Towards Understanding an Imperfect Built Environment: A Methodology for In-Situ Characterization of Building Envelope Thermal Performance

A Dissertation
Presented to
The Academic Faculty

by

Tyler Pilet

In Partial Fulfillment
of the Requirements for the Degree
Doctor of Philosophy in the
School of Architecture

Georgia Institute of Technology
May, 2022

Towards Understanding an Imperfect Built Environment: A Methodology for In-Situ Characterization of Building Envelope Thermal Performance

Approved by:

Dr. Tarek Rakha, Advisor
School of Architecture
Georgia Institute of Technology

Dr. Jason Brown
Research Engineer
Raven Research

Dr. Russell Gentry
School of Architecture
Georgia Institute of Technology

Dr. Juan Ordonez
Department of Mechanical Engineering
FAMU-FSU College of Engineering

Cheryn Metzger
Residential Buildings Program Manager
Pacific Northwest National Laboratory

Date Approved: March 3, 2022

To my grandmother, Francis Ciuffi Hillebrandt. Thank you for pushing me further than ever thought possible.

ACKNOWLEDGEMENTS

I would like to thank my committee for their support in this work. Each committee member represents a specific piece of my professional development up to this point, and I would like to thank each of you for being part of this experience. Thank you to Dr. Tarek Rakha for advising me through this journey and broadening my horizons well beyond anything I expected in a Ph.D. I would also like to thank Dr. Jason Brown and Professor Godfried Augenbroe for bringing me to Georgia Tech and providing the foundational experience to ask the right questions. I will carry this with me through the rest of my life. Rest in peace, Fried. Thank you to Dr. Russell Gentry for making me feel welcome from the very start of my Ph.D. Thank you to Dr. Juan Ordonez for providing me with the seeds of opportunity which have developed into my career and research interests. I never would have considered a graduate education had our paths not crossed. Finally, thank you to Cheryn Metzger for providing the opportunity to further develop my career as a researcher while finishing this doctoral degree. I would also like to give a special thanks to Dr. Simon Pallin for his watercooler chats that developed into this body of research.

Thank you to my family for their support through this process. I never knew if I would have made it to college, much less to a doctoral degree. Thank you for always pushing me to be more and care for my education. The sacrifices you all made allowed for me to strive further than ever anticipated as a first-generation college student.

Finally, thank you to Lena Navarro for your love and undying support in everything I do, especially in balancing the demands of this degree. I deeply appreciate the life we have together, and I feel very blessed to have found you during our time in Atlanta.

TABLE OF CONTENTS

ACKNOWLEDGEMENTS .... **IV**
LIST OF TABLES .... **VIII**
LIST OF FIGURES .... **IX**
LIST OF SYMBOLS AND ABBREVIATIONS .... **XII**
SUMMARY .... **XIV**
CHAPTER 1: INTRODUCTION **1**
1.1 RESEARCH QUESTIONS 3
1.2 SIGNIFICANCE 5
1.3 THESIS STRUCTURE 5
CHAPTER 2: LITERATURE REVIEW **7**
2.1 STATE OF THE ART IN IN-SITU ENVELOPE THERMAL TESTING 7
2.1.1 An Abridged Summary of ASTM C1155 .... *8*
2.1.1.1 Summation Method 8
2.1.1.2 Sum of Least Squares Method 10
2.1.2 An Abridged Summary of ASTM C1046 .... *11*
2.1.3 An Abridged Summary of ISO 9869-1 .... *12*
2.1.3.1 Average Method 13
2.1.3.2 Average Method with Storage Effects 13
2.1.3.3 Dynamic Method 15
2.1.4 Key Takeaways from the State of the Art *16*
2.2 TRANSIENT CONDUCTION NUMERICAL MODELING TECHNIQUES 17
2.2.1 Finite Difference Method *18*
2.2.2 Finite Element Method *22*
2.2.3 Conduction Transfer Function and Response Factor Models *24*
2.3 COMPARISON OF TRANSIENT CONDUCTION CALCULATION APPROACHES 28
2.3.1 TC2: Transient Conduction with Stepped Responses *30*
2.3.2 TC3: Transient Conduction with Sinusoidal Response *34*
2.4 CONCLUDING REMARKS 37
CHAPTER 3: THEORY **39**

3.1 TRANSIENT CONDUCTION ... 41
3.1.1 Basis of Formulation ... 42
3.1.2 Finite Element Spatial Discretization ... 43
3.1.3 Convective and Radiative Boundary Conditions ... 49
3.1.4 Element Temperature Calculation ... 53
3.2 CHARACTERIZATION PROCEDURE AND OBJECTIVE FUNCTION ... 54
3.3 BAYESIAN INFERENCE ... 57
3.4 CHAPTER CONCLUSION ... 59
CHAPTER 4: SIMULATION-BASED VALIDATION ... 62
4.1 PILOT SIMULATION STUDY PARAMETERS ... 62
4.1.1 Assessment Building ... 62
4.1.2 Modeling Approach ... 64
4.1.3 Wall Characterization Simulation Pilot ... 66
4.2 SIMULATION PILOT CHARACTERIZATION RESULTS ... 67
4.2.1 Low Mass Wall Thermal Characterization ... 67
4.2.2 High Mass Wall Thermal Characterization ... 71
4.3 EXPLORING CHARACTERIZATION TIME REQUIREMENTS ... 76
4.4 EVALUATING TRAINING DATASET LENGTH REQUIREMENTS ... 78
4.5 DISCUSSION ... 80
4.6 CHAPTER CONCLUSION ... 83
CHAPTER 5: EXPERIMENTAL VALIDATION ... 85
5.1 EQUIPMENT SELECTION ... 85
5.1.1 Data Acquisition System ... 85
5.1.2 Analog-to-Digital Converter Selection ... 87
5.1.3 Thermistor Selection ... 88
5.1.4 Heat Flux Transducer Selection ... 89
5.2 SENSOR APPLICATION AND USAGE ... 90
5.2.1 Thermistor Usage ... 90
5.2.2 Heat Flux Sensor Usage ... 91
5.3 SENSOR CALIBRATION AND UNCERTAINTY QUANTIFICATION ... 92
5.3.1 Thermistors ... 92
5.3.2 Heat Flux Sensors ... 95
5.4 EXPERIMENTAL DESIGN - ATLANTA ... 96
5.5 EXPERIMENTAL THERMAL CHARACTERIZATION - ATLANTA ... 101
5.6 EXPERIMENTAL DESIGN - CLOQUET ... 106
5.7 EXPERIMENTAL THERMAL CHARACTERIZATION - CLOQUET ... 109
5.8 CHAPTER CONCLUSION ... 114

5.9 CHAPTER ACKNOWLEDGEMENT ... 116
CHAPTER 6: PREDICTING ASSEMBLY CONSTRUCTION FROM IN-SITU CHARACTERIZATION RESULTS ... 117
6.1 CLASSIFICATION FRAMEWORK ... 118
6.1.1 Classification Model and Model Training Data ... 120
6.2 MODEL TRAINING AND TESTING ... 124
6.2.1 Dataset Preparation ... 124
6.2.2 Model Selection and Training ... 125
6.2.3 Model Testing ... 127
6.3 CLASSIFICATION MODEL SPOT VALIDATION ... 128
6.4 CHAPTER CONCLUSION ... 131
CHAPTER 7: CONCLUSION ... 133
7.1 RESEARCH QUESTIONS REVISITED ... 134
7.2 FUTURE WORK ... 139
REFERENCES ... 142
APPENDIX A: EFFECTIVE THERMAL PROPERTIES OF ASHRAE FUNDAMENTALS WALL ASSEMBLIES ... 153
APPENDIX B: SUPPLIMENTS TO THE ASHRAE FUNDAMENTALS WALL DATASET 157

LIST OF TABLES

Table 2.1 A tabulated performance summary of heat transfer algorithms for ASHRAE 1052RP Test TC2 ... 33

Table 2.2 A tabulated performance summary of heat transfer algorithms for ASHRAE 1052RP Test TC3 ... 36

Table 2.3 A tabulated summary of reviewed heat transfer modeling techniques. 37

Table 4.1 ASHRAE Fundamentals wall assemblies utilized within the building simulation (ASHRAE, 2013). ... 66

Table 4.2 Tabulated transient thermal characterization results for a low-mass wall. ... 71

Table 4.3 Tabulated transient thermal characterization results for a high-mass wall. ... 76

Table 5.1 Tabulated thermistor calibration and uncertainty-related metrics. ... 95

Table 5.2 Tabulated thermal characterization results for tested Atlanta wall ... 106

Table 5.3 Tabulated thermal characterization results for tested CRRF Drill-and-Fill wall. ... 114

Table 6.1 Two example assemblies with layer IDs from the ASHRAE Fundamentals Assembly Database. ... 121

Table 6.2 An example visualization of One-Hot Encoding (OHE) for usage on categorical features. ... 125

Table 6.3 Testing performance metrics for the KNN classification model. ... 128

Table 6.4 Assembly classification predictions for the Atlanta brick wall. ... 131

LIST OF FIGURES

Figure 2.1 A diagrammatic representation of the Summation Method's instrumentation requirements. 9

Figure 2.2 A diagrammatic representation of the SLS Method's sensor layout for a sample roof assembly (J. V Beck et al., 1991). 11

Figure 2.3 (a) A network representation of a 2R1C model. (b) A network representation of a 3R2C model. 20

Figure 2.4 A screenshot of a discretized wall assembly in WUFI (Ramos et al., 2010) and its representative thermal circuit. 21

Figure 2.5 A plot of a sample internal surface conduction time series factor. 26

Figure 2.6 Four plots displaying the performance of different transient heat transfer algorithms for the ASHRAE 1052RP TC2 Step-Response test. 32

Figure 2.7 Four plots displaying the performance of different transient heat transfer algorithms for the ASHRAE 1052RP Test TC3. 35

Figure 3.1 A graphical representation of the heat transfer modes influencing façade performance, which can be reduced to a simplified system with the use of a surface temperature measurement. 39

Figure 3.2 A representation of nodes and elements in 2D. 44

Figure 3.3 A representation of local element coordinates using Element 1. 44

Figure 3.4 The proposed sensor layout for in-situ thermal characterization method proposed within this work. 54

Figure 4.1 A view of the single-family reference building's geometry. 63

Figure 4.2 Plotted time-series interior heat gain from a 48-hour Bayesian characterization of a low mass wall. 67

Figure 4.3 Histograms of posterior distributions of the Bayesian inference parameters characterized in the spring low-mass wall characterization. 68

Figure 4.4 Plotted time-series interior heat gain from a traditional steady-state characterization for a low-mass wall during a spring simulation period. 70

Figure 4.5 Plotted interior heat gain from a Bayesian characterization for a high mass wall with 48 hours of training data. 72

Figure 4.6 Histograms of prior and posterior distributions of the Bayesian inference parameters characterized in the spring high-mass wall characterization. 73

Figure 4.7 Plotted time-series interior heat gain from a steady-state summation method characterization for a high-mass wall assembly. 74

Figure 4.8 A histogram visualizing the training length required to achieve an appropriate wall characterization. 78

Figure 5.1 An Arduino MKR Zero. 87

Figure 5.2 An ADS1115 breakout board. 88

Figure 5.3 A photo of the thin-film thermistor utilized. 89

Figure 5.4 A photo of the heat flux sensor utilized. 89

Figure 5.5 A diagram of the Wheatstone bridge circuit. 90

Figure 5.6 A photograph of the thermistor calibration setup. 93

Figure 5.7 A graphical display of a calibrated thermistor curve compared to the calibration data. 94

Figure 5.8 A photograph of the building where experimentation occurred. 97

Figure 5.9 A photograph of the building's brickwork pattern. 98

Figure 5.10 A diagram displaying the sensor layout utilized in this experiment. 99

Figure 5.11 A photograph of the exterior surface temperature sensor. 100

Figure 5.12 A photograph of the interior surface sensors and EPS board. 100

Figure 5.13 Plotted interior heat gain from a Bayesian characterization for the Atlanta characterization experiment. 102

Figure 5.14 A graph of the time series measured interior-surface heat gain compared to the steady-state. 103

Figure 5.15 The Markov chain trace plot of thermal resistance and thermal mass for the Atlanta wall characterization. 104

Figure 5.16 Histograms of the posterior distribution of the Bayesian inference parameters characterized in the Atlanta wall characterization. 105

Figure 5.17 Photographs of the cellulose drill-and-fill wall installation at the CRRF. (Photo Credit: Patrick Huelman) 107

Figure 5.18 A diagram of the drill-and-fill wall assembly composition and sensor layout. 108

Figure 5.19 Plotted interior heat gain from a Bayesian characterization for the Cloquet drill-and-fill characterization experiment. 110

Figure 5.20 Trace plots of the Bayesian inference parameter Markov chains in the CRRF Drill-and-Fill characterization. 111

Figure 5.21 Histograms of prior and posterior distributions of the Bayesian inference parameters characterized in the CRRF Drill-and-Fill wall characterization. 112

Figure 5.22 A graph of the time series measured interior-surface heat gain compared to the steady-state for the CRRF Drill-and-Fill assembly. 113

Figure 6.1 The proposed methodology framework for construction inference from in-situ thermal data....... 119

Figure 6.2 A scatter plot of thermal mass and thermal resistance values for the wall assembly dataset. 123

Figure 6.3 Two graphs displaying the hyperparameter optimization for the KNN model. 126

Figure 6.4 A photograph of the Atlanta case study wall....... 129

Figure 6.5 Histograms of the characterized thermal resistance and thermal mass for the Atlanta wall....... 130

LIST OF SYMBOLS AND ABBREVIATIONS

Symbol	Name	Unit
	Latin Characters	
$\boldsymbol{a}, \boldsymbol{b}$	Lognormal Distribution Coefficients	Coefficient
$\boldsymbol{C}$	Thermal Mass, FEM Mass Matrix	$\frac{\boldsymbol{J}}{\boldsymbol{m^2-K}}$
$\boldsymbol{C_p}$	Specific Heat Capacity	$\frac{\boldsymbol{J}}{\boldsymbol{kg-K}}$
$\boldsymbol{E}$	Gauss Quadrature Point	Coefficient
$\boldsymbol{F}$	FEM Boundary Condition Force Matrix	Coefficient
$\boldsymbol{f}$	Dependent Variable	Varies
$\boldsymbol{H}$	FEM Boundary Condition Conductance Matrix	Coefficient
$\boldsymbol{h}$	Convection or Film Coefficient	$\frac{\boldsymbol{W}}{\boldsymbol{m^2-K}}$
J	FEM Jacobian Matrix	Coefficient
$\boldsymbol{k}$	Thermal Conductivity	$\frac{\boldsymbol{W}}{\boldsymbol{m-K}}$
$\boldsymbol{K}$	FEM Thermal Conductance Matrix	$\frac{\boldsymbol{W}}{\boldsymbol{m^2-K}}$
$\boldsymbol{L}$	Length	$\boldsymbol{m}$
$\boldsymbol{NRMSE}$	Normalized Root Mean Sum-of-Squares Error	%
$\boldsymbol{p}$	Probability	%
$\boldsymbol{\dot{q}}$	Heat Flux	$\frac{\boldsymbol{W}}{\boldsymbol{m^2}}$
$\boldsymbol{R}$	Thermal Resistance	$\frac{\boldsymbol{m^2-K}}{\boldsymbol{W}}$
$\boldsymbol{RMSE}$	Root Mean Sum-of-Squares Error	Varies
$\boldsymbol{t}$	Time	s, hr
$\boldsymbol{T}$	Temperature	°C
$\boldsymbol{x}, \boldsymbol{X}$	Cartesian Horizontal Coordinates	m
$\boldsymbol{y}, \boldsymbol{Y}$	Cartesian Vertical Coordinates, Sample Dependent Variable	m, Unitless
W	Weight Coefficient	Coefficient

Greek Characters		
$\boldsymbol{\epsilon}$	Measurement/Model Error	Varies
$\boldsymbol{\eta}, \boldsymbol{\zeta}$	Local FEM Coordinates	Coefficient
$\boldsymbol{\theta}$	Vector of Model Inputs	Varies
$\boldsymbol{\mu}$	Mean	Varies
$\boldsymbol{\pi}$	Mathematic Constant Pi	Constant
$\boldsymbol{\rho}$	Density	$\boldsymbol{\frac{kg}{m^3}}$
$\boldsymbol{\sigma}$	Standard Deviation	Varies
$\boldsymbol{\Psi}$	FEM Shape Function	Coefficient

SUMMARY

As buildings age, retrofits are becoming an increasingly important topic for the ever-growing and aging existing building stock. Following construction, a building's energy footprint typically remains relatively stagnant, effectively locking-in that building's energy usage for its lifetime. With 50% of America's building stock built before 1980 and only 0.5–1% of existing buildings retrofitted annually, it is essential to reduce guesswork and make building energy retrofits more accessible to reduce the energy footprint of the building sector. Building retrofits are plagued by a lack of original design documentation and general uncertainty regarding the building's envelope composition and integrity. The goal is this work is to utilize the power of transient heat transfer modeling to non-intrusively characterize the thermal properties of a building's envelope to inform energy modeling, facade design, and project appraisal. This thesis presents a literature survey of the state-of-the-art in in-situ thermal testing, a thermal characterization methodology to non-destructively identify representative thermal properties for existing building envelopes, a simulation-based study to verify the thermal characterization method, two physical experiments to validate the thermal characterization method, and a proof-of-concept machine learning approach to classify in-service assemblies via the proposed thermal characterization methodology. This dissertation is designed to bridge the gap between the discrete procedures of building audits and building energy modeling processes to enable a better understanding of existing building envelopes and reduce guesswork from envelope retrofits.

CHAPTER 1: INTRODUCTION

In the developed world, buildings are built not only to protect occupants and their belongings from rain and sun; modern buildings are built to provide a comfortable conditioned space for occupants. Spaces are often conditioned at the cost of burning fuels for heat or utilizing electrical energy to compress refrigerants for cooling. Regardless of the mode, space conditioning is achieved by utilizing energy to generate indoor conditions irrelevant to exterior conditions. The conditioned spaces that the modern world has come to expect in buildings come at the cost of energy, and often at the primary energy source, greenhouse gas emissions. While space conditioning is a major contributor to global climate change, it is important to note that people have come to expect indoor spaces to be conditioned and comfortable, so it is nearly impossible to decouple space conditioning and expectations of comfort from buildings. Instead, it is more practical to focuses more on the reduction of thermal loads to reduce the energy need of space conditioning.

The US Department of Energy reports that 42% of energy use in buildings is a result of thermal losses through a building's thermal envelope (DOE, 2012; EIA, 2012). Building envelopes serve as the primary barrier between the indoor conditioned space and exterior environment, so it is important to design envelopes thoughtfully and carefully to minimize energy losses. To better understand the relationship between a material and its relationship with conductive heat transfer, thermal resistance, or R-value, can be utilized to understand the insulating performance of a material. Everett Schuman, director of the Penn State Housing Research Institute, first developed R-value in 1945 to quantify the insulating performance of various insulation materials on the market (Straube, 2007). As Schuman proposed it, R-value was intended to represent the performance of a layer of material, as opposed to the performance of an entire assembly. There are two large assumptions made when applying R-value to a whole assembly: (1) All modes of heat transfer will be assumed to be represented as conductive heat transfer, and (2) the assembly operates in steady-state conditions. The first assumption can be addressed by understanding that assembly R-values are subject to the temperature and environmental conditions at which the assembly is tested, as material thermal conductivity, convection, and thermal radiation are all dependent on environmental factors. This means that R-values may change slightly depending on the situation; however, R-values are meant to be an estimation tool. Secondly, R-values are designed to represent steady-state conductive performance. Steady-state conditions are rarely established in in-service assemblies, therefore, thermal mass must be considered alongside thermal resistance when calculating heat transfer through an assembly (Childs et al., 1983).

Utilizing modern simulation tools, the transient thermal performance of an assembly can be computed for design cases by specifying material layer ordering and inputting the thermal properties of each material. This makes accounting for assembly thermal mass a fairly trivial task to most designers. This process is, however, nowhere near as trivial when working with in-service or historic buildings. In these cases, assumptions on materials and construction methods can be approximated based upon the year of construction and local building code, if applicable. With energy codes being established as recently as 1992 and various uncertainties related to material degradation and condition, estimating assembly composition can be very difficult with older buildings (Shankle et al., 1994). This problem compounds further with 68% of the US building stock constructed before 1990 (IEA, 2019; National Renewable Energy Laboratory, 2019), and only 0.5-1% of existing buildings are renovated annually (Architecture 2030, 2018).

With the United States' aging in-service building stock, existing buildings must be rehabilitated to guarantee their performance for years to come. In practice, it is difficult to work with existing buildings due to missing documentation and uncertainties in the composition and integrity of a building's envelope. To solve this problem, destructive or non-destructive forensic testing is employed during the building retrofit and repair process. One method of testing the thermal performance of an existing building is via R-value testing, where an existing building envelope is instrumented with sensors and performance is measured. Currently, the state of the art for assessing the thermal performance of an as-built assembly is through in-situ R-value testing, as described in ASTM C1155 "Standard Practice for Determining Thermal Resistance of Building Envelope Components from the In-Situ Data" (ASTM, 2013b). One major limitation of this practice is the fact that it glosses over the uncertainties of thermal mass and instead prioritizes R-value measurement.

1.1 Research Questions

In conclusion, thermal losses and gains through building envelopes represent slightly less than half of a building's annual energy usage. Few buildings in the United States are being renovated each year, and the US building stock is aging. To address this problem and enable envelope retrofits, it is suggested that non-destructive testing be deployed on existing building envelopes to better understand their performance, enabling more informed retrofit decision-making. For this technique, the current state of the art is governed by ASTM C1155, "Standard Practice for Determining Thermal Resistance of Building Envelope Components from the In-Situ Data." Unfortunately, this standard focuses primarily on thermal resistance and does not provide a methodology to infer an assembly's thermal mass. Fortunately, the Sum of Least Squares Technique proposed in ASTM C1155 does provide an inverse modeling platform to infer thermal mass and thermal resistance via non-intrusive temperature and heat flux measurements. The goal of this dissertation research is to expand this methodology to infer thermal mass alongside thermal resistance in a non-intrusive manner. In subsequent chapters, various transient heat transfer algorithms will be evaluated for this application, the problem and sensor layout will be reformulated for non-intrusive measurement, and the improved methodology will be verified via simulation and validated via experiments. This research will be structured to address the following questions:

1) Which methods apply to compute the effective thermal properties of an existing building envelope assembly?
2) Can the sensors and methods from the state-of-the-art methods be utilized to non-destructively infer thermal mass and thermal resistance?
3) How can the proposed inverse modeling approach be verified against existing simulation workflows and validated for field deployment?

4) How long must an assembly be instrumented with sensors to infer thermal mass and thermal resistance?
5) What is the impact of thermal mass on envelope heat transfer, and is it required that thermal mass be measured alongside thermal resistance?
6) How can the measurement of thermal mass and thermal resistance be made beneficial to those without the specialized knowledge to simulate transient heat transfer?

Each of these questions seeks to develop and further enable the applicability and relevance of transient thermal characterization. Each of these questions will be addressed in detail in subsequent chapters.

1.2 Significance

This dissertation proposes a model to compute the effective thermal properties of a building envelope assembly in a non-destructive and non-intrusive manner. This work aims to bolster existing methods and testing workflows currently utilized for in-situ R-value testing of envelope assemblies to encompass thermal mass alongside thermal resistance. The goal of this work is to provide a non-destructive diagnostic tool to better understand the in-service thermal performance of assemblies to enable retrofits and allow for a more detailed understanding of our existing built environment.

1.3 Thesis Structure

This dissertation is designed to address each of the research questions posed in Section 1.1. Chapter 1 serves as the introduction and motivation to the work. Chapter 2 is a review of the current state of the art and an abridged literature review of methods to solve the transient conduction problem. This chapter also tests these various methods to motivate transient conduction algorithm selection. Chapter 3 is a chapter on research methods, where the transient conduction algorithm is described in detail, the Bayesian inference algorithm is described and motivated, and the proposed thermal characterization methodology is described in detail. Chapter 4 is a simulation-based verification of the proposed methodology, where the proposed thermal characterization methodology's performance is validated against simulation test cases. Chapter 5 is an experimental validation of the proposed thermal characterization methodology. Chapter 6 presents a proof-of-concept machine learning methodology to classify envelope assemblies, built upon the proposed thermal characterization methodology. Finally, Chapter 7 concludes with a reflection on the developments made within this dissertation and answers each of the research questions this dissertation set out to address.

CHAPTER 2: LITERATURE REVIEW

In Chapter 1, the importance of better understanding the performance of existing envelope assemblies was motivated. Thermal losses through envelopes represent a large fraction of energy usage in buildings, and the US building stock is continually aging and is rarely experiencing retrofits. To address this problem, in-situ thermal testing can be utilized to better understand the thermal performance of existing, in-service building envelopes. This chapter seeks to explore the state of the art in in-situ thermal testing and address methods to include thermal mass into existing in-situ testing methods.

2.1 State of the Art in In-Situ Envelope Thermal Testing

With the relative importance of in-situ testing understood, it is important to understand how in-situ testing is currently conducted. At this time, there are two main ASTM standards governing in-situ R-value testing—ASTM C1155 "Standard Practice for Determining Thermal Resistance of Building Envelope Components from the In-Situ Data" and ASTM C1046 "Standard Practice for In-Situ Measurement of Heat Flux and Temperature on Building Envelope Components" (ASTM, 2013b, 2013a). Per their names, ASTM C1155 addresses the process to compute in-situ R-values from sensor data, and ASTM C1046 governs the sensor implementation required to collect the in-situ thermal data. These two standards build upon each other to enable in-situ R-value testing. Similarly, there is an equivalent ISO standard entitled: ISO 9869 "In-situ measurement of thermal resistance and thermal transmittance." This ISO standard is very similar to ASTM C1155 and contains very similar methods, therefore, this standard will not be discussed in detail.

2.1.1 An Abridged Summary of ASTM C1155

ASTM C1155 standardizes the practice of in-situ R-value testing for in-service assemblies. This standard provides two techniques for calculating R-value from sensor data—the Summation Method and the Sum of Least Squares Technique, with the former Summation Method being the more popular and more addressed method within the standard.

2.1.1.1 Summation Method

The Summation Method was first proposed by Modera et al. in their conference paper titled "Determining The U-Value of A Wall from Field Measurements of Heat Flux and Surface Temperatures" (Modera et al., 1985). The equation for the summation is displayed below:

$$R_{eff} = \frac{\sum_{k=1}^{M}\left(T_{si,k} - T_{so,k}\right)}{\sum_{k=1}^{M} \dot{q}_{si,k}} \tag{1}$$

From Eq. 1, an inference can be made regarding the effective thermal resistance of the candidate assembly. In this equation, R_{eff} is the effective thermal resistance in W/m^2, and T_{si} and T_{so} is a vector of interior and exterior surface temperatures, respectively, measured from the candidate assembly in °C. In the original paper, this equation was proposed under the assumption that thermal mass and environmental conditions are periodic, causing any transient effects of thermal mass to wash out of the equation as increasingly large timescales of data were used in the summation. In the real world, this assumption differs slightly from real environmental conditions, which may cause this R-value to be skewed via the effects of thermal mass. This problem is further exacerbated when considering that most citations to ASTM C1155 in research and development are often about the Summation Method (FluxTeq, 2016; Hukseflux, 2021; Sujatmiko et al., 2016). ISO 9869 also has an equivalent version of the summation method called the Average Method. The Average method is identical to the Summation Method.

One advantage of the summation method is its non-invasive instrumentation requirements. The summation method only requires that sensors be placed on the exterior and interior surfaces of an envelope, which allows for testing in occupied or in-service buildings. An instrumentation diagram for the summation method is displayed in Figure 2.1.

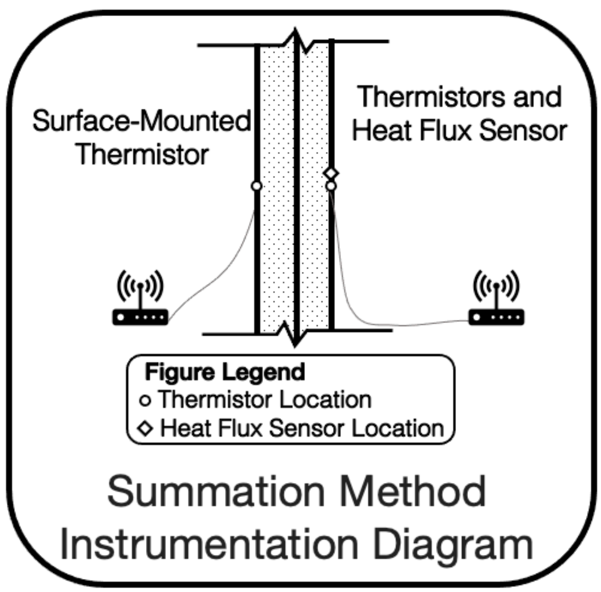

Figure 2.1 A diagrammatic representation of the Summation Method's instrumentation requirements.

2.1.1.2 Sum of Least Squares Method

To address the influence of thermal mass, ASTM C1155 provides a second method, the Sum of Least Squares (SLS) technique. This method, originally proposed by Beck, Petrie, and Courville in 1991, solves a partial differential equation via finite difference approximations to account for the impact of thermal mass on R-value while minimizing an objective function to match simulation results to measured data (J. V Beck et al., 1991). This method utilizes the following two equations:

$$\frac{\partial}{\partial x}\left(k\frac{\partial T}{\partial x}\right) = (\rho C_p)\frac{\partial T}{\partial t}, \text{ with } \dot{q} = -k\frac{\partial T}{\partial x} \tag{2}$$

$$SSE = \sum_{i=1}^{K}\sum_{m=1}^{M}\left(\hat{T}_{m,i} - T_{m,i}\right)^2 W_{T,m} + \sum_{i=1}^{K}\sum_{n=1}^{N}\left(\widehat{\dot{q}_{n,i}} - \dot{q}_{n,i}\right)^2 W_{\dot{q},m} \tag{3}$$

Where Eq. 2 is solved under the exterior and interior surface temperature boundary conditions via finite differencing. The corresponding nodal temperatures and heat flux values are then utilized in Eq. 3, where the weighted sum of squared error is computed and the Gauss linearization algorithm is utilized to minimize model/measured error (J. V. Beck & Arnold, 1977). One important note on Eq. 3 is that the m and n subscripts correspond to the internal layers of the assembly, indicating that this method requires the temperature and heat flux sensors to be built inside of the assembly. A diagram of Beck et al.'s proposed sensor layout is displayed in Figure 2.2.

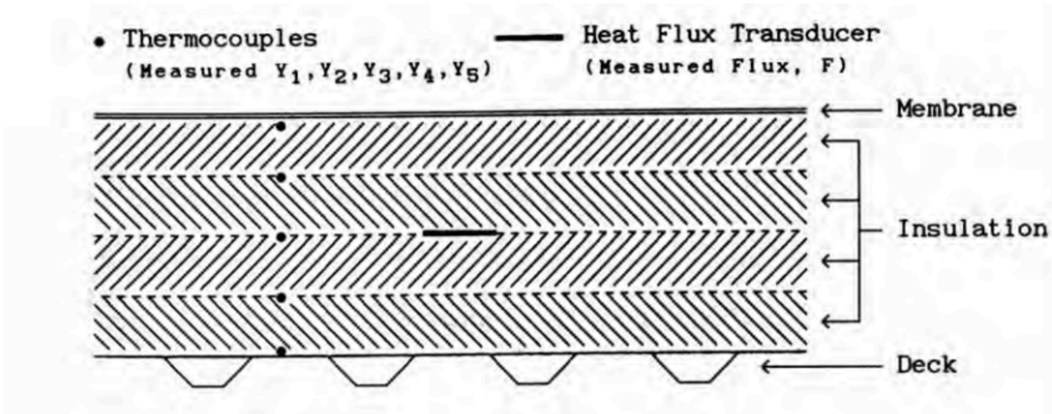

Figure 2.2 A diagrammatic representation of the SLS Method's sensor layout for a sample roof assembly (J. V Beck et al., 1991).

In Figure 2.2, the SLS Method proposes an instrumentation layout with sensors inside of the assembly. For experimental constructions, this is a fair to assume that sensor can be placed inside of an assembly during construction. However, the least squares technique, at least how it is expressed in ASTM C1155 and in Beck et al.'s, is incompatible with in-service that currently do not contain sensors inside of the assembly. It is possible to install sensors inside of an existing assembly via drilling and installing probe sensors, however, this may not be appliable in historic or in-service buildings where assemblies cannot be disturbed.

2.1.2 An Abridged Summary of ASTM C1046

ASTM C1046 provides a significant amount of context related to the selection, usage, and installation of temperature and heat flux sensors for in-situ measurement of envelope assemblies. This standard is extensive; however, the key takeaways of this standard as they related to ASTM C1155 are as follows:

- Heat flux and temperature sensors must have a lower thermal time constant than the envelope assembly being instrumented in non-steady-state conditions.
- A single measurement site is not representative of an entire building. Infrared thermography should be used to identify similar sites.
- Infrared thermography should be used to identify defects, thermal bridging, convective loops, and air leakage in assemblies.
    - In the case of defect measurement, the measurement should take place at the center of the defective area.
    - Alternatively, when instrumenting an assembly outside of areas with defects, measurement is recommended to occur with defects or thermal bridging as far away as possible (e.g. at the exact center of the cavity in a stud wall construction).
    - When instrumenting an assembly with a suspected convective loop or air leakage (visible via thermal imaging), it is recommended to instrument at the top, middle, and bottom of the assembly and average their results.
- To reduce rapid thermal fluxation due to environmental factors, heat flux transducers and temperature sensors on the interior or exterior surfaces of an assembly can be placed under a layer of additional, low thermal mass material. The impact of this material's thermal resistance should be removed after assembly thermal resistance is computed.

2.1.3 An Abridged Summary of ISO 9869-1

ISO 9869-1 is the international counterpart to ASTM C1155 and ASTM C1046. This standard is entitled: "*In-Situ Measurement of Thermal Resistance and Thermal Transmittance.*" This standard governs sensor usage, calibration, installation, and analysis of in-situ thermal data to compute thermal resistance (ISO, 2014). ISO 9869-1 proposes three methods to compute in-situ thermal resistance: (1) the Average Method, (2) the Average Method with Storage Effects, and (3) the Dynamic Method.

2.1.3.1 Average Method

In short, the Average Method is the ISO 9869-1 version of ASTM C1155's Summation Method. The Average Method's equation is exactly that of the Summation Method displayed in Eq. 1.

2.1.3.2 Average Method with Storage Effects

Acknowledging that the Average Method may fail to compute effective thermal resistance on high mass assemblies, ISO 9869-1 proposes the Thermal Mass Correction Factor. The thermal mass correction factor is calculated and implemented with the following equations:

$$R_{si,k} = \sum_{j=1}^{k-1} R_j \quad R_{so,k} = \sum_{j=\mathrm{k}+1}^{N} R_j \tag{4}$$

Where k is the layer number, ordered from 1 to N with 1 as the interior surface and N as the exterior surface. Utilizing these factors, the thermal mass factors for each layer k can be computed with the following:

$$F_{si,k} = C_k \left(\frac{R_{so,k}}{R} \left(\frac{1}{6} + \frac{R_{so,k} + R_{si,k}}{3R} \right) + \frac{R_{so,k} R_{si,k}}{R^2} \right) \tag{5}$$

$$F_{so,k} = C_k \left(\frac{R_k}{R} + \frac{{R_k}^2}{3R^2} - \frac{R_{so,k} R_{si,k}}{R^2} \right) \tag{6}$$

Where C_k is the thermal mass, or thermal capacitance, of each layer, and R is the total assembly thermal resistance. With the thermal mass factors computed for each layer, the interior and exterior thermal mass correction factors for the assembly can be computed with the following summations:

$$F_{si} = \sum_{k=1}^{N} F_{si,k} \quad F_{so} = \sum_{k=1}^{N} F_{so,k} \tag{7}$$

These thermal mass correction factors can then be applied to the average method in the following way:

$$R_{eff} = \frac{\sum_{i=1}^{M} \left(T_{si,i} - T_{so,i} \right)}{\sum_{i=1}^{M} \dot{q}_{si,i}} \quad \text{, for the first 24 hours.} \tag{8}$$

$$R_{eff} = \frac{\sum_{i=1}^{M} \left(T_{si,i} - T_{so,i} \right)}{\sum_{i=1}^{M} \dot{q}_{si,i} - \frac{(F_{si}\,\delta T_{si} + F_{so}\,\delta T_{so})}{\Delta t}} \quad \text{, after the first 24 hours.} \tag{9}$$

Where δT_i is the difference between internal averaged temperature over the 24 h prior to the reading k and internal averaged temperature averaged over the first 24 h of the analysis period, δT_e is the difference between external averaged temperature over the 24 h prior to the reading k and external averaged temperature averaged over the first 24 h of the analysis period, and Δt is the time interval between readings in seconds.

While the thermal mass correction factor does augment the average method, this approach has one major drawback—The composition of the assembly must be known to compute the thermal mass correction factors. From a practical perspective, there may be no reason to perform an in-situ thermal resistance test if the assembly's materiality is already known; thermal resistance could be approximated utilizing estimated material properties of the assembly's known layering. Due to this limitation, the thermal mass correction factor may not have much utility when assembly composition is unknown.

2.1.3.3 Dynamic Method

The dynamic analysis method is the final method to compute thermal resistance, located within the appendices of ISO 9869-1. This method is built upon the assumption that the heat flow rate is a function of all temperatures at that time and at all preceding times. In short, the dynamic analysis method is a sophisticated method to simulate transient conduction based upon the following equation:

$$\begin{aligned}\hat{\dot{q}}_{in,i} = \frac{T_{si,i} - T_{so,i}}{R} &+ G_1\dot{T}_{si,i} - G_2\dot{T}_{so,i} \\ &+ \sum_n P_n\left(\sum_{j=i-p}^{i-1} T_{si,i}(1-\beta_n)\beta_n(i-j)\right) \\ &+ \sum_n Q_n\left(\sum_{j=i-p}^{i-1} T_{so,i}(1-\beta_n)\beta_n(i-j)\right)\end{aligned} \tag{10}$$

Where G_1, G_2, P_n, Q_n and β_n are coefficients which represent the dynamic thermal mass characteristics of the assembly, which can be computed by minimizing the difference between $\hat{\dot{q}}_{in}$ and the measured $\dot{q}_{in}$ similar to objective function present in Eq. 3.

Without going into additional detail on this algorithm, the representation of thermal mass as a combination of unitless coefficients obscures the physical nature of the assembly's thermal mass. This method's goal primary goal is to approximate thermal resistance, with the influence of thermal mass's impact being considered but its estimation being an afterthought. This is considered to be a major drawback of this method—thermal resistance and a collection of non-informative coefficients unfortunately provide no additional context on an assembly's thermal properties compared to the traditional average method.

2.1.4 Key Takeaways from the State of the Art

While ASTM C1155 and ISO 9869-1 do have significant shortcomings, both of these standards provide a foundation for in-situ thermal characterization to estimate thermal mass and thermal resistance. Regardless of the method, ASTM C1046 and ISO 9869-1's guidance applies to any in-situ thermal measurement. Both ASTM C1155 and ISO 9869-1 do, however, have significant shortcomings. Both standards focus primarily on the summation/average method for thermal resistance calculation, which ignores the influence of thermal mass. This is unfortunate, as envelope assemblies are rarely subject to steady-state conditions and thus thermal mass has a thermal impact in most typical conditions.

While the summation and average methods do ignore thermal mass, ASTM C1155 does address thermal mass intuitively via the Sum of Least Squares Technique. This differs in comparison to ISO 9869-1's dynamic method and thermal mass correction factors, where thermal mass is non-intuitively represented as cumbersome, application-specific coefficients as opposed to a parameter with physical meaning. While the SLS technique does have shortcomings for non-destructive measurement, e.g. requiring sensors to be installed inside the assembly, this inverse modeling approach does provide a flexible platform to develop techniques atop. For example, the SLS Technique as per the standard suggests that the user estimate the assembly's thermal mass values; however, this inverse modeling approach does provide the flexibility for thermal mass to be inferred alongside thermal mass via the optimization approach. For brevity, the inference of thermal resistance and thermal mass will be referred to as transient thermal characterization in this dissertation.

Additionally, the problem and sensor layout can most likely be reformulated to remove the need for sensors located inside of the candidate assembly. This is a major shortcoming of ASTM C1155's SLS Technique, as it is often not possible or not preferable for destructive thermal probes to be placed inside of an in-service assembly. Addressing this problem would allow for this method to be relevant for historic buildings and buildings where destructive measurement is not possible.

2.2 Transient Conduction Numerical Modeling Techniques

Building upon ASTM C1155's SLS technique, different approaches can be utilized to bolster this technique's performance and applicability. At its core, the SLS technique is an inverse model—a model that calculates, from a set of observations or measurements, the factors that produced them. In the case of engineering modeling, an inverse model utilizes an optimization algorithm to tune physical parameters to minimize error between measures and simulated data. This is the basis of the SLS technique—this approach simulates transient conduction via finite differencing and minimizes an objective function. In this approach, transient conduction is computed thousands, if not tens of thousands of times, while an optimization algorithm minimizes an objective function. Due to the number of simulations required, it is necessary to select the proper transient heat transfer model to ensure computation accuracy and efficiency for the inverse model. To address transient model selection, a review and evaluation of transient conduction modeling approaches was conducted within this section.

It should also be noted that a similar case could be made for the selection of the optimization algorithm. Fortunately, extensive reviews on this topic exist within literature (J. V. Beck & Arnold, 1977; Bierlaire, 2015; Fister et al., 2013; Q. Li, 2017; Tian et al., 2014; Venter, 2010; Yao et al., 2011) and therefore will be outside of the scope of this dissertation's literature review.

2.2.1 Finite Difference Method

One of the most frequently implemented models to evaluate the thermal performance of an envelope component is the finite difference method (FDM). THE FDM is a method to solve differential equations by approximating derivatives via finite-difference. The FDM in building envelope research is known by many names, such as Resistance-Capacitance (RC) models, 2R1C models, 3R2C models, etc., but the common naming characteristic is the R and C. Each of these models is defined by a finite volume discretization which, in 1D, reduces the problem to an analogous electrical circuit model, with thermal resistance modeled as a resistor, thermal storage modeled as a capacitor, temperatures modeled as voltages, and heat fluxes modeled as currents all within an electrical circuit network. One of the major advantages of RC models is that each parameter within the model has a physical meaning (Wang & Xu, 2006), allowing for a user to anticipate the computed result.

RC models were first proposed by Lorez and Masy and have been widely utilized since (Hudson & Underwood, 1999; Lorenz & Masy, 1982). The model Lorez and Masy produced has one capacitor for the lumped thermal capacitance of the building envelope and two resistors representing two halves of the envelope's total thermal resistance. While Lorez and Masy represented the entire building's envelope with one lumped network, researchers have adopted this methodology to represent buildings, rooms, and individual envelope components (Bénard et al., 1992; Cui et al., 2018). Over time, more lumped capacitance methods appeared, distributing thermal resistances and thermal capacitances among more components to produce more accuracy than the baseline 2R1C method (Bénard et al., 1992; Fraisse et al., 2002; Fux et al., 2014; Kummert et al., 1996). Sample networks of 2R1C and 3R2C networks can be seen below in Figure 2.3. While 3R2C and higher-order RC models show more promise of accurately representing an opaque assembly's thermal performance, the process does still require costly iterative solvers to solve coupled differential equations.

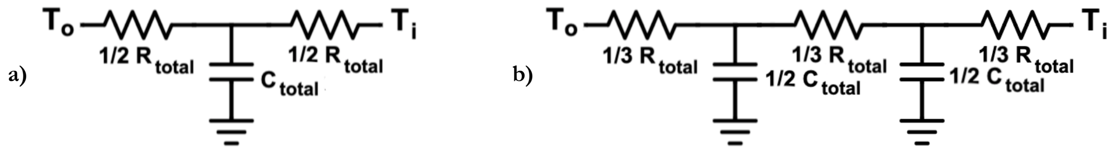

Figure 2.3 (a) A network representation of a 2R1C model. (b) A network representation of a 3R2C model.

While the node count in an RC network is a debated topic, Antonopoulos and Koronaki determined that the summed capacitance values in RC models are inadequate for precise solutions (Antonopoulos & Koronaki, 1998). Before this work, Antonopoulos and Koronaki stated that assembly capacitance was typically calculated as the sum of the envelope components' capacitances, which they referred to as apparent capacitance. They showed that another term, known as effective capacitance, should be solved from measurement data and utilized for future calculations. The effective capacitance they proposed differed in value from the lumped, apparent capacitance term, since effective capacitance represented the effective thermal properties of a complex assembly as one single thermal mass term.

The lumped capacitance method is a frequently used physics-based model used for inverse modeling due to its small computational overhead and simple implementation. Similar to its forward modeling approaches, there are lumped capacitance inverse models to predict indoor conditions (R. Kramer et al., 2013; R. P. Kramer & van Schijndel, 2012), façade performance (Alshatshati, 2017), and even heat transfer coefficients (Anderson & Singh, 2006; Mohamed, 2008).

Similar to the simplified RC models (2R1C, 3R2C, etc.), there are also RC models with higher RC discretization counts, sometimes referred to as Finite Volume Method (FVM) models. Technically, all RC thermal models are simplified FVM models, however, FVM models in published building conduction literature are either multi-dimensional or have higher discretization counts than simple RC models. An example of a FVM problem discretization is displayed in Figure 2.4.

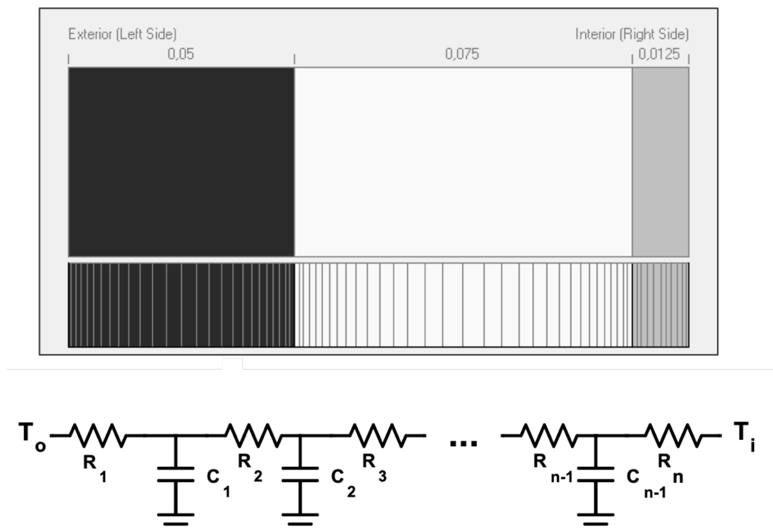

Figure 2.4 A screenshot of a discretized wall assembly in WUFI (Ramos et al., 2010) and its representative thermal circuit.

In Figure 2.4, a length-discretized wall assembly from WUFI is shown alongside its representative thermal circuit. It should be noted that the thermal circuit seen in this finite volume problem is simply a longer, more discretized version of the RC model thermal circuits highlighted in Figure 2.3. This is precisely the difference between lumped capacitance models and finite difference models; lumped capacitance models represent an entire assembly as a “lumped capacitance” and resistance, while finite difference models are a collection of discrete elements modeled as discrete capacitor-resistor combos.

Two widely recognizable softwares in the building industry that employ the finite volume method are EnergyPlus’s finite difference method conduction algorithm (Tabares-Velasco et al., 2012) and WUFI (Ramos et al., 2010). Tabares-Velasco states that the finite volume method was added to EnergyPlus as an optional solver that was capable of handling the temperature and state dependency phase change materials into envelope simulations while also simulating temperatures throughout a multi-layered assembly. WUFI, similarly, utilizes finite volumes to address the highly non-linear problem of hypothermal transport through building envelope assemblies.

The finite volume method is also used frequently in literature, with it being used for roofs (Al-Sanea, 2003; Kumar & Kaushik, 2005), obstructions within envelopes (Zhu et al., 2012), façade optimization (L. P. Li et al., 2008; Ozel, 2011), and whole-building simulation (Koo et al., 2014; Luo et al., 2008; Yang et al., 2018).

2.2.2 Finite Element Method

Rather than lumping material together to form a thermal resistance network, opaque components are discretized and solved over through the finite-element method (FEM). The finite element method is based upon reformulation of governing partial differential equations as integrals, known as the “weak form”(J. N. Reddy & Gartling, 2010). These weak form integrals can then be approximated via linear algebra to evaluate heat transfer, meaning problems can be solved through matrix operations rather than iterative algorithms.

This means that computational time for finite elements is directly proportional to the number of elements, meaning that fine meshes with many elements can result in disproportionately long solution times (Segerlind, 1976). FEM's typical solution time makes it an unlikely candidate for inverse modeling procedures, but a simplified, speed-optimized finite element approach could make finite elements an attractive candidate due to their robust numerical stability and high accuracy.

The finite element method is often utilized for its ability to solve 2-dimensional heat transfer and is showing up more and more to evaluate the performance of phase-change materials in building envelopes (Alawadhi, 2008, 2012; Hasse et al., 2011). While this is a useful tool to evaluate the performance of phase-change materials, phase change materials are currently rarely found outside of lab settings. In the future, these models may become more popular for assessments, but only after phase-change materials see widespread market adoption.

Another frequent use of the finite element method is for hygrothermal modeling of facades. Hygrothermal models solve coupled systems of equations to model heat, moisture, and sometimes air transfer through elements, with finite element hygrothermal models becoming increasingly more widespread (Janssen et al., 2007; Khoshbakht et al., 2009; Lü, 2002; Pallin et al., 2017). There is even a current push to add moisture transport into the US DOE's popular THERM tool to expand its capability as a dynamic façade component evaluation tool (Curcija & Pallin, 2018). Hygrothermal finite element models typically utilize computationally expensive nonlinear solvers to deal with the drastic nonlinearity of moisture equations (Khoshbakht et al., 2009).

Finite element models seem to be less frequented in inverse modeling due to their large computational requirements. This does not entirely stop the method's use, as it was first used in 1978 by Krutz et al. to characterize the thermal properties of a heated rod (Krutz et al., 1978). Krutz et al. showed that this inverse finite element method model can predict thermal properties with much success in 1D. This work was followed by Tseng et al. in 1995 who developed a 2D finite element inverse which showed much promise (Tseng et al., 1995). Finite element inverse modeling was not directly applied to the building industry until van Schijndel utilized COMSOL to characterize the hygrothermal properties of a façade with marginal accuracy (van Schijndel, 2009). Regardless of the experiment's accuracy, van Schijndel emphasized the importance of their method and potential for future façade characterization applications, i.e. thermography. Another relevant application of inverse modeling with finite elements was Aïssani et al.'s characterization of insulation compression defects via 3D finite elements (Aïssani et al., 2016). This work was complex and computationally expensive but has relevance and novelty for applying inverse modeling to envelope defects.

2.2.3 Conduction Transfer Function and Response Factor Models

The conduction transfer function (CTF) and response factor methods are currently the most widely used means of solving heat conduction problems within the field of building energy modeling (X. Q. Li et al., 2009). These methods allow for the computation of heat transfer by relating current output to past outputs via time-invariant coefficient matrices. The first proposition of a transfer function is the thermal response factor created by Mitalas and Stephenson (Mitalas & Stephenson, 1967). The conduction transfer function method allows for transient heat transfer to be computed through the use of time-series temperatures and fluxes without the need for finite differencing or repetitive matrix inversion via pre-calculated coefficient vectors. Peavy (Peavy, 1977), Hittle and Pedersen (D C Hittle & Pedersen, 1981), Seem (Seem, 1987), and Li et al. (X. Q. Li et al., 2009) all developed methods to calculate coefficient vectors for layered wall assemblies, two-dimensional thermal bridging, and even entire rooms. Utilizing these procedures, CTFs became the go-to method for modern energy simulation after being implemented in DOE-2 (Koschenz, 1999; York & Cappiello, 1981), TARP (Walton, 1983), and BLAST (Douglas Carl Hittle, 1979), which are all predecessors of modern EnergyPlus. Due to the two programs merging to form EnergyPlus, the CTF method also became the standard method to calculate conductive heat transfer in building energy simulation (DOE, 2021a; R. Strand et al., 1999; R. K. Strand, 2001).

Building off of the widespread usage of the CTF method, Spitler et al. developed the Radiant Time Series Method as a simplified alternative to the heat balance method popular in energy simulation (Spitler et al., 1997). Within this proposed method, a closed-form solution for the CTF method was developed, called the Conduction Time Series Method (Spitler & Fisher, 1999). The Conduction Time Series method has also been referred to in the literature as the Periodic Response Factor method. Regardless of the naming, this method generates a singular coefficient vector representing the transient thermal performance of an assembly, referred to as a Conduction Time Series (CTS) factor, building off of the multiple complex CTFs present within the transport function method. After being published in the 1989 edition of the ASHRAE Handbook (ASHRAE, 1989), the process became a popular method to calculate building thermal loads. The CTS method, as Spitler and Fisher propose, utilizes a vector of time-dependent response factors known as the conduction time series. A sample conduction time series factor is displayed in Figure 2.5.

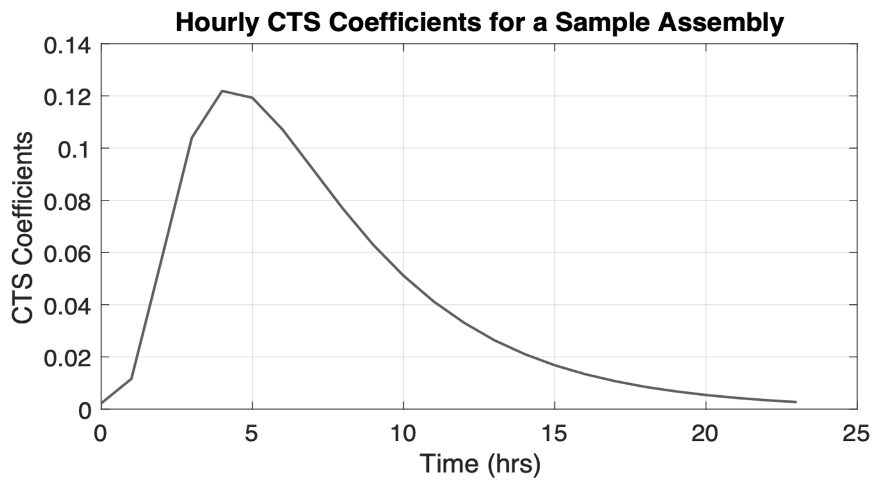

Figure 2.5 A plot of a sample internal surface conduction time series factor.

The CTS coefficients shown in Figure 2.5 represent the percentage of steady-state heat transferred through a surface from the past to the present. In a way, the CTS shows which percentage of the current and past steady-state heat fluxes are transmitted at the current time timestep. For example, the interior surface of an assembly represented by the CTS in Figure 2.5 would experience 0% of the steady-state heat transfer from this hour, 0.5% of the steady-state transfer from 1 hour ago, 0.75% of the steady-state transfer from 2 hours ago, and so on. While the conduction time series and conduction transfer function differ in implementation, both methodologies are fundamentally similar—heat transfer is evaluated via a vector of coefficients computed from assembly layering and thermal properties.

To utilize the CTS method, the building element's total R-value or U-factor must be known, alongside a vector of CTS coefficients representing the thermal mass of the element. While the CTS of coefficients contains more variables than the thermal capacitance term of lumped capacitance method, this CTS vector can accurately simulate the effects of thermal mass compared to apparent thermal capacitance. This method also only requires a single computation of the CTS and can be utilized without the need for matrix inversion or iteration, unlike the finite element and finite difference methods. The one major downfall of the CTS method is the need for a vector of coefficients rather than a singular coefficient to represent thermal mass, similar to ISO 9869's dynamic method.

While transfer functions are a widely popular method for thermal modeling, they are not as frequently used in inverse modeling. J.E. Braun used a mix of transfer functions and lumped capacitance models to create an inverse model of indoor temperature and characterize building envelopes for many years (Braun & Chaturvedi, 2002; Cai & Braun, 2012; Lee & Braun, 2016), and is one of the only authors to have utilized conduction transfer functions for explicit façade characterization.

Since transport functions are the primary forms of conduction heat transfer calculation in DOE2, BLAST, and EnergyPlus, most calibration and inverse modeling exercises in these energy modeling programs can be reformulated for calibration of facades. This means that the body of research on energy modeling calibration is all relevant and can be applied to characterize a building's façade using thermal loads, energy usage, and modeled surface temperatures. (Chaudhary et al., 2016; Haberl & Bou-Saada, 1998; Heo et al., 2012; T. A. Reddy, 2006; Royapoor & Roskilly, 2015; Yoon et al., 2003).

2.3 Comparison of Transient Conduction Calculation Approaches

Formal testing and peer review are the basis on which the scientific process stands. Without regulated testing or standardized references, immense model complexity can stand as a major barrier to verifying a scientific approach's validity. This problem also plagues building energy simulation, where models frequently employ complex, spatially defined zonal models to simulate heat transfer and energy usage at the building or urban scale. At such a scale, it can become difficult to diagnose model discrepancies due to the infinitely large combinations of model inputs and vast interconnectivity of model branches, independent solvers, and coupled heat transfer modes. To address this problem, the American Society of Heating, Refrigeration, and Air-Conditioning Engineers (ASHRAE) sponsored research project 1052-RP to develop standardized analytical tests to verify the performance EnergyPlus's building envelope simulation approach (Henninger & Witte, 2011). This project developed a software toolkit and 16 analytical tests to verify EnergyPlus's envelope heat transfer simulation models. As stated in a retrospective publication by Witte, Henninger, and Crawley, "[ASHRAE 1052-RP] tests cover a variety of building envelope mechanisms including conduction, convection, solar gains, shading, infiltration, internal gains, radiant transfer, and ground coupling." (Witte et al., 2016). Building off of this work, the ASHRAE 1052RP toolkit and its reference simulations provide a unique opportunity to compare many of the heat transfer calculation approaches highlighted in the chapter against a baseline in a controlled environment.

As stated by Witte et al., the goal of ASHRAE 1052RP is to develop a test suite to evaluate the performance of energy modeling software for a variety of usage cases.

ASHRAE 1052RP is a combination of many different solutions approaches for the physics-based equations solved in energy modeling software, so the project was structured as a series of case studies simulating various building physics phenomena on the component scale. The relevant case studies present within ASHRAE 1052RP are as follows:

- Test #4: Transient Conduction with Step Response
- Test #5: Transient Conduction with Sinusoidal Response and Multi-Layered Assembly

These two ASHRAE 1052RP tests, Test #4 and Test #5, respectively referred to as Transient Conduction 2 and 3 (TC2 and TC3) in the toolkit, are relevant to the performance assessment of transient heat transfer computation approaches. Utilizing these two transient conduction tests, various transient heat transfer algorithms can be simulated for the given scenarios and compared against the ASHRAE 1052RP baseline. To compare the various techniques, a 50-node Galerkin finite element model (J. N. Reddy & Gartling, 2010), a 20-node finite volume model, a 4R3C lumped capacitance model (DOE, 2021a), and transport function model (Spitler & Fisher, 1999) were implemented in MATLAB and simulated for both 1052RP test cases. This testing was designed to compare the performance of each of these algorithms to aid in model selection for subsequent sections of this dissertation.

To compare the performance of each of these models relative to the reference ASHRAE 1052RP analytical solutions, root-mean-square error (RMSE) was utilized. RMSE can be computed via the following equation:

$$RMSE = \sqrt{\frac{\sum_{i=1}^{n}(y_i - \hat{y}_i)}{n}} \tag{11}$$

Where y is the measured value, $\hat{y}$ is the modeled value, and n is the total number of data points. RMSE is advantageous due to its ubiquitous usage in scientific computing and generalizability regarding variable dataset sizes. It is a strong metric for comparing the relative performance of two models against one another.

2.3.1 TC2: Transient Conduction with Stepped Responses

In the ASHRAE 1052RP toolkit, the first relevant test is a simulation of a single-layered wall assembly with two different step responses on the exterior ambient temperature. The exterior convection coefficient for the assembly was set to 10.22 W/m^2-K, the interior convection coefficient for the assembly was 3.076 W/m^2-K, infrared radiation was neglected, the interior ambient temperature was held constant at 20°C, and the wall assembly was comprised of one material with a thermal resistance of 0.714 m^2-K/W and a thermal mass of 125 kJ/K. In this case study, the exterior ambient temperature is stepped up from 20°C to 70°C and held at that temperature for approximately 2159 hours. After this long period, the exterior ambient temperature undergoes a step response from 70°C to -30°C. While the original case study holds the exterior ambient temperature at 70°C for approximately 86 days to approach the steady-state response of the assembly, this is an unnecessarily long period to allow the assembly to warm up. This unnecessarily long period was reduced to 105 hours for ease of analysis, computational time, and visualization for the case study simulated in this work. Shortening this long, stationary period should not have any effect on the transient performance of the assembly during the step-up and step-down periods. All simulations were also simulated with a warm-up time of 72 hours before the analysis period to allow for each transient algorithm to "warm-up" from each model's respective initial conditions.

With these environmental conditions and material properties as inputs, the four transient heat transfer algorithms were simulated and compared to the ASHRAE 1052RP baseline. Due to the diverse nature of the heat transfer algorithm formulations, different options were utilized for each formulation. For the four heat transfer algorithms, the following options were implemented for this test case:

- For the finite element method, 50 1-dimensional nodes were simulated and solved via the Galerkin finite element method.
- For the finite volume method, 25 1-dimensional nodes were simulated and solved via the Crank-Nicholson method.
- For the lumped capacitance method, the one-layered assembly was modeled with a 4R3C network. This network was solved with MATLAB's ODE45 differential equation solver with variable time-stepping.
- For the conduction transport function approach, the assembly was modeled in the Oklahoma State University's PRF/CTF Generator tool to generate the transfer function (Iu, 2002). This transfer function was utilized in the TC2 simulation.

Utilizing these options and model setups, the test case was then run and compared against the ASHRAE 1052RP baseline. These results can be seen below in Figure 2.6.

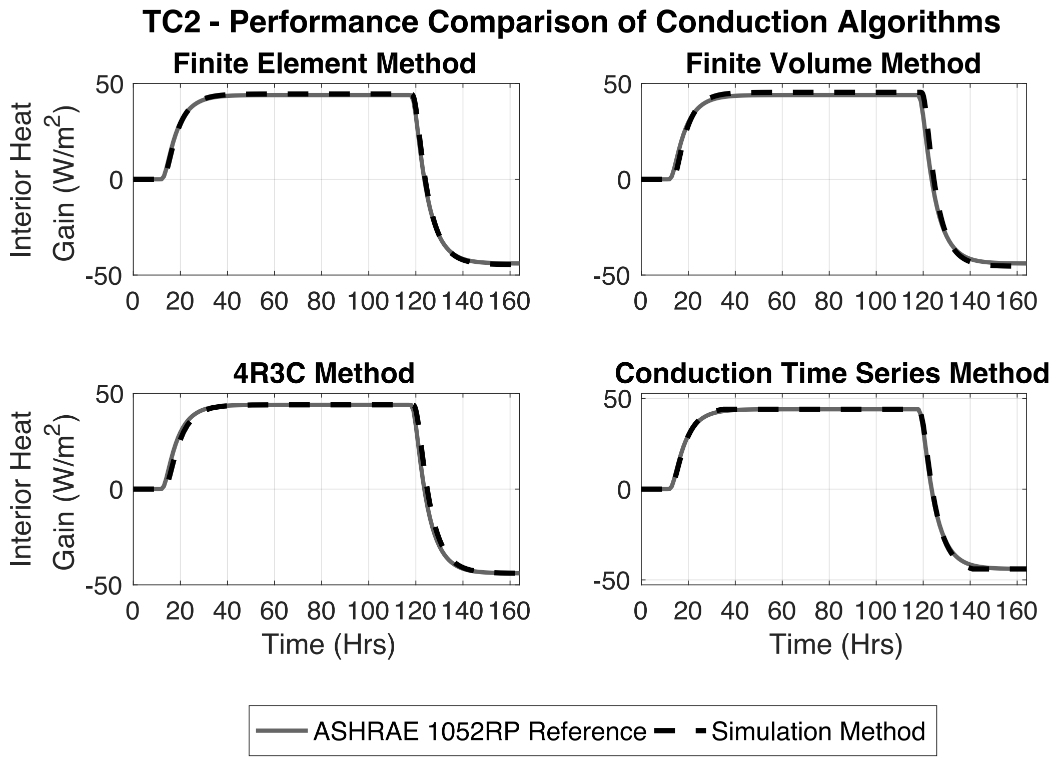

Figure 2.6 Four plots displaying the performance of different transient heat transfer algorithms for the ASHRAE 1052RP TC2 Step-Response test.

From the above figure, the performance of transient finite element, transient finite volume, 4R3C (lumped capacitance), and conduction time series methods can be seen compared against the ASHRAE 1052RP baseline. Each of the methodologies closely match the results of the reference data, indicating strong transient performance in response to drastic changes in environmental conditions. Each algorithm matches the reference data for the “step-up” region of the plots; however, the finite volume and 4R3C models appear to be slightly under-predict heat gain during the warm-up period. The FVM also appears to have over-predicted the heat flux by approx. 1.40 W/m^2 during the steady-state regime. Once again, all four algorithms display performance closely matching the reference assembly for the “step-down” portion of the test, with FVM and 4R3C models once again lagging the reference data during the transient regime. Additional results of this test can be viewed in Table 2.1.

Table 2.1 A tabulated performance summary of heat transfer algorithms for ASHRAE 1052RP Test TC2.

Model Type	Root-Mean Squared Error (W/m^2)	Computation Time (Seconds)
Finite Element	0.934	0.147
Finite Volume	1.52	0.244
RC Model	2.44	0.229
Conduction Time Series	0.757	0.00448

From Table 2.1, the performance of each respective transient heat transfer algorithm can be assessed in further detail. All four algorithms displayed low RMSE values with the reference dataset, with cumulative RMSE errors all below 2.00 W/m^2 for the test case. While accuracy is important when assessing models, another important facet of model performance is computational speed. When considering the tens-of-thousands of times a model will be computed in an inverse modeling problem, incremental speed increases compound to become much more impactful. When viewing the speed of all four of the tested models, all four formulations computed the 165 hours of data in under 1 second. While all four models are relatively efficient, the two models that stand out the most are the finite element model and the transfer function model, which are computed in 147 and 4.48 milliseconds, respectively. With this information, the transport function approach seems to be a strong candidate for inverse modeling; however, it should be noted that the transport function for this assembly was generated manually via the PRF/CTF Generator tool. There currently is no existing methodology to translate a transport function back to a list of material properties, which makes inverse modeling utilizing transport functions or conduction time series vectors a near-impossible task. In light of this information, the transient 1D finite element method becomes the most relevant methodology for inverse modeling.

2.3.2 TC3: Transient Conduction with Sinusoidal Response

The second relevant ASHRAE 1052RP case study is "Test TC3 - Transient Conduction, Sinusoidal Driving Temperature and a Multi-Layer Wall." As the title suggests, this test simulates the transient heat transfer performance of multi-layered assembly subjected to sinusoidal environmental conditions. The multi-layered assembly was exposed to a sinusoidal exterior temperature which ranged from -15°C to 15°C with a period of 24 hours. The exterior convection coefficient for the assembly was set to 10.22 W/m^2-K; the interior convection coefficient for the assembly was 3.076 W/m^2-K, the interior ambient temperature was held constant at 20°C; and the multi-layered assembly was comprised of three materials with thermal resistances of 0.7143 m^2-K/W, 0.5 m^2-K/W, and 0.5 m^2-K/W, respectively. The layers of the assembly also had thermal capacitance values of 35 kJ/K, 0.5 kJ/K, and 40 kJ/K, respectively per layer. This test case was simulated for 176 hours with the ASHRAE 1052RP toolkit and was compared against MATLAB implementations of the transient finite element method, the transient finite volume method, the 4R3C lumped capacitance method, and the conduction transfer function method. As with Test TC2, custom options were applied to each implemented heat transfer approach. Algorithm options are the same between Test TC2 and TC3, but it should be noted that the transport function was re-simulated with the PRF/CTF Generator to match the new three-layer assembly. The results of Test TC3 are displayed in Figure 2.7.

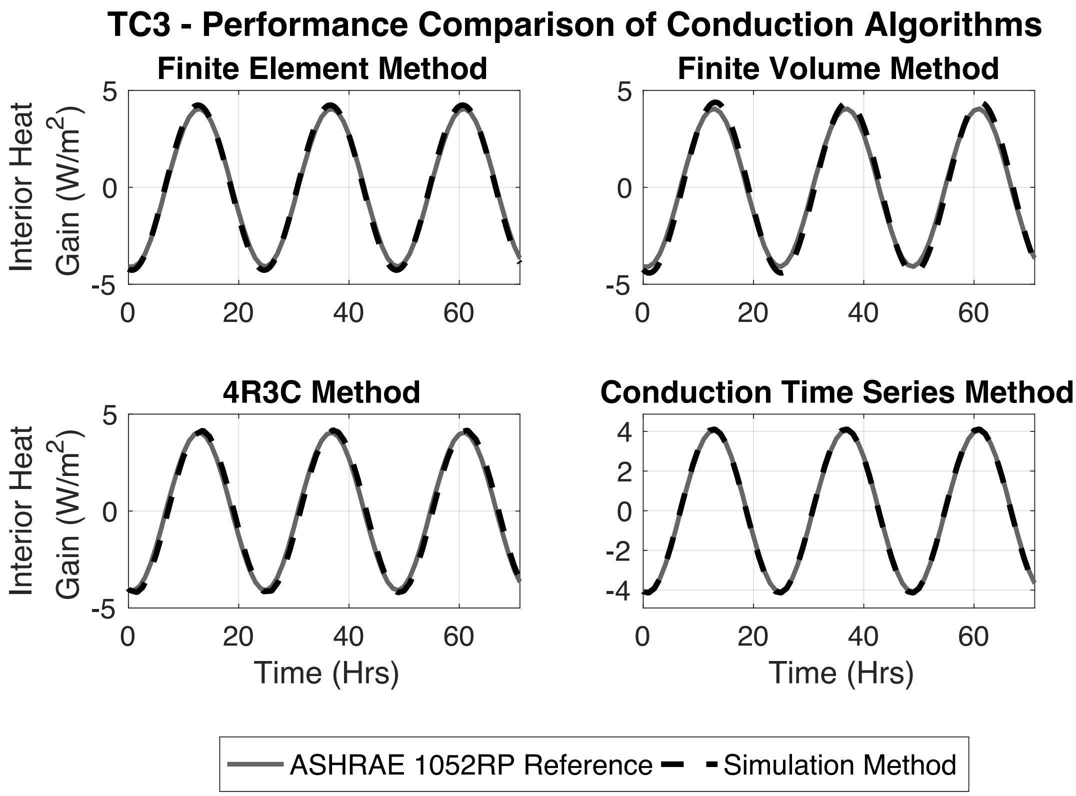

Figure 2.7 Four plots displaying the performance of different transient heat transfer algorithms for the ASHRAE 1052RP Test TC3.

From the above figure, the performance of transient finite elements, transient finite volume, lumped capacitance, and conduction time series methods can be seen compared against the ASHRAE 1052RP baseline for Test TC3. As with Test TC2, all of the methodologies closely match the results of the reference data, indicating strong transient performance in response to drastic changes in environmental conditions. Each algorithm matches the trend of the ASHRAE 1052RP reference data; however, a minor overprediction can be seen with the FEM and FVM approaches. As with the TC2 test, FVM and the RC model appear to be lagging the reference data in the transient regime, which is the entire duration of the entire TC3 test. Despite these minor issues, each of the models appear to match the heat flux at the interior surface of the 1052RP reference data closely. Additional results of this test can be viewed in Table 2.2.

Table 2.2 A tabulated performance summary of heat transfer algorithms for ASHRAE 1052RP Test TC3.

Model Type	Root-Mean Squared Error (W/m^2)	Computation Time (Seconds)
Finite Element	0.181	0.112
Finite Volume	0.598	0.985
RC Model	0.298	0.239
Conduction Time Series	0.0653	0.00516

Once again, the finite element and transfer function methods differentiate themselves due to low RMSE values and computation times. These results mirror that of TC2, where all algorithms appear to be sufficiently accurate for inverse modeling, but finite elements and transfer function methods drastically out-perform finite difference and lumped capacitance methods in terms of computational speed. The low speeds of finite volume and lumped capacitance methods are due to the low numerical stability of both approaches. From testing, it was noted that both approaches seem to become unstable with Fourier numbers less than 0.5. To account for this, both approaches handle this problem similarly—the lumped capacitance approach lowers the model's Fourier number via adaptive timestep throttling, where MATLAB's ODE45 solver adaptively adjusts individual timesteps to maintain numerical stability. The explicit implementation of the finite difference method utilized also reduces timesteps to maintain stability; however, this approach lacks an adaptive time-stepping approach and instead adjusts every timestep throughout the simulation period. Regardless of the timestep-altering approach, both the finite difference method and lumped capacitance methods struggle with numerical stability which is reflected in their computation times.

2.4 Concluding Remarks

In conclusion, 67 papers were evaluated within this literature review, all with different approaches and different applications. The literature review showed that certain modeling approaches performed well for specific tasks and not for others. Due to the number of thermal model typologies available, each must be classified for users to choose the correct approach for their problem. A tabulated, subjective scorecard for each modeling methodology is displayed in Table 2.3.

Table 2.3 A tabulated summary of reviewed heat transfer modeling techniques.

Model Type	Relative Computation Speed	Relative Model Accuracy	Relative Inverse Modeling Potential	Approx. Implementation Time (Hours)
Finite Element	2	3	3	35
Finite Volume	2	2	2	4
RC Model	1	2	3	10
Conduction Time Series	3	3	1	1

From the above table, subjective scores for each transient heat transfer algorithm can be evaluated for many different criteria. From the previous section, finite element and transfer function method approaches both compute heat transfer with relatively low computational overhead and high accuracy. It is also noted that the transport function method does not lend itself to an inverse modeling process due to the additional step of inferring thermo-physical properties from the inferred transfer function. Another important factor to consider is the ease of implementation for each approach. This data was approximately timed from the implementation of each method in the previous section. It should be noted that all of the approaches were adapted from published methods reported in technical reports and books. This implementation barrier can be overcome if these algorithms were released as open-source material, which would significantly reduce the implementation time of even the most complicated of approaches.

CHAPTER 3: THEORY

To evaluate the potential to characterize buildings' façade performance, a transient thermal model was developed. This model computes the heat transfer and surface temperature of the interior and exterior surfaces of the building element, allowing for comparison with the measured sensor data. A summary of the modes of heat transfer computed within this model can be seen graphically in Figure 3.1.

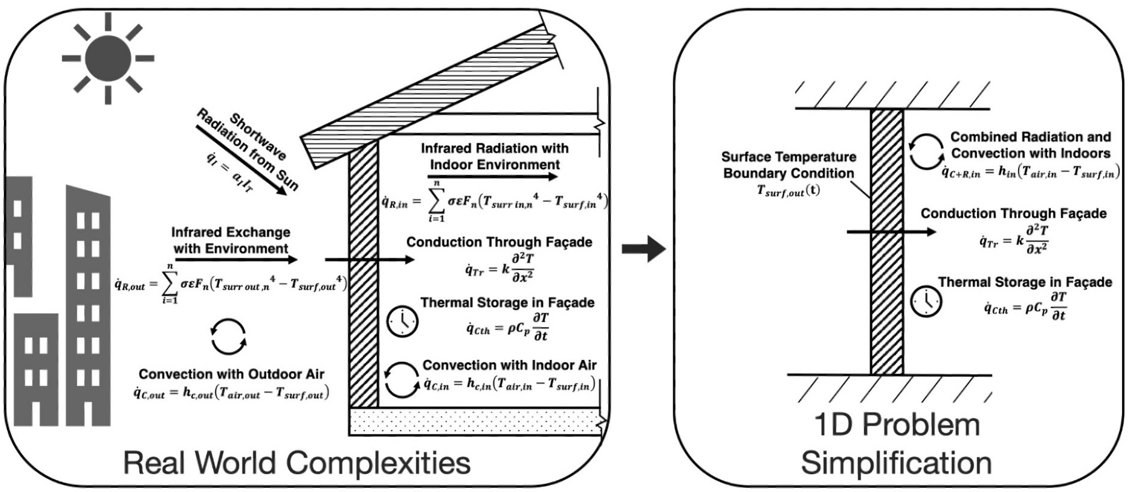

Figure 3.1 A graphical representation of the heat transfer modes influencing façade performance, which can be reduced to a simplified system with the use of a surface temperature measurement.

In the above figure, a variety of modes of heat transfer are displayed. Shortwave radiation, longwave radiation, and convection heat exchange with the outdoor environment all interact with exterior surfaces of the façade, transient conduction occurs through the façade element, and combined longwave radiation and convection with the indoor environment occurs the façade's interior surface. Balancing all of these modes heat transfers among their respective surfaces can provide the interior and exterior surface temperatures of the façade element, which in turn can be utilized to characterize the thermal properties of the façade element in 1D. This approach is very similar to that outlined in ASTM C1155.

Computing the various modes of heat transfer on the exterior of a façade element is no simple task; numerous environmental and local variables contribute to heat transfer. This complexity motivates the usage of the heat balance approach seen everywhere in building physics. While it may seem like a monumental task to characterize the thermal performance of a façade under all of these time-dependent factors and heat balancing, the task can be drastically simplified with the usage of a surface temperature measurement. Shortwave radiation, environmental longwave radiation, and local convection all contribute to the exterior surface temperature of the façade element, meaning that they can be represented in the exterior surface temperature of the façade. If all forms of exterior heat transfer are represented as a surface temperature, the complexity of the heat balance approach can be avoided and applied as a simple temperature boundary condition in a 1D transient conduction problem. Interior surface heat transfer can also be simplified as a combined longwave-convection heat transfer coefficient since most interior partitions can be assumed to be the temperature of the interior air. An illustration of this simplification can be seen in the latter half of Figure 3.1.

In the following sections, the simplified modeling framework proposed in Figure 3.1 are explored in further detail. Descriptions of the unsteady conduction computation, interior boundary conditions, characterization objective function, and Bayesian inference workflow are all displayed to provide context into the thermal characterization methodology. The theory is consistent with that which is utilized for thermal characterization throughout subsequent chapters of the dissertation.

3.1 Transient Conduction

In the early sections of this work, many different methods to compute transient conduction were proposed and reviewed. There are many different candidate methods shown here, but the method selected was a transient, Galerkin implementation of the finite element method (FEM). This FEM implementation was reduced to its most basic operations implementation and optimized for speed. As a result of these incremental changes, the implementation of the FEM utilized within this work can compute annual transient conduction at speeds in the tens of milliseconds, nearly as fast as tested implementations of the CTF method implemented in modern energy modeling software. FEM is also a very attractive method for this application due to its robust numerical reliability at many different timestep intervals.

Since this work is focused on the application of the FEM rather than research on the FEM, this section will focus purely on the numeric implementation and process of this FEM approach. This approach is an adaptation of Lawrence Berkley National Laboratory's HygroThermFEM engine, which is a fully transient implementation of the Galerkin finite element method (Vidanovic et al., 2021). This engine has been heavily validated and is at the core of THERM 8.0's transient heat transfer and moisture calculation engine. Due to the scope of this work and the associated computational overhead, all moisture-related components were omitted from this implementation of the HygroThermFEM engine.

If more information is needed on the background and details of the FEM, one should reference a book such as *The Finite Element Method in Heat Transfer and Fluid Dynamics* by Reddy and Gartling (J. N. Reddy & Gartling, 2010), which was referenced many times during the formulation of this engine.

3.1.1 Basis of Formulation

To begin, the goal of this finite element implementation is to approximate a solution the two-dimensional Fourier-Biot equation. This equation is as follows:

$$\rho C_p \frac{\partial T}{\partial t} = \frac{\partial}{\partial x}\left(k_{xx}\frac{\partial T}{\partial x}\right) + \frac{\partial}{\partial y}\left(k_{yy}\frac{\partial T}{\partial y}\right) + \dot{q} \tag{12}$$

Eq. 12 will be solved under appropriate boundary and initial conditions. It should be noted that this implementation is an adaptation of a two-dimensional finite element workflow, and thus includes y-coordinates. For this application, it is suggested to utilize y coordinates with infinitesimal differences (i.e. of the order of 10^-25). These small differences in y-coordinates temperature variability in the y-direction, effectively making the solution pseudo-one dimensional calculation in the x-direction. For additional context, a diagram displaying the coordinates on a sample wall section is displayed in Figure 3.2.

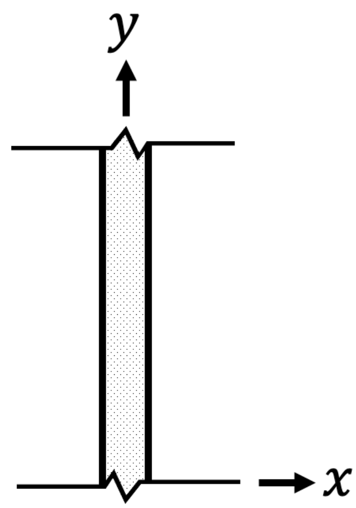

Figure 3.2 A sample envelope assembly section with cartesian coordinates displayed.

This numerical solution of this initial-boundary problem will be solved in a two-step process. The first step is a special discretization and development of the weak form through finite elements. The second step is a spatial approximation of the time-dependent temperature field across the simulated case. The finite element discretization is described first below in Section 3.1.2.

3.1.2 Finite Element Spatial Discretization

One foundation of the FEM is the distinction between nodes and elements. This implementation of the finite element method utilizes linear elements that each contain four nodes at element corners. An element is a collection of nodes that are connected by edges, and nearly all operations are done at the element-by-element level. A 2D example of the relationship between nodes and elements can be seen below in Figure 3.3.

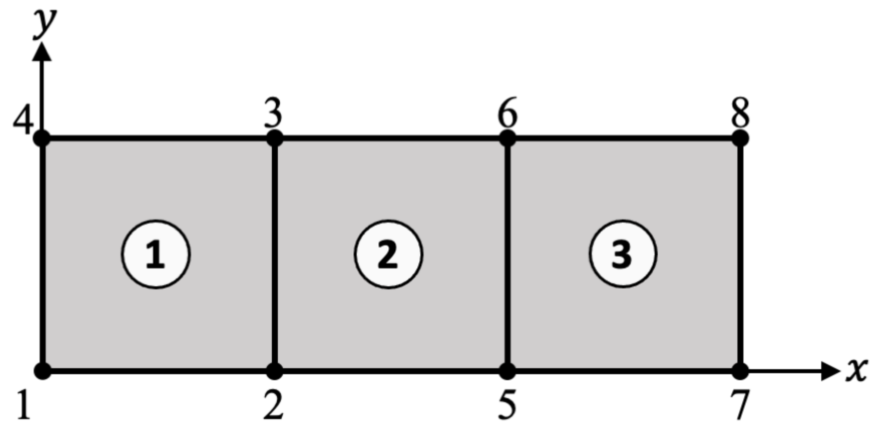

Figure 3.3 A representation of nodes and elements in 2D.

In the above figure, nodes are denoted as numbers near points, and elements are denoted as numbers inside of a circle. Nodes bound the corners of each element, and nodes are shared between neighboring elements. In this implementation, each node is provided a cartesian x- and y-coordinate, and each element contains an individual specific heat, density, and thermal conductivity. While nodes are denoted a global-coordinate location on the cartesian plane, nodes are also provided local coordinates on a local element plane centered at each element. This plane is denoted by η and ξ. A sample of this local coordinate system can be seen below.

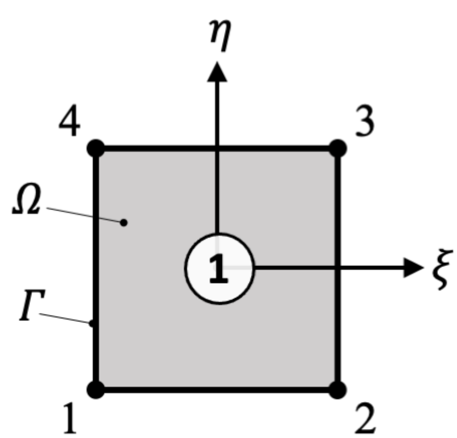

Figure 3.4 A representation of local element coordinates using Element 1.

From Figure 3.4, a singular finite element in the associated local coordinate system can be seen. This element is comprised of edges denoted by Γ, and an area denoted by Ω. It should also be noted that all element operations within this implementation act in a counterclockwise direction beginning at the bottom left node, which is denoted as Node 1 in Element 1. Nodes locations in the local coordinate system are referred to as Gauss points, which are at a Gauss quadrature distance E from the local origin. A Gauss quadrature distance of $\frac{1}{\sqrt{3}}$ with an associated Gauss integration weight of 1 was utilized for the rectangular elements in this implementation. The local coordinates of the nodes are as follows:

$$\xi = [-E \quad +E \quad +E \quad -E] \tag{13}$$

$$\eta = [-E \quad -E \quad +E \quad +E] \tag{14}$$

Where local coordinates are measured in a counterclockwise direction from the top left. These local coordinates can then be used to compute the shape, or interpolating, functions for the rectangular element. The shape functions for each Gauss point in the element can be computed by the following:

$$\Psi = 0.25 \begin{bmatrix} (1-\xi)(1-\eta) \\ (1+\xi)(1-\eta) \\ (1+\xi)(1+\eta) \\ (1-\xi)(1+\eta) \end{bmatrix} \tag{15}$$

The next step is to find the partial derivatives of the shape function with respect to ξ and η. These partial derivatives can be computed by the following:

$$\frac{\partial\Psi}{\partial\xi} = 0.25\begin{bmatrix} -(1-\eta) \\ (1-\eta) \\ (1+\eta) \\ -(1+\eta) \end{bmatrix} \tag{16}$$

$$\frac{\partial\Psi}{\partial\eta} = 0.25\begin{bmatrix} -(1-\xi) \\ -(1+\xi) \\ (1+\xi) \\ (1-\xi) \end{bmatrix} \tag{17}$$

Using the above partial derivates, the partial derivatives of the local coordinates with respect to the global coordinates can be computed. This operation is shown in Eq. 18–21.

$$\frac{\partial X}{\partial\xi} = X\frac{\partial\Psi}{\partial\xi} \tag{18}$$

$$\frac{\partial X}{\partial\eta} = X\frac{\partial\Psi}{\partial\eta} \tag{19}$$

$$\frac{\partial Y}{\partial\xi} = Y\frac{\partial\Psi}{\partial\xi} \tag{20}$$

$$\frac{\partial Y}{\partial\eta} = Y\frac{\partial\Psi}{\partial\eta} \tag{21}$$

An infinitesimal area in one coordinate system can be transformed into another by the following equation, where the 2 by 2 matrix on the right-hand side is referred to as the Jacobian and denoted by J:

$$\begin{bmatrix} \frac{\partial\Psi}{\partial\xi} \\ \frac{\partial\Psi}{\partial\eta} \end{bmatrix} = \begin{bmatrix} \frac{\partial X}{\partial\xi}_{(1,1)} & \frac{\partial Y}{\partial\xi}_{(1,1)} \\ \frac{\partial X}{\partial\eta}_{(1,1)} & \frac{\partial Y}{\partial\eta}_{(1,1)} \end{bmatrix} \begin{bmatrix} \frac{\partial\Psi}{\partial X} \\ \frac{\partial\Psi}{\partial X} \end{bmatrix} \tag{22}$$

Using matrix transformation, the partial derivative of the shape function with respect to the global coordinates can be computed with Eq. 23. This Jacobian can be utilized to transform between local and global coordinate systems, as shown below. It should be noted that the process shown below should be computed for each row-column index combination.

$$\begin{bmatrix} \frac{\partial \Psi}{\partial X}_{(i,j)} \\ \frac{\partial \Psi}{\partial Y}_{(i,j)} \end{bmatrix} = J^{-1} \begin{bmatrix} \frac{\partial \Psi}{\partial \xi}_{(i,j)} \\ \frac{\partial \Psi}{\partial \eta}_{(i,j)} \end{bmatrix} \tag{23}$$

Additionally, it should also be noted that elemental areas (i.e. $dxdy$) can be transformed between element and global coordinate systems via:

$$dxdy = det\ (J) d\xi d\eta \tag{24}$$

Utilizing this equality, the conductance and mass matrices for the element can be written. The element conductance can be computed by the following:

$$K_{el} = \int_{\Omega_e} k \left(\frac{\partial \psi}{\partial x}\frac{\partial \psi}{\partial x} + \frac{\partial \psi}{\partial y}\frac{\partial \psi}{\partial y} \right) dxdy = \int_{\Omega_e} k \left(\frac{\partial \psi}{\partial x}\frac{\partial \psi}{\partial x} + \frac{\partial \psi}{\partial y}\frac{\partial \psi}{\partial y} \right) det\ (J) d\xi d\eta \tag{25}$$

Where k is the element thermal conductivity, $\det(J)$ is the determinant of the Jacobian, and $\frac{\partial \psi}{\partial x}$ and $\frac{\partial \psi}{\partial y}$ are the partial derivatives of the shape function with respect to the global coordinates.

Integrals defined over a rectangular element Ω_e can be numerically evaluated using the Gauss-Legendre formula:

$$\int_{\Omega_e} f(\xi,\eta)\, d\xi d\eta \ = \int_{-1}^{1}\int_{-1}^{1} f(\xi,\eta)\, d\xi d\eta \ \approx \sum_{I=1}^{M}\sum_{J=1}^{N} f\big(\xi_I,\eta_J\big)\, W_I W_J \tag{26}$$

Where f(ξ,η) is an arbitrary function being integrated along a rectangular element and W_I and W_J are the corresponding Gauss weights (specified to be 1 in this two-point formulation and can thus be ignored). Combining Gauss-Legendre formula shown in Eq. 26 with Eq. 25, the element conductance calculation can be expressed in matrix form:

$$K_{el} = k\left(\frac{\partial\Psi}{\partial X}\frac{\partial\Psi^T}{\partial X} + \frac{\partial\Psi}{\partial Y}\frac{\partial\Psi^T}{\partial Y}\right) det(J) \tag{27}$$

This matrix formulation provides a workable framework to numerically compute conductance matrix for each respective element. A similar methodology can be utilized to compute the element mass term, which is represented in Eq. 28.

$$C_{el} = \int_{\Omega_e} \rho C_p\, \psi(x,y)\psi(x,y)\, dxdy = \int_{\Omega_e} \rho C_p\, \psi(x,y)\psi(x,y)\, det(J)\, d\xi d\eta \tag{28}$$

Combining Eq. 28 with the equality of the Gauss-Legendre formula, the mass matrix can be computed:

$$C_{el} = \rho C_p\, \Psi\, \Psi^T\, det(J) \tag{29}$$

Where ρ is the element density, C_p is the element specific heat, Ψ is the shape function matrix, and $\det(J)$ is the determinant of the Jacobian. As with Eq. 27, this matrix formulation of the elemental mass term provides a work-able computation footing to calculate each the mass of each respective element.

Since this process is to compute the mass and conductance matrix for a singular element, the procedure computing using Eq. 13–29 should be repeated for each finite element and assembled into a global conductance and mass matrices. Due to the formulation of element numbers and coordinates present within this implementation, the global conductance and mass matrices can be generated as follows:

$$K_{GL} = \begin{bmatrix} K_{1\,(1,1)} & K_{1\,(1,2)} & K_{1\,(1,3)} & K_{1\,(1,4)} & 0 & 0 \\ K_{1\,(2,1)} & K_{1\,(2,2)} & K_{1\,(2,3)} & K_{1\,(2,4)} + K_{1\,(1,1)} & 0 & 0 \\ K_{1\,(3,1)} & K_{1\,(3,2)} & K_{1\,(3,3)} + K_{2\,(1,1)} & K_{1\,(3,4)} + K_{2\,(1,2)} & K_{2\,(1,3)} & K_{2\,(1,4)} \\ K_{1\,(4,1)} & K_{1\,(4,2)} & K_{1\,(4,3)} + K_{2\,(2,1)} & K_{1\,(4,4)} + K_{2\,(2,2)} & K_{2\,(2,3)} & K_{2\,(2,4)} \\ 0 & 0 & K_{2\,(3,1)} & K_{2\,(3,2)} & K_{2\,(3,3)} + K_{3\,(1,1)} & K_{2\,(3,4)} + K_{3\,(1,2)} \\ 0 & 0 & K_{2\,(4,1)} & K_{2\,(4,2)} & K_{2\,(4,3)} + K_{3\,(2,1)} & \ddots \end{bmatrix} \quad (30)$$

Eq. 30 displays the methodology for the formation of the global conductance matrix for this implementation of the FEM. The same procedure can be applied to the element mass matrices to form the global mass matrix. Following the generation of the global mass matrix, a lumped global mass matrix is made by summing the mass matrix rows and placing the sums in a diagonal matrix. The generation of the lumped mass matrix is optional, as the “lumping” step is only present to increase matrix inversion speed in subsequent steps. This process can be seen in the following:

$$C_{lump} = \begin{bmatrix} \sum_{i=1}^{n} C_{GL\,(1,i)} & 0 & 0 \\ 0 & \sum_{i=1}^{n} C_{GL\,(2,i)} & 0 \\ 0 & 0 & \ddots \end{bmatrix} \quad (31)$$

3.1.3 Convective and Radiative Boundary Conditions

Following the generation of the global conductance and mass matrices, the next step is to generate boundary conditions for the appropriate elements. For the rectangular finite elements utilized in this implementation, boundary conditions influence the finite element system along a node's edge. Due to this, boundary condition elements and their respective shape functions are treated as boundary elements, which have differing calculation processes than rectangular elements. While the element makeup is different, this process also starts with the generation of local coordinates and a shape functions. The local coordinate system and shape function for a boundary condition line element can be seen below.

$$\eta_{BC} = [-E \quad +E\,] \tag{32}$$

$$\Psi_{BC} = 0.5\begin{bmatrix} (1-\eta_{BC\,(1,1)}) & (1-\eta_{BC\,(1,2)}) \\ (1+\eta_{BC\,(1,1)}) & (1+\eta_{BC\,(1,2)}) \end{bmatrix} \tag{33}$$

Due to the simplified nature of the line element compared to a rectangular element, the Jacobian and determinant of the Jacobian are quite simple to compute for a line element. The equation for the determinant of the Jacobian for line elements can be seen below:

$$det(J_{BC}) = 0.5\sqrt{\Delta x^2 + \Delta y^2} \tag{34}$$

For this due to the nature of boundaries in this implementation, boundary conditions are treated as edge heat fluxes, which can be computed with the following equation:

$$\dot{q}_e = \oint_{\Gamma_e} \Psi_{BC}\,\dot{q}_a\,ds = \oint_{\Gamma_e} \Psi_{BC}\,\dot{q}_a\,det(J_{BC})\,ds \tag{35}$$

Where $\dot{q}_e$ is the heat flux applied to the element, Ψ_{BC} is the boundary element shape function, and $\dot{q}_a$ is the boundary heat flux. q_a can also be adapted to represent a convection or radiation heat flux with the usage of a convection or radiation film coefficient. This is show in Eq. 36.

$$\dot{q}_a = h(t)(T(t)_s - T_\infty(t)) \tag{36}$$

Where h is the heat transfer coefficient that can represent linearized radiation or convection film coefficient, T_s is the element surface temperature, and T_∞ is the ambient temperature. This surface temperature can be converted to elemental temperatures with the following relationship.

$$T_s(\eta, t) = \Psi_{BC} T(t) \tag{37}$$

Similar to Eq. 26, there is a Gauss-Legendre relationship to approximate line integrals as a summation:

$$\oint_{\Gamma_e} f(\eta)\, ds \ = \int_{-1}^{1} f(\eta)\, ds \ \approx \sum_{J=1}^{N} f(\eta_I)\, W_I \tag{38}$$

Combining this with Eq. 35, 36, and 37 results in:

$$\dot{q}_e = h(t)\, \Psi_{BC}\, \Psi_{BC}{}^T\, det(J_{BC})\, T(t) \ - \ h(t)\, T(t)\, \Psi_{BC}\, det(J_{BC}) \tag{39}$$

This equation can further be broken down into terms which are analogous to the conductance and mass matrices:

$$\dot{q}_e = H(t)\, T(t) - \ F(T) \tag{40}$$

$$H(t) = h(t)\, \Psi_{BC}\, \Psi_{BC}{}^T\, det(J_{BC}) \tag{41}$$

$$F(t) = h(t)\, T_\infty(t)\, \Psi_{BC}\, det(J_{BC}) \tag{42}$$

$H(t)$ is a term called the boundary conductance, and is analogous to the element conductance computed above. $\mathrm{F}(t)$ also has a name, it is called the boundary condition force term.

In this formulation, the boundary condition heat transfer coefficient can be made to be represent convection or radiation. The process is same for both, and both can be included in the finite element solution by adding the $H(t)$ and $F(t)$ terms together for both after each respective calculation. Boundary conditions must be recomputed at each timestep at each applicable surface since film coefficients and temperatures are consistently changing in most practical scenarios. These coefficients also must be applied into a global boundary condition matrix in combination with mass and conductivity matrices. In this FEM implementation, nodes are indexed in increasing order from the interior façade element surface to the exterior surface. Due to this, the indoor boundary condition matrices will be populated into the first indices of the global boundary condition conductance and force matrices, and exterior boundary conditions will be added into the final indices. This process is displayed below:

$$H_{GL}(t) = \begin{bmatrix} H_{in\,(1,1)}(t) & H_{in\,(1,2)}(t) & 0 & & \cdots & 0 \\ H_{in\,(2,1)}(t) & H_{in\,(2,2)}(t) & 0 & & \cdots & 0 \\ 0 \quad 0 & & 0 & & & \\ & & & \ddots & & \\ & & & 0 & & \\ \vdots \quad \vdots & & & & H_{out\,(1,1)}(t) & H_{out\,(1,2)}(t) \\ 0 \quad 0 & & & & H_{out\,(2,1)}(t) & H_{out\,(2,2)}(t) \end{bmatrix} \tag{43}$$

$$F_{GL}(t) = \begin{bmatrix} F_{in\,(1)}(t) \\ F_{in\,(2)}(t) \\ 0 \\ \vdots \\ 0 \\ F_{out\,(1)}(t) \\ F_{out\,(2)}(t) \end{bmatrix} \tag{44}$$

3.1.4 Element Temperature Calculation

To compute the elemental temperature of a general finite element, the following backwards difference equation can be utilized:

$$\frac{C}{\Delta t}\big(T(t+1) - T(t)\big) + (K + H)\,T(t+1) = F(t+1) \tag{45}$$

Rearranging this equation and converting it to the matrix notation utilized here, the following equation can be upon:

$$T(t+1) = \left(K_{GL} + \frac{C_{lump}}{\Delta t} + H_{GL}(t+1)\right)^{-1} \left(\frac{C_{lump}}{\Delta t}\,T(t) + F_{GL}(t+1)\right) \tag{46}$$

Where $T(t)$ is a vector of nodal temperatures at the current timestep, K_{GL} is the global conductance matrix, C_{Lump} is the lumped mass matrix, H_{GL} and F_{GL} are boundary conditions, and $T(t+1)$ is a vector of nodal temperatures at a next timestep. If standard SI units are used for all FEM calculations, the unit of each timestep will be in units of seconds.

It should also be noted that initial temperatures must be applied for the starting timestep, and the solution may take time to transition from these starting conditions to a viable solution. This is referred to as the "warm-up period". To reduce the impact of starting conditions, it is suggested that nodal initial temperatures be initialized with their steady-state temperatures at the starting conditions. The impact of the "warm-up period" can also be minimized by starting the simulation a few hours or days before the period of interest, depending on the thermal mass of the assembly.

3.2 Characterization Procedure and Objective Function

In this work, a two-stage characterization procedure is proposed: The first stage involves instrumentation of the real building, and the latter stage is an optimization-based inverse heat transfer computation. The proposed non-destructive sensor layout is summarized graphically below in Figure 3.5.

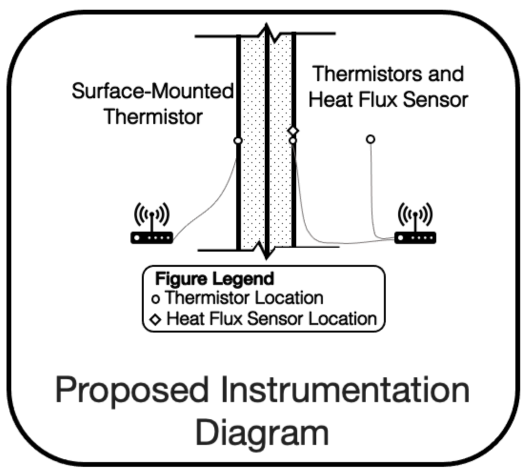

Figure 3.5 The proposed sensor layout for in-situ thermal characterization method proposed within this work.

In the above figure, the proposed sensor layout can be seen. Temperature sensors are located on the exterior surface, interior surface, and within the indoor space, and a singular heat flux sensor is placed on the interior surface of the assembly. The surface-mounted sensors must be mounted at the same position on the assembly to capture heat transfer occurring perpendicular to the assembly's face. This instrumentation approach differs from that of ASTM C1155's SLS method, as it allows for characterization without the need for sensors to be located inside the assembly, and instead locates sensors on the assembly's surfaces and within the indoor space.

With the assembly's performance measured through the proposed sensor layout, optimization can be used to determine the representative thermal properties of a façade element via the minimization of an objective function. The objective function and optimization statement is displayed within Eq. 47.

For the façade element of interest, minimize:

$$SSE = W_{\dot{q}} * \sum_{i=1}^{n} \left(\dot{q}_i - \hat{\dot{q}}_i(R,C)\right)^2 + W_T * \sum_{i=1}^{n} \left(T_{si,i} - \hat{T}_{si,i}(R,C)\right)^2 \quad (47)$$

Subject to:

$$0 < \mathrm{R} \leq 100\ \frac{m^2\text{–}K}{W}$$

$$0 < C_{th} \leq 1000\,\frac{kJ}{K}$$

Where $\dot{q}$ is measured surface heat flux at the interior surface of the assembly, T_{si} is measured surface temperature at the interior surface of the assembly, $\hat{\dot{q}}$ is the simulated interior heat flux, $\hat{T}_{si}$ is the simulated surface temperature of the interior-facing surface, R is the effective thermal resistance of the modeled homogeneous layer, C is the effective thermal capacitance of the modeled homogeneous layer, i is the timestep of simulation/measurement, n is the total number of timesteps present in the characterization, and $W_{\dot{q}}$ and W_T are the weights for heat flux and temperature, respectively. In this case, weights for both heat flux and temperature were set to be equal at 0.5 each to avoid biasing one metric over the other.

In plain terms, this objective function represents the difference between measured and modeled heat flux and surface temperatures on the interior-facing surface of an envelope assembly. Selection of different thermal resistances and thermal mass values result in modeled values which may be nearer or farther away from measured performance. Optimization algorithms can be employed to minimize the error between simulated and measured performance through search for the optimum combination R and C which minimize error. When optimum values are located, the optimum R and C are considered to be representative of a thermal analog for the measured assembly; an assembly which mirrors the heat transfer performance of the measured assembly.

The objective function is similar to that of ASTM C1155's SLS technique but was adapted for the proposed sensor layout. One major difference between the proposed method compared to ASTM C1155's SLS is the alteration of boundary conditions for the conduction problem. The SLS method utilizes temperature boundary conditions on the interior and exterior surfaces of the assembly of interest, while this approach utilizes the measurement of a temperature boundary condition on the exterior-facing surface and a convective boundary condition on the interior surface. Combined convection and thermal radiation film coefficient can be approximated utilizing the ASTM C1155 Summation method with the interior surface temperature sensor, the heat flux sensor, and the temperature sensor measuring the indoor air temperature.

The transient heat transfer is handled via the aforementioned FEM approach, where the heat transfer through a homogeneous layer of material that serves as an analog of the layered in-situ facade element. Any of the surveyed heat transfer algorithms could be utilized; however, special care must be taken to maintain numerical stability due to the convective boundary condition.

To evaluate characterization performance, RMSE was utilized to compare ground-truth data to thermal characterizations. The equation for RMSE is displayed as Eq. 11 in the previous chapter.

Another equation to evaluate characterization performance is normalized root-mean-square error (NRMSE). One major advantage of NRMSE over RMSE is the ability to be displayed as a percentage, allowing for interpretation as an absolute accuracy metric as opposed to a relative accuracy metric like RMSE. The equation for NRMSE is as follows:

$$NRMSE = \frac{RMSE}{y_{max} - y_{min}} \tag{48}$$

Where y_{max} and y_{min} are the maximum and minimum of the measured data, respectively.

3.3 Bayesian Inference

To characterize the thermal performance of assemblies via simulation, the simulation inputs must be computed. This is typically referred to in the literature as parameter estimation or parameter inference. Since the goal of this characterization optimization statement in Eq. 47 is to minimize the sum of squared error between simulated and measured heat fluxes across all timesteps, this characterization task can be approached with a variety of deterministic and stochastic approaches. For this research, Bayesian inference was selected due to its robust statistical underlying and prevalence in the literature.

In short, Bayesian inference is a methodology that allows for the inference of unknown parameters to update a model based upon measured data. To motivate this process, consider the following equation:

$$y = \hat{y}(\theta) + \epsilon \tag{49}$$

Where y is an array of measured data, $\hat{y}(\theta)$ represents an array of computed model results, θ is a vector of unknown model inputs, and ϵ represents error or model discrepancy of the form of $\epsilon \sim N(0, \sigma_{err}^2)$. In the case of this application, y represents sensor data from the measured assembly, and $\hat{y}(\theta)$ represents the modeled performance of the assembly. Utilizing this framework, the goal of this characterization process can be restated so that the process infers the model inputs which result in the model closely matches measured values. Bayesian inference calibrates the model in a stochastic fashion, allowing for interpretation of the inferred parameters to address modeling concepts such as model overfitting, certainty of results, and prior expectation. One of the most important aspects of Bayesian inference is the modeler's prior expectation of the inference's result. This concept can be illustrated via Bayes' Rule in Eq. 50.

$$p(\theta|y) = \frac{p(y|\theta)\, p(\theta)}{p(y)} \propto p(y|\theta)\, p(\theta) \tag{50}$$

Where $p(\theta)$ represents the prior distribution, which is a distribution motivated by the modeler's expectation of the results; $p(y|\theta)$ represents the likelihood function of the measured phenomenon; $p(\theta|y)$ represents the posterior distribution, which is an updated form of the prior distribution in light of the measurement data; and $p(y)$ is the normalization factor. Bayes' rule can also be rewritten as a simpler proportionality statement, which at high-level states: the posterior distribution is proportional to the likelihood function multiplied by the prior distribution. A more literal interpretation of Bayes' rule states that this framework allows for the updating of prior expectations in light of new knowledge, which in this case is measured data. One of the major hurdles of Bayesian inference is the difficulty of computing the normalization constant, $p(y)$ (Laine, 2008). For most practical cases, the computation of the normalization constant requires special Markov Chain Monte Carlo (MCMC) algorithms, such as Metropolis-Hastings (MH) (Hastings, 1970; Metropolis et al., 1953), Adaptive Metropolis (AM) (Haario et al., 2001), Delayed-Rejection (DR) (Peskun, 1973; Tierney & Mira, 1999), and Delay-Rejection Adaptive Metropolis (DRAM) (Haario et al., 2006). For this work, the DRAM algorithm by Haario et al. was employed for parameter estimation of the homogeneous thermal equivalent layer.

3.4 Chapter Conclusion

In conclusion, the methodologies and computational procedures described within this chapter provide the basis of a foundation to infer the effective thermal properties of an as-built building envelope assembly. Three major pieces of the transient characterization workflow were proposed within this chapter: 1) The transient conduction algorithm, 2) The sensor layout and characterization objective function, and 3) Bayesian Inference. These three aspects overlap and work together to enable thermal characterization of as-built envelopes.

First off, this chapter began with the proposal of a transient finite element heat transfer algorithm. This implementation of the finite element method was adapted from THERM 8.0 and optimized for speed and accuracy to enable rapid computation heat transfer within the stable and accurate framework of finite element heat transfer. Alongside the direct application to this thesis work, the finite element workflow displayed within Section 3.1 is also widely applicable to many different use cases within the field of thermal engineering. Throughout the literature survey and background reading conducted to formulate this methodology, it was noted that there are few works present within the literature that directly inform readers on the implementation of finite elements for the computation of transient heat transfer. This was one of the main motivations for displaying such detail; the hope is that this work may become a useful tool to reduce the uncertainty and specialized knowledge required to implement transient finite elements.

Secondly, this chapter displayed a heat transfer-based objective function to enable thermal characterization of building envelopes. This objective function utilizes the transient finite elements proposed within this chapter to compute the transient heat flux occurring at the interior surface of the envelope element. Utilizing this heat flux, the sum-of-squared error between the simulated and measured fluxes can be computed, allowing for an optimization algorithm, or a Bayesian inference algorithm, to be introduced to minimize the objective function, allowing for the simulated assembly to closely mirror the thermal performance of the candidate in-situ assembly.

Finally, a Bayesian inference workflow was motivated and proposed. Bayesian inference provides the opportunity to stochastically characterize the thermal performance of façade assemblies, leveraging the proposed finite element workflow and objective function. The main goal for the utilization of Bayesian inference is to reduce uncertainty and provide a clear, well-represented understanding of the measured assembly's performance, under measurement and sensor uncertainty. Haario et al.'s MATLAB DRAM toolbox was utilized within this work to enable Bayesian characterization.

Leveraging these three tools, it is now possible to characterize the thermal performance of as-built building envelopes. In subsequent chapters, these workflows will be utilized to characterize envelopes from measured data. This workflow can be applied to simulation studies and field data alike to better understand the transient thermal performance of as-built assemblies.

CHAPTER 4: SIMULATION-BASED VALIDATION

Within this chapter, a simulation-based study will be conducted to verify the performance of the proposed transient characterization workflow and better understand the workflow's intricacies within a controlled simulation environment. This entire chapter characterizes envelope assemblies which are simulated in EnergyPlus to verify the methodology's performance against known envelope assemblies.

4.1 Pilot Simulation Study Parameters

In this section, the parameters for an initial simulation-based pilot study are explored. This pilot study aims to be a proof-of-concept application of the Bayesian characterization workflow outlined in Chapter 3.

4.1.1 Assessment Building

To evaluate the performance of the inverse modeling procedures proposed in Chapter 3, a sample characterization exercise was applied to a simulated building. Usage of a simulated building allows for pilot verification of the approach in absence of real-world uncertainty. This data is also advantageous, since it mimics that of a real building assessment, while the thermal properties of the façade assembly are known. For this analysis, the DOE/IECC 2015 single-family reference building was utilized (Mendon et al., 2015). A screenshot of this building's energy model geometry is displayed in Figure 4.1.

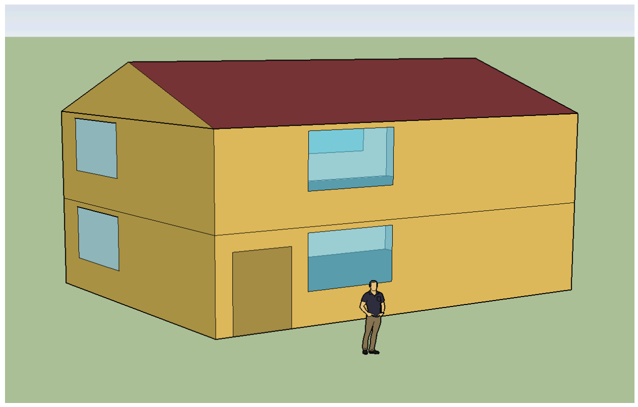

Figure 4.1 A view of the single-family reference building's geometry.

This building was selected because of its window-to-wall ratio, which is approx. 14% compared to the medium office reference building's window-to-wall ratio of 30%. This building also has significantly lower radiant loads, compared to other DOE/IECC reference building models.

To test the computational portion of the characterization workflow, the South-facing wall of the first was characterized with the proposed transient characterization methodology. Simulation of this building within EnergyPlus allows for surface temperatures of the interior and exterior and heat fluxes to be measured with controlled certainty and environmental factors, which acts as a stand-in for instrumentation and data collection on a real building. This measured data is also quite useful for this early-stage testing since it is free of measurement and calibration error characteristic of real-world experimentation.

In this exercise, the EnergyPlus virtual building was simulated for the Hartsfield-Jackson Atlanta TMY3 EnergyPlus weather file (DOE, 2021b). Exterior surface temperatures, interior heat fluxes, and interior air temperatures were measured from the model in 10-minute increments. Measured data from the first week of April for the simulation was separated into 48-hours of training data for characterization and 52 hours of evaluation data to characterize the simulated assembly and evaluate model performance.

4.1.2 Modeling Approach

The surrogate single-layer assembly was characterized to match its simulated heat flux with the measured interior heat flux. This was approached using finite elements and the open-source DRAM-based Bayesian inference MATLAB toolbox available at http://helios.fmi.fi/~lainema/dram/ (Haario et al., 2006). One of the main benefits of Bayesian inference is its speed and ability to conclusively infer a distribution of possible thermal resistance and thermal capacitances, rather than a single deterministic result. This allows for resultant posterior distributions to be evaluated to determine the certainty and accuracy of the stochastic thermal characterization.

In this study, relevant envelope thermal properties (effective thermal resistance and effective thermal capacitance) were inferred via Bayesian inference. The DRAM algorithm was used for the MCMC simulation and was allowed to run for 10,000 function iterations to allow for chain convergence as well as chain mixing. Within the Bayesian inference workflow, the transient finite element routine highlighted in previous sections was used. The finite elements are solved in 1D, allowing for observation of each node's temperature. For this characterization exercise, the façade element was given an arbitrary thickness of 0.3 m discretized into 50 finite element nodes along the assembly's thickness. Testing found that characterization solutions converged upon the same thermal resistances and thermal capacitances regardless of surrogate assembly thickness. While assembly thickness was not found to influence characterization accuracy, the number of simulated nodes was found to have influence. Through testing, it was found that 50 nodes struck a balance between execution time and FEM accuracy.

Alongside the selected heat transfer model, another modeling consideration for the Bayesian inference technique is the selection of quantified uncertainties and prior distributions. Since the data utilized in this test are simulation results, synthetic, controlled noise was added to the data to simulate measurement uncertainty which would be present in a physical experiment. To account for this, temperature measurements were assumed to be from a T-type thermocouple with a measurement tolerance of ±1.00°C (Omega Engineering, 2019). Little information could be located regarding heat flux sensor accuracy, so heat flux measurements were assumed to have a measurement tolerance of ±0.250 W/m^2. Both of these measurement errors were assumed to be normally distributed and were applied to all flux and temperature measurements via normally distributed Monte-Carlo sampling.

The secondary major consideration for Bayesian inference is the selection of a prior distribution to serve as an input to the MCMC algorithm. While the literature tends to disagree on the selection of prior distributions in light of no prior knowledge (Box & Tiao, 1973; Gelman et al., 2013; Tarantola, 2005), it is suggested that non-informed prior be utilized for starting the Bayesian inference search. For the cases where no prior is known for the Bayesian inference, a prior with infinite variance was employed to start the model without biasing results (Laine, 2008).

4.1.3 Wall Characterization Simulation Pilot

Utilizing the data provided via EnergyPlus simulation of the reference building, a multitude of tests can be run. In this work, the constructions simulated in EnergyPlus are sample constructions found in ASHRAE Fundamentals Chapter 18 (ASHRAE, 2013). Buildings with a low mass wall and a high mass wall were selected from the sample constructions, simulated in EnergyPlus, and characterized using the proposed methodology to simulate a real building assessment and test the methodology. The definitions of low and high mass walls can be seen in Table 4.1.

Table 4.1 ASHRAE Fundamentals wall assemblies utilized within the building simulation (ASHRAE, 2013).

Layer Number (Number Ext. to Int.)	Low Mass Wall (Wall #13)	High Mass Wall (Wall #63)
1	25mm Stucco (F07)	200mm Heavyweight Concrete (M15)
2	13mm Fiberboard Sheathing (G03)	89mm Batt Insulation (I04)
3	89mm Batt Insulation (I04)	89mm Batt Insulation (I04)
4	16mm Gypsum Board (G01)	16mm Gypsum Board (G01)

Using the walls shown in Table 4.1, two characterization trials were run and analyzed. Both assemblies were simulated in the EnergyPlus virtual building and assessed for the south-facing floor façade during a sample period in spring. These assemblies were assessed using the proposed transient characterization exercise and compared to measured and steady-state heat transfer values. Assemblies were characterized for 48 hours of training data measured at a frequency of every 10 minutes.

4.2 Simulation Pilot Characterization Results

4.2.1 Low Mass Wall Thermal Characterization

The first trial was conducted for Wall #13 utilizing 48 hours of heat flux measurements taken at 10-minute intervals. This "audit" was conducted on the first week of April simulated from an Atlanta TMY3 file for the building's southern face. The results of this study are presented below.

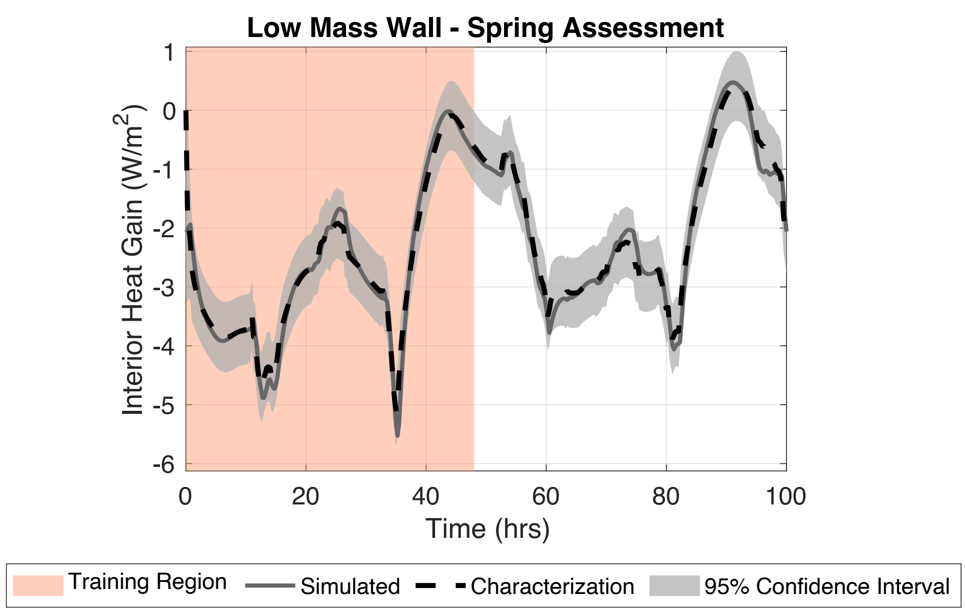

Figure 4.2 Plotted time-series interior heat gain from a 48-hour Bayesian characterization of a low mass wall (Wall #13).

From the above figure, the performance of the finite element characterization can be seen. This exercise characterized the façade element correctly for the spring simulation period with an RMSE of 0.308 (0.136, 0.688) W/m^2 with the values in parentheses denoting the 95% confidence interval for the RMSE. The 95% confidence interval for each timestep is also displayed within the plot, with the characterization appearing to have an uncertainty of approximately 1 W/m^2 due to the synthetic measurement error applied to the data. Despite this noise, the mean value of the characterization closely matches the simulated reference data. Alongside these results, the posterior distributions for the inferred parameters can be analyzed. Histograms of parameters are plotted in Figure 4.3.

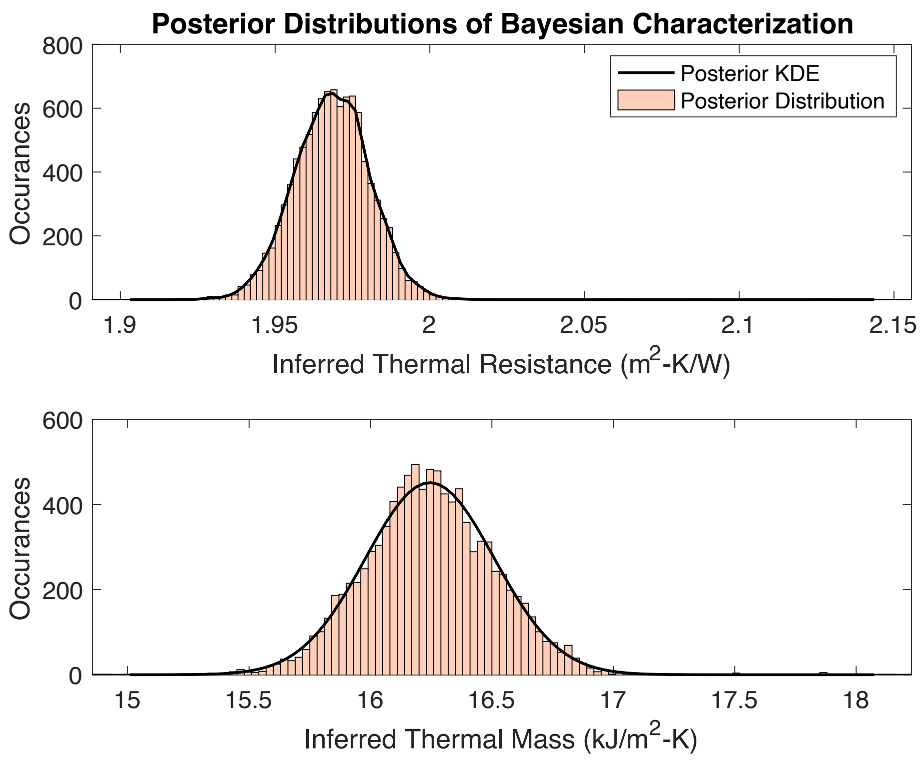

Figure 4.3 Histograms of posterior distributions of the Bayesian inference parameters characterized in the spring low-mass wall (Wall #13) characterization.

From the above figure, prior and posterior distributions for the inference parameters of thermal resistance and thermal mass can be visualized via histograms. Due to the Gaussian prior and likelihood function (native to this DRAM implementation), both generated posterior distributions are Gaussian-like in shape. Due to the intrusion of error in the modeling, these posterior distributions are not exactly Gaussian and are instead represented by a non- Kernel Density Estimation (KDE) plotted as the thick black line. Utilizing this non-parametric fit, confidence intervals can be readily computed for inference posterior. Computation of a confidence interval is extremely important, as it provides a convenient metric to specify certainty bounds in the results of the characterization exercise. The inference posterior values resulting from this Bayesian characterization are 2.14 (2.11, 2.17) m^2-K/W and 18.0 (17.3, 18.7) kJ/m^2-K, with the values in the paratheses representing the lower and upper bounds of the computed non-parametric confidence interval.

Since the implementation of the transient finite element model was the most time-consuming task within this work, the transient thermal characterization was also compared to the Summation Method's steady-state characterization approach. Utilizing the spring simulation present in this subsection, the Summation Method can be applied to evaluate the time-series performance of a traditional R-value test that ignores thermal mass fluctuations. The performance of this steady-state R-value test is shown in Figure 4.4.

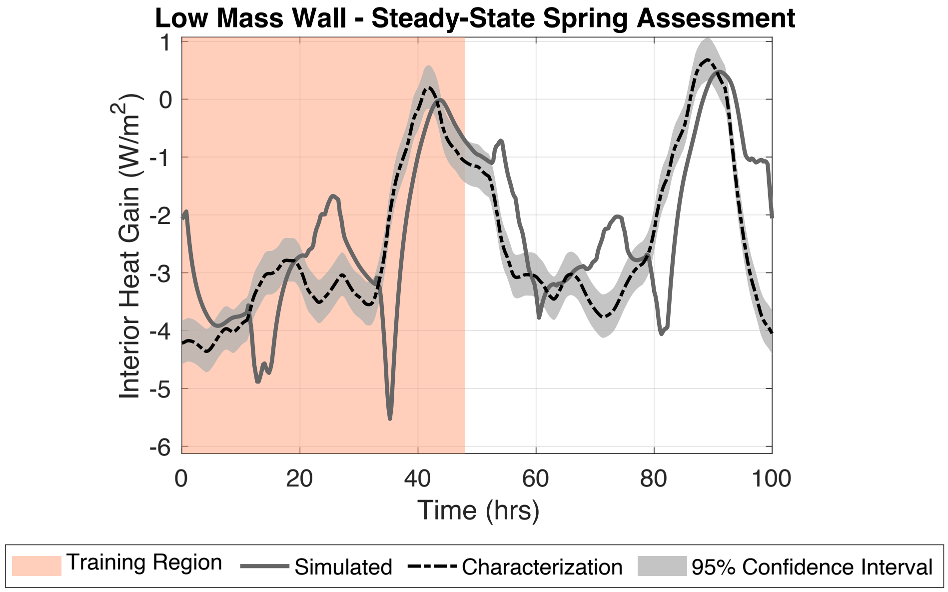

Figure 4.4 Plotted time-series interior heat gain from a traditional steady-state characterization for a low-mass wall (Wall #13) during a spring simulation period.

From Figure 4.4, the plotted interior heat gain of the steady-state thermal characterization can be viewed. These results represent a traditional ASTM C1155 steady-state R-value test, which neglects thermal mass under the assumption that thermal mass's effects are periodic. Due to this assumption, an approximate three-hour lag can be seen between the simulated steady-state interior heat gain and the reference, measured heat gain. Along with the phase difference in both signals, the steady-state characterization overpredicts the effect of the peaks of the heat gain signal. In the real assembly, these peak magnitudes are most likely buffered by the assembly's thermal mass. Despite the phase and magnitude discrepancies of the signals, the steady-state characterization generally displays the trend of the reference data but does not perform as well as the fully transient thermal characterization. A summary of results for the low-mass assembly characterization is summarized in Table 4.2.

Table 4.2 Tabulated transient thermal characterization results for a low-mass wall (Wall #13).

Test Case	Thermal Resistance (R), m^2-K/W	Lumped Thermal Capacitance (C_{th}), kJ/m^2-K	Ref/Model RMSE, W/m^2	Ref/Model NRMSE, %
Simulated Assembly (Wall #13)	2.13	16.8	N/A	N/A
Transient Characterization	2.14 (2.11, 2.17)	18.0 (17.3, 18.7)	0.308 (0.136, 0.688)	6.79% (3.00%, 15.2%)
Steady-State Characterization	1.93 (1.83, 2.02)	N/A	1.24 (1.19, 1.29)	27.3% (26.2%, 28.4%)

From Table 4.2, the results of the characterization exercise for the low-mass wall can be seen. The transient single-layer wall characterized has a similar thermal resistance to the reference wall, with a percentage difference of less than 1% for the mean inferred thermal resistance. This relative size of this percentage error and similarity of results suggest that the wall's insulating value was properly characterized through this procedure. The 95% confidence interval also provides values near the mean and "actual" thermal resistance values, indicating high model confidence in the results.

4.2.2 High Mass Wall Thermal Characterization

The second trial run was run for Wall #63 utilizing 48 hours of heat flux measurements taken at 10-minute intervals and the same spatial and environmental conditions as the low mass wall characterization exercise. The results of this study are presented below.

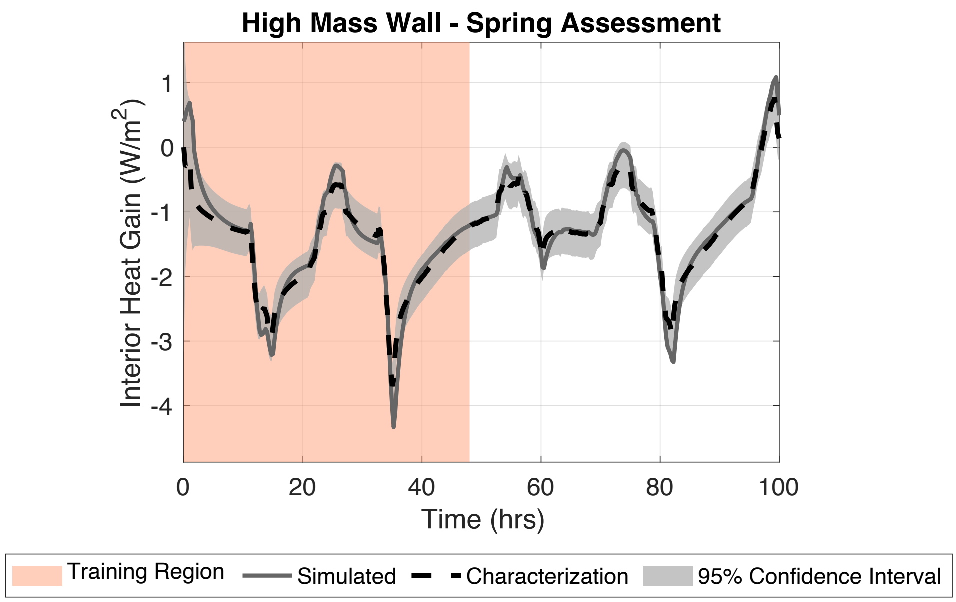

Figure 4.5 Plotted interior heat gain from a Bayesian characterization for a high mass wall (Wall #63) with 48 hours of training data.

In the above figure, the performance of the transient Bayesian characterization routine is displayed. The exercise characterized the high mass wall for a sample simulation in spring, where exterior conditions are similar to that of typical indoor conditions. Due to this small temperature difference, the measured and simulated interior heat flux values are quite small, which accentuates the assumed measurement uncertainties. Despite the large uncertainty bound, the Bayesian characterization routine characterized the reference data high certainty, producing RMSE values of 0.229 (0.149, 0.435) W/m^2 and NRMSE values of 5.19% (3.38%, 9.87%). Due to this low RMSE and a visual inspection of the assembly's time-series performance, this appears to be a successful characterization of an insulated, high-mass wall assembly.

Along with RMSE values and visual inspections of the characterization performance, certainty in inference parameters can also be examined to determine the performance of the characterization. Histograms of the prior and posterior distributions produced by this Bayesian characterization exercise can be visualized in Figure 4.6.

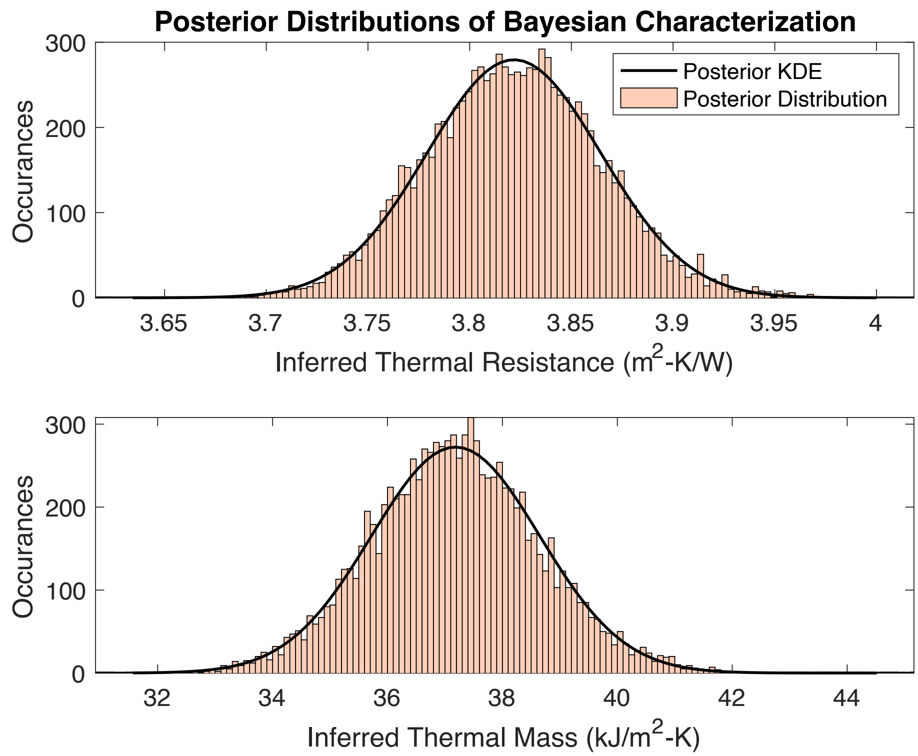

Figure 4.6 Histograms of prior and posterior distributions of the Bayesian inference parameters characterized in the spring high-mass wall (Wall #63) characterization.

From the above figure, prior and posterior distributions for the inference parameters of thermal resistance and thermal mass can be visualized via histograms. As with the previous characterization, the posterior distributions are Gaussian in shape due to their Gaussian prior and likelihood functions. Utilizing the non-parametric fit, confidence intervals were for both parameter posterior distributions. inference posterior values resulting from this Bayesian characterization are 3.82 (3.74, 3.91) m^2-K/W and 37.2 (34.3, 40.1) kJ/m^2-K. Confidence interval bounds on both inference parameters are quite narrow, providing much certainty regarding the thermal resistance and thermal mass inferred via Markov Chains.

Alongside the results of the transient characterization, a steady-state characterization was also performed for the high-mass assembly. The results of the steady-state R-value characterization are displayed in Figure 4.7.

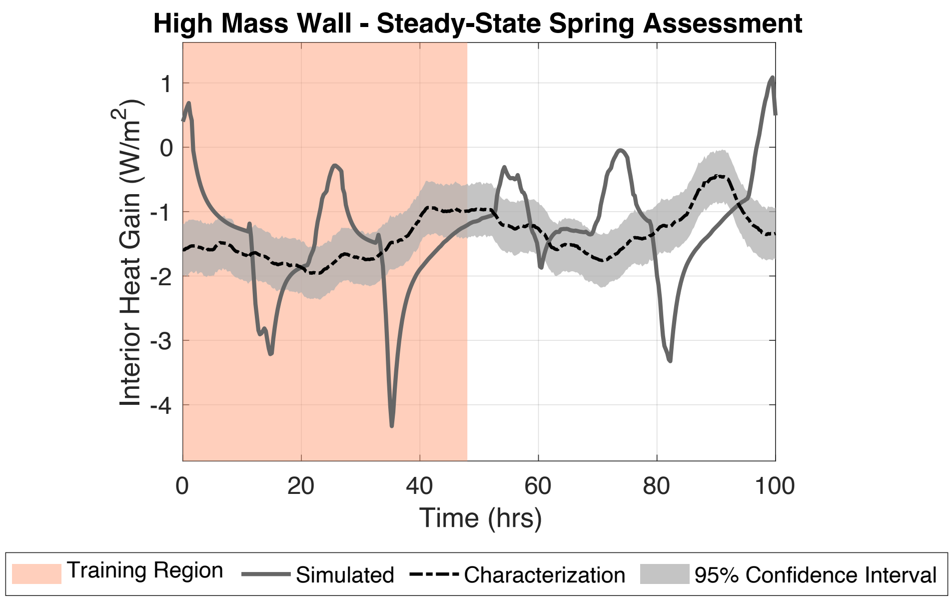

Figure 4.7 Plotted time-series interior heat gain from a steady-state summation method characterization for a high-mass wall assembly (Wall #63).

From Figure 4.7, the plotted interior heat gain of the steady-state thermal characterization can be viewed. As with the low-mass steady-state characterization, this characterization represents an ASTM C1155 summation method characterization, which neglects thermal mass under the assumption that thermal mass's effects are periodic. It should be noted that ASTM C1155 does not endorse the application of the Summation Method to high-mass assemblies such as this one. The standard states: "Examples of the heaviest construction [to which this practice applies to] include: a 390-kg/m^2 wall with a brick veneer, a layer of insulation, and concrete blocks on the inside layer of a 76-mm (3-in.) concrete slab with insulated built-up roofing of 240 kg/m. Insufficient knowledge and experience exists to extend the practice to heavier construction." (ASTM, 2013b). Regardless, the Summation Method displayed in Eq. 1 was applied under the assumption that an inspector may not know the construction of the assembly without destructive testing. It is still important to understand the performance of steady-state characterization, even if the practice is not suggested by ASTM.

Due to the high mass of the candidate assembly, ASTM C1155 does not suggest steady-state characterization to high-mass assemblies, and the results displayed in Figure 4.7 further reinforce this warning. The results of the high-mass wall steady-state characterization do not remotely follow the trend, shape, or magnitude of the reference signal. This discrepancy is a result of the neglected thermal capacitance, or thermal mass, term which is completely ignored in steady-state characterization. One redeeming factor of this characterization is the ability to measure thermal resistance, which was measured at 3.58 (3.58, 3.59) m^2-K/W. This thermal resistance closely mirrors that of the transient characterization, providing confidence in the steady-state approach's ability to characterize thermal resistance. A summary of results for both high-mass assembly characterization is summarized in Table 4.3.

Table 4.3 Tabulated transient thermal characterization results for a high-mass wall.

Test Case	Thermal Resistance (R), m^2-K/W	Lumped Thermal Capacitance (C_{th}), kJ/m^2-K	Ref/Model RMSE, W/m^2	Ref/Model NRMSE, %
Simulated Assembly (Wall #63)	3.78	427	N/A	N/A
Transient Characterization	3.82 (3.74, 3.91)	37.2 (34.3, 40.1)	0.229 (0.149, 0.435)	5.19% (3.38%, 9.87%)
Steady-State Characterization	3.58 (3.58, 3.59)	N/A	0.938 (0.91, 0.965)	21.3% (20.6%, 21.9%)

From Table 4.3, the results of the characterization exercise for the low-mass wall can be seen. The transient single-layer wall characterized has a similar thermal resistance to the reference wall, with a percentage difference of less than 1% for the mean inferred thermal resistance. This relative size of this percentage error and similarity of results suggest that the wall's insulating value was properly characterized through this procedure. The 95% confidence interval also provides values near the mean and "actual" thermal resistance values, indicating high model confidence in the results.

4.3 Exploring Characterization Time Requirements

In preliminary testing, the assessment length, or length of the training dataset, was found to be a limiting factor for characterization performance. In an ideal scenario, training data would be measured for as long as possible, i.e. 7+ days to allow for a sufficient training set. ASTM C1046 states, "[Characterization] requires obtaining data over long periods, perhaps several days, depending on the type of building component and on temperature changes." (ASTM, 2013a), but does not specify the length of assessment required. To further understand the length of assessment required to properly characterize an assembly, each assembly was simulated to find the length of training time required. Walls #1–66 from ASHRAE Fundamentals were simulated in EnergyPlus and characterized for an assessment starting from the first day of April for a DOE/IECC medium office reference building located in Atlanta, Georgia (Deru et al., 2011). Reference building models were simulated with the Hartsfield-Jackson Atlanta TMY3 EnergyPlus weather file (DOE, 2021b). Prior distributions were generated via the methodology described in Section 4.1.2. Walls were characterized with training sets ranging in length from 1 hour up to 96 hours, with each characterization recording the mean RMSE value computed for a validation dataset of 8 days. Mean RMSE values less than 1.00 W/m^2 were deemed to be an "appropriate characterization", providing a metric to determine the minimum training time required for a diverse set of envelope assemblies.

In addition to characterizing the length of time required to appropriately characterize typical envelope assemblies, this exercise also provides a convenient venue to generate a prior distribution database to accompany ASHRAE's wall database present in ASHRAE Fundamentals Chapter 18 (ASHRAE, 2013). The resultant posterior distributions of each assembly characterization can be aggregated into a database, allowing for a straightforward selection of prior distributions for future studies.

4.4 Evaluating Training Dataset Length Requirements

Per the exercise described in Section 4.3, an experiment was run to understand the length of time a façade element must be instrumented for proper characterization. This test simulated all 66 ASHRAE fundamentals wall assemblies with varying lengths of training data. All assemblies were characterized on the south-facing façade of the EnergyPlus medium office model simulated for an Atlanta TMY3 file. Walls were characterized for measured datasets ranging in length from 1 to 96 hours, and the minimum training set length required to achieve a characterization RMSE value of less than 1.00 W/m^2 for each wall. The result of this experimental study is shown below in Figure 4.8.

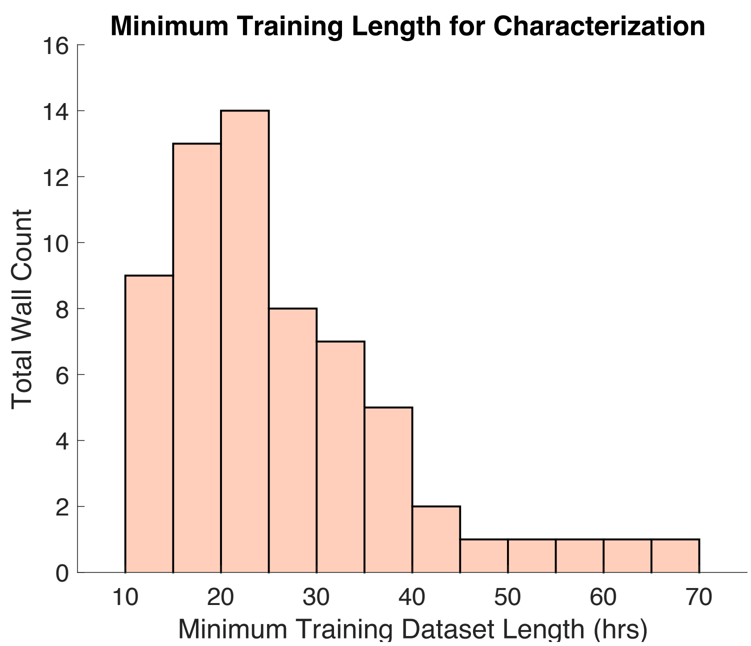

Figure 4.8 A histogram visualizing the training length required to achieve an appropriate wall characterization.

From the above figure, the time required to appropriately characterize a façade element can be visualized. For the 66 ASHRAE fundamentals walls simulated, the results varied depending on the wall's construction type and thermal properties, as suggested in ASTM C1046. This leads to a distribution of required training lengths, each specific to a wall's type and construction.

When viewing the data as a histogram, the plot takes the shape of a positive-skewed distribution, with a mean of 25.5 hours and a standard deviation of 12.5 hours. This histogram's shape is most likely a result of the dataset's entries—e.g. a majority of walls within the dataset were low-to-medium mass wall constructions and a small "tail" of constructions tended towards higher thermal mass. This conclusion is also validated via a qualitative view of the dataset.

Another important piece of information regarding this dataset must be addressed before further analysis can be conducted. From a fundamental standpoint, this ASHRAE wall dataset is a sample of a larger population and therefore should not be interpreted as a population. Each assembly in this dataset represents a single assembly type and is not representative of that assembly's number of occurrences in the US or global existing building stock. Despite this drawback, this dataset can be utilized to approximate the amount of training data required to characterize most assembly types. To identify this time requirement, the 95th percentile was computed from this data to evaluate the amount of time series training data required to characterize most assemblies. From testing, it was noted that the 95th percentile would provide context for the data requirements for most assemblies, except for less common assemblies with excessive thermal mass, e.g. tilt-up concrete constructions. The 95th percentile for the dataset displayed in Figure 4.8 was computed to be 48.1 hours, which is rounded down to 48 hours for practical purposes. This means that 48 hours of measurement data is sufficient to characterize the majority of the ASHRAE fundamentals walls.

4.5 Discussion

This study shows the promise of characterizing façades utilizing transient finite element heat transfer. The results for both transient thermal characterizations displayed strong model agreement with reference datasets and low RMSE values. Transient NRMSE values for transient characterizations of Walls #13 and #63 were computed at 6.79% (3.00%, 15.2%) and 5.19% (3.38%, 9.87%) , respectively. These mean NRMSE are both near below 10% NRMSE from the reference data, indicating strong characterization performance. Additionally, inferred thermal resistances were near that of the simulated assemblies, with percent errors of 7.51% and 1.06% for Wall #13 and Wall #63, compared against their reference simulated assemblies. Error bounds for inferred thermal resistances were also quite narrow, with Wall #13 having an inferred thermal resistance of 2.14 ± 1.40% m^2-K/W and Wall #63 having a value of 3.82 ± 2.23% m^2-K/W. These narrow tolerance bounds indicate high certainty levels of inferred thermal resistance, providing additional information about the characterization’s reliability compared to a single, deterministic value.

While all simulated transient models had good agreement with measured data and thermal resistance was found to be adequately characterized, thermal capacitance was not always found to be near the lumped thermal capacitance value of the real multi-layer wall. The transient thermal characterization trials showed characterized found capacitances with relative differences of 7.14% and 91.3% for the spring characterization of the low-mass assembly and high-mass assembly, respectively. This appears to be an issue with high-mass assemblies, which mimics the discrepancies of summed thermal capacitance and effective thermal capacitance described by Antonopoulos and Koronaki (Antonopoulos & Koronaki, 1998). These results suggest that effective thermal capacitance is not the same as summing the thermal mass of every layer in a multi-layered assembly. Effective thermal capacitance represents the complex interactions between various thermal capacitances and thermal resistances of the multi-layered wall without the need to simulate the complexity of each layer. This result also indirectly shows that the thermal mass of each layer in an assembly cannot be simply added up and modeled as a single layer; a thermally equivalent wall must be found instead when modeling the homogenous analog of a layered assembly.

Another important finding from this study was the relative impact of uncertain film, or convection and radiation, coefficients utilized for the transient characterization. Static film coefficients for both simulation pilots were approximated via the summation method, however, film coefficients are environmentally-dependent and varied over time in the reference simulation. It was also noted that coefficients tended to change drastically during periods of peak heat transfer, which are the regions with the highest discrepancy in Figure 4.2 and Figure 4.5. Due to this, it is suggested that, in real-world experimentation and field deployment, a material with a more static thermal resistance be added at the interior surface, atop the temperature and heat flux sensors. A good candidate for this material is a thin layer of board insulation, which will provide a more static resistive boundary condition that is agnostic of thermal and environmental fluctuations.

In addition to the successful thermal characterizations, another aspect of this research aims to determine the amount of training data required for the characterization of a typical façade element. ASTM C1046 suggests that façade elements be characterized utilizing several days of data depending on the construction, but does not suggest a specific length of instrumentation (ASTM, 2013a). All 66 of the ASHRAE fundamentals assemblies were simulated and characterized, leading to a variety of required training dataset lengths, alongside the generation of a database of prior distributions for each assembly. When plotted in a histogram, this temporal data took the form of a positive skewed normal distribution with a mean of 25.5 hours and a standard deviation of 12.5 hours. When the 95^{th} percentile of this data was computed, it was found that 48.1 hours of data was required to characterize most typical wall constructions. This result puts a specific number to the suggestion proposed in ASTM C1046; slightly more than two days of data is needed to adequately characterize a façade element. It should be noted that this was found via simulation of the ASHRAE fundamentals walls, which are typical non-residential constructions. Non-residential walls tend to employ more massive materials (CMU, cast concrete, heavy insulation) than residential construction, so low-mass residential constructions can most likely be characterized with fewer data. While the minimum requirement of 48.1 hours of measurement data was found, it must be stressed that this is a minimum requirement. Any additional data provides the opportunity to improve the characterization and to have an additional dataset to verify the characterization's performance. Regardless, this minimum required measurement length is practical guidance that more assessment professionals should consider when quantifying envelope performance.

These results of this study motivate the applicability and validity of thermal characterization usage in the built environment. Utilizing surface temperatures and heat flux measurements, any type of opaque façade element can be simulated to understand its performance. While this work was able to characterize the thermal performance of a typical façade element, the hope is that this procedure is used more often in the future to understand the impact of underperforming and unknown façade elements. This methodology was also developed with the aspiration of characterizing defects in a framework that is relevant to assessing their impacts via energy modeling.

4.6 Chapter Conclusion

In conclusion, this chapter proposed and verified a methodology to instrument in-service building envelope assemblies and characterize their performance via Bayesian inference. This procedure uses transient finite elements in a Bayesian inverse modeling workflow to identify thermally equivalent materials representing the complexity of thermal mass and thermal resistance in multi-layer assemblies. This procedure was quite successful when tested, characterizing low and high mass walls with RMSE values below 1 W/m^2. These results also highlighted the shortcomings of steady-state characterization techniques which ignore the effects of thermal mass. This work also put a number to the ASTM C1046 suggestion to "[Obtain] data over long periods, perhaps several days" to characterize a façade element. It was found that collecting data for a little over two days is sufficient to characterize most typical non-residential constructions, giving specific guidance for the instrumentation process of assessment professionals.

The robustness and proven performance of this characterization process provide a vehicle for building professionals and researchers to understand more about how as-built building envelopes perform in the real world. While this work is extremely successful on simulation test cases, the workflow requires field testing for validation in future studies. Applying this method in the real world will also allow for imperfect or moisture-laden assemblies to be characterized and understood, which is a reality whole-building simulation packages like EnergyPlus fail to reproduce.

This study is a fundamental step in the process of detecting, characterizing, and understanding the as-built performance of facades in existing buildings. With the methodology's performance now verified against state-of-the-art energy simulation, field studies can be run to verify the methodology's real-world performance. This represents a strong foundation to begin understanding for in-situ building envelope measurement beyond R-value.

CHAPTER 5: EXPERIMENTAL VALIDATION

In this chapter, an abridged description of the sensors and equipment utilized, equipment calibration, and two physical experiments will be presented. This section aims to experimentally validate the methodology's performance in the field.

5.1 Equipment Selection

Thermal characterization requires the measurement of heat flux and surface temperatures. These metrics can be measured in a variety of ways; however, the selected methods for this application are (1) surface temperature measurements via mounted thermistor and (2) heat flux measurements via a heat flux transducer. Thermistors were selected due to their measurement flexibility (specialized boards and equipment are not required for measurement, unlike thermocouples), and heat flux transducers were selected due to their wide availability and analog nature. Because both sensors produce analog outputs, both sensors can be measured with a standard analog-to-digital converter (ADC). More details on the selected data acquisition (DAQ) platform, ADC, and sensors will be outlined in subsequent sections.

5.1.1 Data Acquisition System

Since it was known that measurement must be taken on both the interior and exterior surfaces of an assembly, there are two options for connecting sensors to the DAQ: (1) one

DAQ with long runs of wire between the DAQ and sensors, sized so that the sensors can travel through doors or windows to reach the opposite side of the assembly, or (2) two DAQs, each on the exterior and interior sides of the building, with relatively short runs of wire between the DAQ and sensors. For practicality, the latter was selected, requiring two data acquisition platforms.

Now that it is known that two DAQs will be utilized for experimentation, more practical concern arose—Will these two DAQs need to be connected to two different computers? How will the DAQs be powered? Will the exterior DAQ and associated computer be able to withstand the outdoor environment? After significant research and background reading, the Arduino platform seemed to address all of these concerns. An Arduino microcontroller is an embedded system that can be operated without the need for an on-site computer connection. Certain Arduino specifications are also designed to be powered via a battery and are compact enough to be housed in a weatherproof enclosure. The Arduino platform also has many open-source libraries and available breakout boards for interfacing with many different types of sensors. Due to all of these benefits, an Arduino MKR Zero was selected as a data acquisition platform. This specific model of Arduino also provides other benefits for data acquisition, such as a built-in microSD input, a built-in 12-bit ADC, LiPo battery inputs, and a low power draw. These features make the Arduino MKR Zero a strong data acquisition system for this application[1]. A photo of the utilized Arduino MKR Zero is displayed in Figure 5.1.

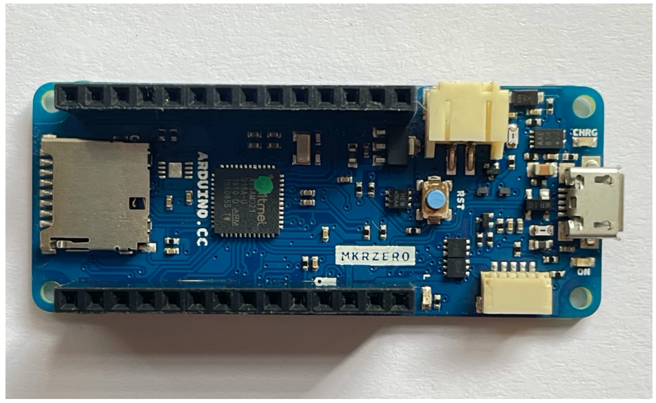

Figure 5.1 An Arduino MKR Zero.

5.1.2 Analog-to-Digital Converter Selection

With the selection of the Arduino MKR Zero, the board has a built-in 12-bit ADC. Due to the Arduino MKR line's operating voltage of 3.3 V, this built-in ADC has an estimated resolution of 1.61 mV. This resolution may be high enough for thermistors, however, most heat flux transducers on the market produce outputs in the 1-10 microvolt range. Because of this, an ADC breakout board was sourced and implemented for sensor measurement. For this application, an external breakout board utilizing a Texas Instruments ADS1115 chip was procured. The ADS1115 is a 16-bit ADC with a programable gain of 16 and a

---

[1] At the time of writing, the Arduino Pro Portenta H7 Lite Connected was released. This microcontroller is designed to be the new Arduino flagship for IoT applications, with many of the same features are the Arduino MKR line. On top of the MKR line's features, this microcontroller also has built-in radio frequency communication; a built-in 16-bit ADC; and a standby current draw in the microamp range, allowing for long lifespans on battery power. If this work were to conducted after the release of the Portenta H7 Lite, this would have been the chosen microcontroller for this application. It should be noted, however, that many of these features of the Portenta H7 Lite were augmented onto an Arduino MKR Zero via external breakout boards.

default sampling rate of 128 SPS. Utilizing the full gain and accounting for noise, the ADS1115 has an effective resolution of 7.81 uV (Texas Instruments, 2019). A sample photo of an ADS1115 breakout board is displayed in Figure 5.2.

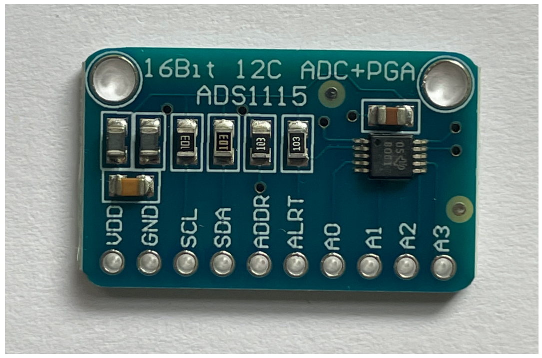

Figure 5.2 An ADS1115 breakout board.

5.1.3 Thermistor Selection

Since these thermistors were required for measuring surface temperatures, priority was given to thermistors that were flat and could be affixed to a surface via adhesive or tape. Thermistors come in a variety of shapes, from probes to surface-mounted thermistors meant for circuit board mounting. For this application, the TEWA TTT6-10KC8-9-25 thin-film negative temperature coefficient (NTC) thermistor was selected. This thermistor is designed for interfacing with flat surfaces and is covered in a Kapton coating to reduce electrical interference and weatherproof the sensor (see Figure 5.3). These sensors have a working temperature range of -30°C to 120°C and have a 10 kOhm resistance at 25°C. Because they are NTC thermistors, these thermistors decrease in resistance as temperatures increase and increase in resistance as temperatures decrease. This phenomenon was measured and calibrated as described in later sections.

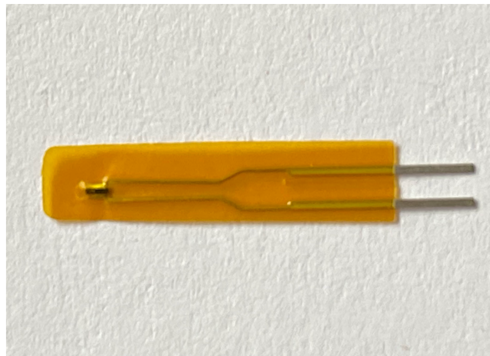

Figure 5.3 A photo of the thin-film thermistor utilized.

5.1.4 Heat Flux Transducer Selection

The final sensor procured was the heat flux sensor. There were many available options for these sensors, however, the selected sensor was a FluxTeq PHFS-09e differential thermopile. This sensor is based on the Seebeck Effect, where the differential thermopile generates a voltage proportional to the heat flux traveling through it. Another advantage of the PHFS-09e is that it is a thin-film heat flux sensor, shielded from moisture and electrical contact via a Kapton film, similar to the selected thermistor. A photo of the heat flux sensor is shown below.

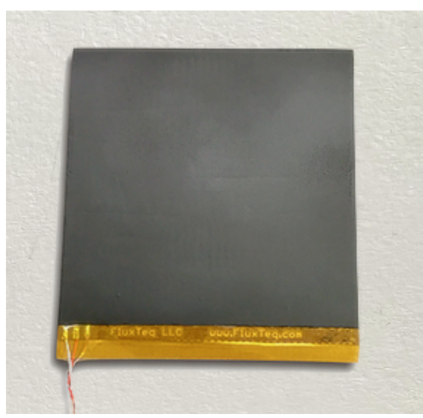

Figure 5.4 A photo of the heat flux sensor utilized.

5.2 Sensor Application and Usage

The goal of this section is to provide context on the mathematical operations required to measure heat fluxes and temperatures via the respective sensors.

5.2.1 Thermistor Usage

Thermistors, by definition, are classified as resistive temperature devices, sometimes referred to as RTDs. RTDs change their resistance under the influence of temperature, allowing for that resistance to be correlated to a temperature value. For a DAQ to measure resistance, the resistor must be placed into a configuration allowing for that resistance to be calculated. There are two popular methods to measure resistance: the voltage divider circuit and the Wheatstone bridge (Ekelof, 2001). The Wheatstone bridge was selected due to its potential to reduce offset and temperature errors, which can often make accurate measurement via voltage divider circuitry difficult. The Wheatstone bridge circuit is displayed below in Figure 5.5.

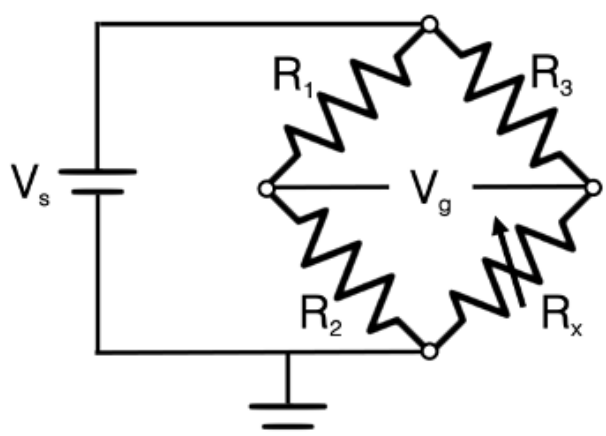

Figure 5.5 A diagram of the Wheatstone bridge circuit.

From the above circuit diagram, a view of a the Wheatstone bridge is displayed. V_s represents the supplied voltage, V_g represented the measured voltage, R_{1-3} represent resistors of fixed voltages, and R_x represents the resistor of unknown resistance, which is a thermistor in this application. Based upon this circuit arrangement, the resistance of the thermistor can be computed via the following equation:

$$R_x = \frac{R_2\, V_s - (R_1 + R_2)\, V_g}{R_1\, V_s + (R_1 + R_2)\, V_g} R_3 \tag{51}$$

From Eq. 51, the unknown resistance can be computed as a function of V_g. R_1, R_2, and R_3 should be known precision resistors. While V_s should be a known excitation voltage, it is recommended that it also be measured at the same time as V_g to guarantee accuracy and completeness of measurement.

With the resistance of the thermistor known, this resistance must be correlated to a temperature value. Resistance-Temperature correlation can be done via the Steinhart–Hart equation (Steinhart & Hart, 1968). This equation is displayed in Eq. 52.

$$T_x = (A + B\, ln(R_x) + C(ln(R_x))^3)^{-1} \tag{52}$$

Where T_x is the temperature of interest; R_x is the thermistor resistance; and A, B, and C are the Steinhart-Hart coefficients which are experimentally determined. These coefficients can be computed via least-squares curve fit.

5.2.2 Heat Flux Sensor Usage

Thermopiles generate voltage under the influence of heat flux due to the Seebeck Effect (FluxTeq, 2020). This voltage can be correlated to a heat flux via an experimentally-determined Seebeck coefficient. From the PHFS-09e sensor manual, the following equation can be found:

$$\dot{q} = (0.00334\ T + 0.917)\, S_c\, V_g \tag{53}$$

From Eq. 53, the equation for converting the heat flux sensor's measured voltage to a heat flux is displayed. In this equation, V_g is the measured voltage produced by the thermopile in V, S_c is the calibration Seebeck coefficient provided via the manufacturer, T is the temperature at the location of the heat flux sensor in °C, and $\dot{q}$ is the measured heat flux in W/m^2-K. It should be noted that FluxTeq does not recommend that these thermopiles be calibrated by the user due to the precise equipment required. Because of this recommendation, the factory calibration values for the heat flux sensors utilized in this research were utilized.

5.3 Sensor Calibration and Uncertainty Quantification

5.3.1 Thermistors

To correlate thermistor resistances to measured temperatures, a laboratory calibration was required. Calibration of the three thermistors took place at the Georgia Tech Manufacturing Related Disciplines Complex. Thermistors were calibrated per ASTM E644, "Standard Test Methods for Testing Industrial Resistance Thermometers" (ASTM, 2019). Testing occurred in an water thermal bath with a Lauda Ecoline E100 circulating thermostat (NIST, n.d.). A photo of the calibration setup is displayed in Figure 5.6.

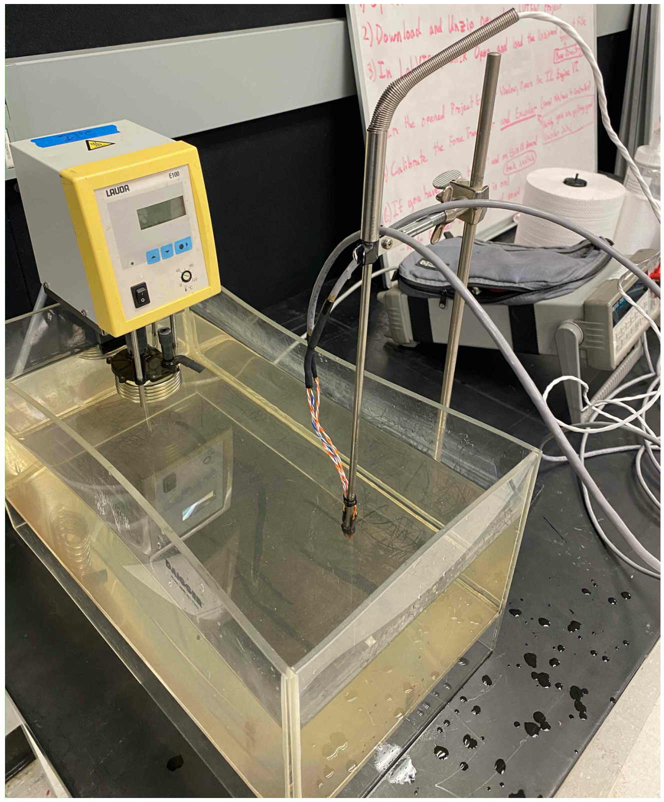

Figure 5.6 A photograph of the thermistor calibration setup.

From the above photo, the thermistor calibration setup is displayed. Water was circuited via the Lauda E100, and thermistor measurements were compared against a calibrated platinum resistance thermometer. This thermometer was reported to have a measurement tolerance of ±0.006°C at 0°C. The reference thermometer was measured via an HP 34401A desktop multimeter, which was reported to have a measurement tolerance of 0.010% for resistance measurements. All three thermistors were calibrated for temperatures ranging between 6.80°C and 69.5°C. The circulating thermostat employed for this calibration unfortunately did not have cooling capabilities, so this set of calibrated thermistors should not be deployed at temperatures below 6.80°C. If deployment in temperatures below 6.80°C is required, these thermistors should be recalibrated with a circulating thermostat with cooling capabilities. This, however, is outside of the scope of this thesis work, and special care was made to avoid deployment in low-temperature scenarios.

Post calibration, the Steinhart–Hart coefficients for each of the calibrated thermistors were computed. Coefficients were computed via MATLAB's nonlinear curve fitting function. A sample calibration curve for Thermistor 1 (which is the thermistor attached to the outdoor-facing side of assemblies) is displayed in Figure 5.7.

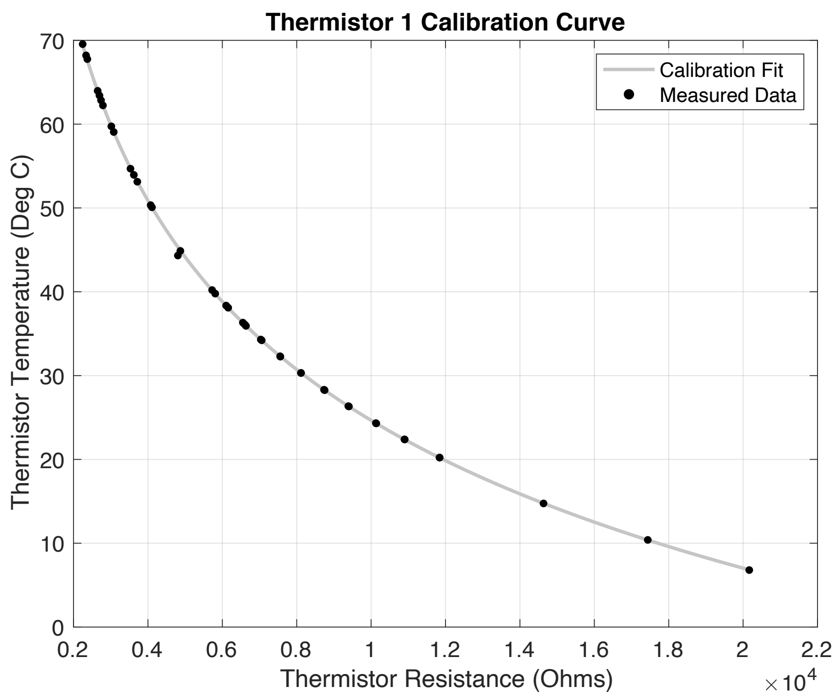

Figure 5.7 A graphical display of a calibrated thermistor curve compared to the calibration data.

In Figure 5.7, the deterministic calibration for Thermistor 1 is displayed. Coefficients for the Steinhart-Hart equation were determined via the non-linear least squares curve fitting toolbox in MATLAB. The graph in Figure 5.7 shows a deterministic calibration; however, this calibration can be approached as a stochastic problem when accounting for uncertainties of other equipment. Possible sources of uncertainty accounted for were: the reference thermometer, the reference thermometer's multimeter, the utilized Arduino and its associated ADC, and resistors utilized in the Wheatstone bridge. Uncertainties can be propagated mathematically with the following formula (Peralta, 2012):

$$s_f = \sqrt{\left(\frac{\partial f}{\partial x}\right)^2 {s_x}^2 + \left(\frac{\partial f}{\partial y}\right)^2 {s_y}^2 + \left(\frac{\partial f}{\partial z}\right)^2 {s_z}^2} \tag{54}$$

From the above equation, the propagation of uncertainties from a function, f, can be calculated. x, y, and z are independent, uncorrelated variables and s represents the standard deviation of each variable. Utilizing this equation with Eq. 52 and Eq. 53 allows for the uncertainty in each temperature sensor to be computed. The sensor calibration coefficients, alongside their computed accuracies are displayed in Table 5.1.

Table 5.1 Tabulated thermistor calibration and uncertainty-related metrics.

Test Case	Mean Steinhart-Hart Coefficient, A	Mean Steinhart-Hart Coefficient, B	Mean Steinhart-Hart Coefficient, C	Calibration-Fit RMSE Value (°C)	Sensor Uncertainty Standard Deviation at 25°C (°C)
Thermistor 1	8.12E-4	2.65E-4	1.38E-7	0.0707	0.190
Thermistor 2	8.35E-4	2.60E-4	1.56E-7	0.0787	0.180
Thermistor 3	8.42E-4	2.59E-4	1.62E-7	0.0782	0.182

5.3.2 Heat Flux Sensors

While the calibration and uncertainty quantification process was an extensive effort for thermistors, the process was much more straightforward for the heat flux sensors. The heat flux transducers procured were calibrated by the manufacturer before their shipment. This means that these sensors need not be recalibrated and could be utilized with the manufacturer-provided Seebeck coefficient and its related uncertainty. The heat flux sensor's uncertainty was propagated using Eq. 53 and Eq. 54. From the calculation, the chosen heat flux sensor, thermistor, and ADC selection result in an uncertainty standard deviation of 0.9758 W/m^2 at 0 W/m^2 and 25°C.

5.4 Experimental Design - Atlanta

To validate the real-world performance of the proposed transient characterization methodology, a physical experiment was designed. The goal of this experiment was to display the performance of the characterization methodology on an in-service assembly. For this experiment, the façade of a 1920s multifamily building in Atlanta was utilized as a test case. A photo of this building is displayed in Figure 5.8.


Figure 5.8 A photograph of the building where experimentation occurred.

From the photo, an overview photo of the building can be seen. This building was a multifamily building built in the 1920s, which housed 18 individual units. Testing occurred on the façade of the first-floor apartment, which is the right half of the building, divided along the downspout near the middle of the photo. Due to the presence of a basement, the first floor is represented by the third window, if counting downwards from the roof.

With this building being from the 1920s, inferences can be made regarding the wall assemblies. Due to this building being built in the early-1900s, it can be anticipated that these walls were constructed of structurally-bonded bricks. Below is a photo of the brickwork, for reference:

Figure 5.9 A photograph of the building's brickwork pattern.

From the above photo, the brickwork can be seen. Based upon the pattern, this assembly appears to be a common bond, where headers bricks are laid with the short side facing outwards and two layers of stretcher bricks are laid side to side. While these walls appear to be one brick length thick (or two brick widths thick), the true number of brick layers is unknown. It was noted by the building owner that the interior walls of this building were uninsulated and comprised of plaster interior finish; however, not much else was known of the walls' composition. All that can be inferred is that this is a mass masonry assembly.

Because of the uncertainties in this wall's composition, there can be significant guesswork related to this wall's thermal performance. This assembly is also interesting from a thermal mass perspective, since it is a mass wall and most likely would not be characterized well with R-value alone. To characterize this wall's performance, sensors were deployed on this assembly. Similar to the sensor layout proposed in Figure 3.5, thermistors were deployed on the interior-facing and exterior-facing surfaces of the assembly, and a heat flux sensor was deployed on the interior-facing surface of the assembly. It was noted that temperature or airflow-related shifts in the interior surface film (convection) coefficient created difficulties for the methodology, so a ½ inch square of expanded polystyrene (EPS) covered the interior surface of the assembly, with a third temperature sensor on the exterior of that EPS covering. A figure display of this sensor layout is displayed in Figure 5.10.

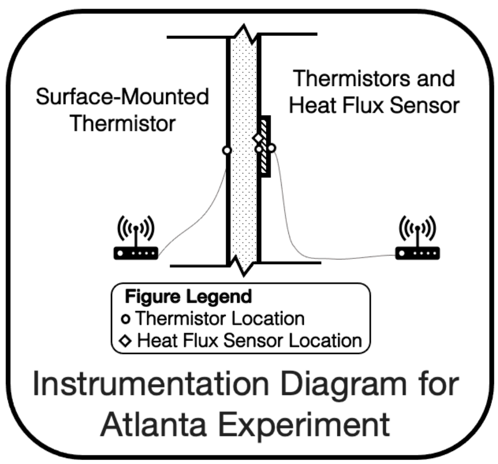

Figure 5.10 A diagram displaying the sensor layout utilized in this experiment.

From the above figure, an overview of the experimental sensor layout is displayed. Photographs of the actual sensor implementation are displayed in Figure 5.11 and Figure 5.12.

Figure 5.11 A photograph of the exterior surface temperature sensor.

Figure 5.12 A photograph of the interior surface sensors and EPS board.

From Figure 5.11 and Figure 5.12, the installed experimental equipment can be seen. Before sensor installation, the interior and exterior surfaces of the assembly were assessed via a thermal camera to identify thermal bridges or other anomalies. No anomalies were identified at this measurement spot, so the position was marked. To align the exterior and interior sensors, a rare earth magnet was attached to the exterior marking via double-sided tape. An analog compass was utilized to identify the corresponding planar position on the interior surface of the assembly. Once both positions were marked, the sensors and EPS board were affixed to the wall via double-sided carpet tape. With the sensors installed, data collection could begin. With the sensors installed, data was collected at 5-minute increments over 5 days. Experimentation occurred between March 28^{th,} 2021 to April 1^{st,} 2021. There was no precipitation during this time, and the building was in service during the entire measurement period.

5.5 Experimental Thermal Characterization - Atlanta

As mentioned in the previous section, a sample envelope section was characterized in an Atlanta multifamily building. The 100 hours of data were measured in 5-minute increments between 3/28/2021–4/1/2021. This data was split into 48 hours of training data and 52 hours of validation data.

For the Bayesian calibration, the DRAM MCMC algorithm was utilized allowed to run for 10,000 function iterations to allow for chain convergence as well as chain mixing. Thermistor measurements were estimated to have a normally distributed uncertainty according to their respective values in Table 5.1. A normally distributed uncertainty of the form N(0, 0.9758) W/m^2 was also applied to all heat flux measurements. For the input prior distribution, a non-informative prior was utilized due to the unknown composition of the assembly. Priors for both This modeling input airs on the side of conservatism, to avoid influencing the Bayesian characterization when the assembly's composition is unknown.

Utilizing all of this information, the transient characterization was conducted. A diagram of the time series results is displayed in Figure 5.13.

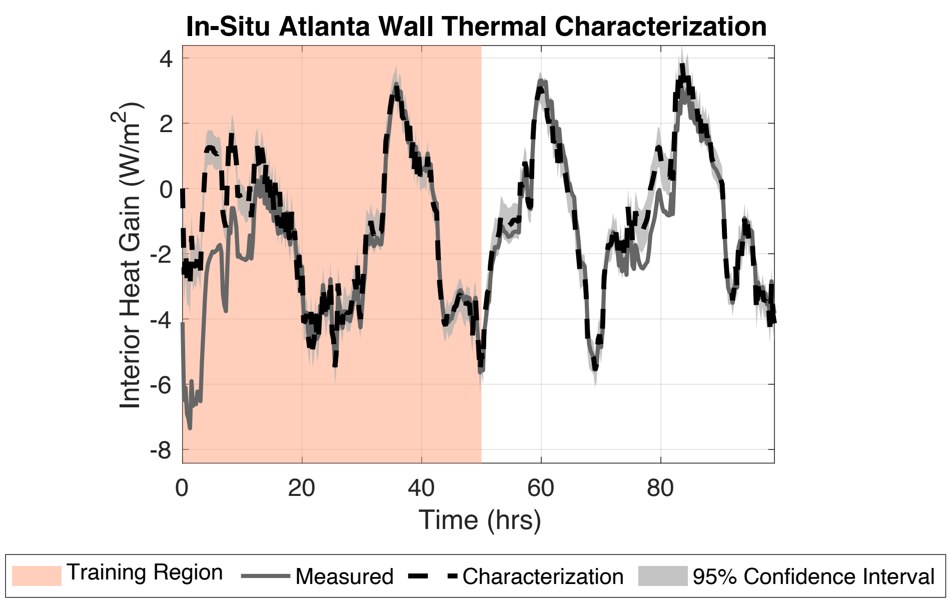

Figure 5.13 Plotted interior heat gain from a Bayesian characterization for the Atlanta characterization experiment.

From the above figure, the performance of the Bayesian characterization is displayed. This characterization was performed utilizing the 48 hours of training data (highlighted in red), then was assessed over 52 hours of validation data. During the training period, it can be noted that the characterization required approximately 20.0 hours of time before it began to capture the impact of the assembly's thermal mass. This is due to the assembly being a mass wall, and the simulation transitioning from its initial conditions during the simulation "warm-up period". After this "warm-up period", the characterization begins to closely match the measured data, with a validation period RMSE value of 0.805 (0.475, 1.30) W/m^2. With these results in consideration, this same equipment can be employed for a steady-state characterization via the Summation Method. The results of this steady-state characterization are displayed in Figure 5.14.

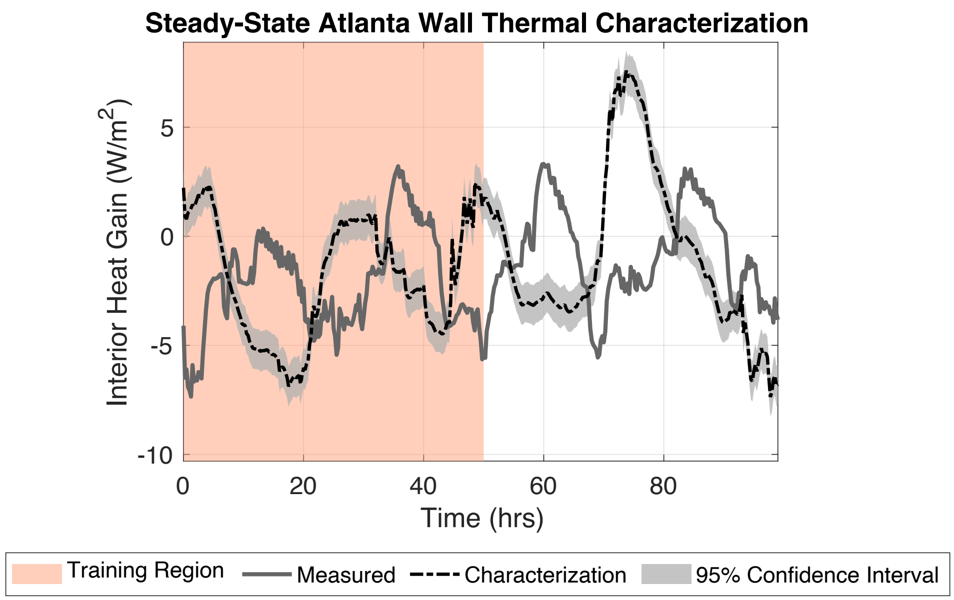

Figure 5.14 A graph of the time series measured interior-surface heat gain compared to the steady-state.

From Figure 5.14, the steady-state characterization is displayed. Viewing this as time-series data, it can be noted that the steady-state characterization vaguely matches the measured data in magnitude, but the peaks and troughs of the measured data tend to lag the steady-state characterization by approximately 11 hours. This is due to the absence of thermal mass in the steady-state characterization. Despite the differences in magnitude and occurrence of the heat flux peaks, this steady-state characterization did capture a thermal resistance value of 0.561 (0.554, 0.569) m^2-K/W, with the mean value within 3% of that measured via the transient characterization. This shows that there is still value in steady-state characterization, however, thermal mass plays a large role in time series performance, especially in (suspected) mass walls.

Alongside the time series portion of characterization, the transient characterization of the assembly's thermal mass and thermal resistance can be viewed. These characterizations can be viewed through histograms and trace plots. The trace plots of the Markov chains' iterations are displayed below in Figure 5.15.

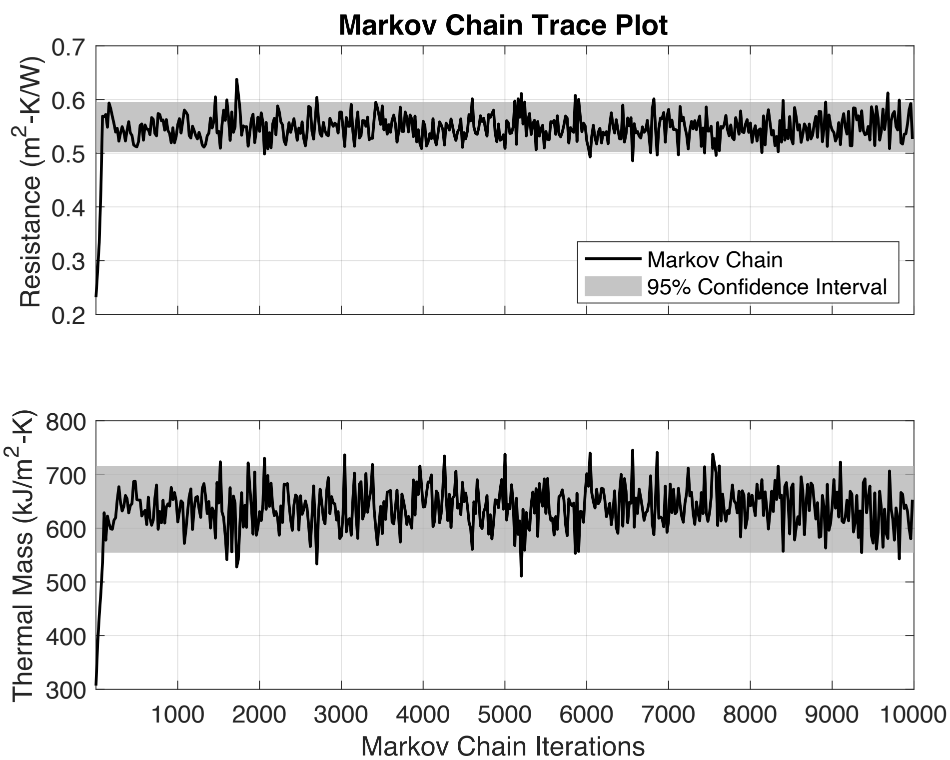

Figure 5.15 The Markov chain trace plot of thermal resistance and thermal mass for the Atlanta wall characterization.

From the above figure, the trace plots for both thermal resistance and thermal mass are displayed. From the trace plots, it can be noted that the Markov chain for thermal resistance appears to have converged to a stationary distribution near iteration number 200, while thermal mass took much longer—approximately 450 samples to converge. Following this convergence, the Markov chains converged to values of 0.546 (0.503, 0.595) m^2-K/W for thermal resistance and 636 (554, 715) kJ/m^2-K for thermal mass. These Markov chains can be viewed in histogram formats in Figure 5.16.

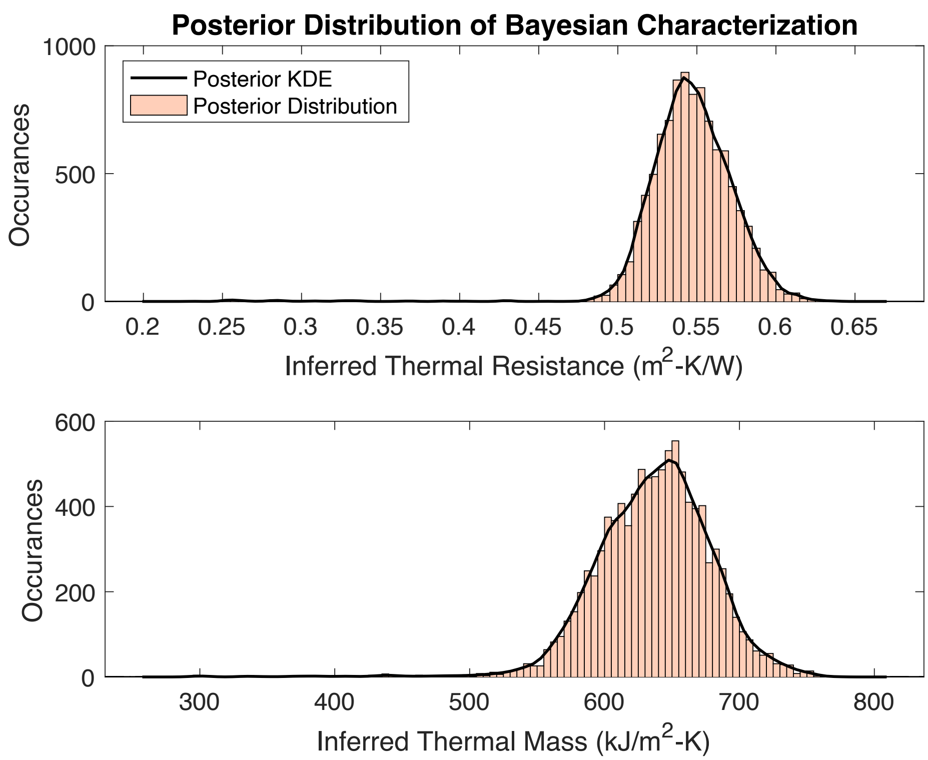

Figure 5.16 Histograms of the posterior distribution of the Bayesian inference parameters characterized in the Atlanta wall characterization.

From Figure 5.16, the distribution of characterized thermal mass and thermal resistance can be visualized via a histogram. The convergence of the Markov chain is apparent via the distributions sampled around 0.546 (0.503, 0.595) m^2-K/W for thermal resistance and 636 (554, 715) kJ/m^2-K for thermal mass, and the starting point (before chain convergence) is visible via the long, low occurrence number tail of the kernel density estimation. Another feature of this characterization is that the measured thermal resistance and thermal capacitance are unlike that of any other wall in the ASHRAE Fundamentals wall database. The wall with the nearest thermal properties is Wall #66, which is single layer of uninsulated 300mm heavyweight concrete. This suggests that this assembly may be a similar uninsulated mass wall.

Each of the values for this wall's in-situ characterization are tabulated within Table 5.2

Table 5.2 Tabulated thermal characterization results for tested Atlanta wall.

Test Case	Thermal Resistance (R), m^2-K/W	Lumped Thermal Capacitance (C_{th}), kJ/m^2-K	Ref/Model RMSE, W/m^2	Ref/Model NRMSE, %
Transient Characterization	0.546 (0.503, 0.595)	636 (554, 715)	0.805 (0.475, 1.30)	8.99% (5.3%, 14.6%)
Steady-State Characterization	0.561 (0.554, 0.569)	N/A	4.69 (4.62, 4.77)	52.4% (51.6%, 53.3%)

5.6 Experimental Design - Cloquet

To further test the proposed methodology, a dataset from the project Wall Upgrades for Deep Residential Energy Renovation (DE-LC-000L048) was utilized. This project was a joint project between Pacific Northwest National Laboratory, Oak Ridge National Laboratory, and the University of Minnesota. Through this project, retrofit wall assemblies were constructed and instrumented at the Cloquet Residential Research Facility (CRRF) located at the University of Minnesota's Cloquet Forestry Center. Constructed walls were instrumented with temperature, moisture, and heat flux sensors and were exposed to outdoor conditions for up to 1.5 years, depending on the wall's project phase. For this application, the south-facing cellulose drill-and-fill wall was selected. Photos of this wall and its construction are displayed in Figure 5.17.

a) The cellulose insulation contractor with the completed drill-&-fill wall before sealing and cladding reinstall.

b) The finalized drill-and-fill wall test panel.

Figure 5.17 Photographs of the cellulose drill-and-fill wall installation at the CRRF. (Photo Credit: Patrick Huelman)

After construction, this wall was monitored for 1.5 years up to the point of writing. This wall remained in service, and data were collected remotely in five-minute increments. Temperature sensors and moisture probes were located throughout the wall and a heat flux sensor was placed on the interior-facing surface. Below is a diagram of this wall's material layering and sensor layout.

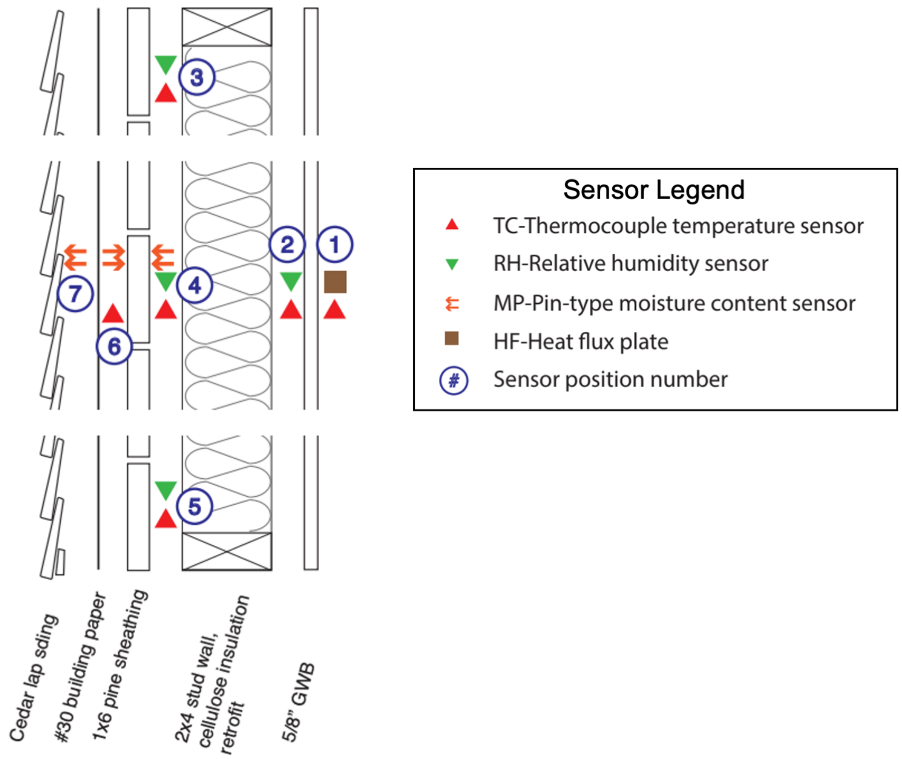

Figure 5.18 A diagram of the drill-and-fill wall assembly composition and sensor layout.

For this experiment, temperature sensors in positions 1 and 6 were utilized, alongside the heat flux sensor at position 1 and another thermocouple measuring indoor ambient air temperatures within the test bay. T-type thermocouples were utilized, therefore an uncertainty of ±1.00°C was assumed (Omega Engineering, n.d.). Similar to the Atlanta experimental study, a FluxTeq PHFS-09e differential thermopile was utilized to measure heat flux. The PHFS-09e was used with a Campbell Scientific CR1000x 24-bit data logger. Propagating datalogger and sensor uncertainty for this sensor results in a heat flux measurement uncertainty of ±0.686 W/m^2 (assuming coverage factor of k=1.96 for a 95% confidence interval).

Utilizing the data from this wall assembly, the transient performance of this assembly could be characterized (excluding the influence of the cedar siding, due to TC-6's location in the assembly). Temperature and heat flux data from midnight January 22, 2021 to midnight January 26, 2021 was utilized for the Bayesian thermal characterization. This characterization was conducted utilizing 10,000 Markov chain iterations with the DRAM and an informative prior. Due this assembly being of known composition, a prior for Wall #11 from the ASHRAE Wall database was utilized. Additional information of the production of this prior can be found in Section 4.3. The results of this characterization are displayed in the subsequent section.

5.7 Experimental Thermal Characterization - Cloquet

As previously stated, thermal data from the Cloquet drill-and-fill wall was utilized for thermal characterization. 48 hours of data from the start 01/22/21 to the end of 1/23/21 was utilized for model training, then the model was evaluated utilizing 48 hours of data from 1/24/21 to 1/25/21. The results of this characterization are displayed below:

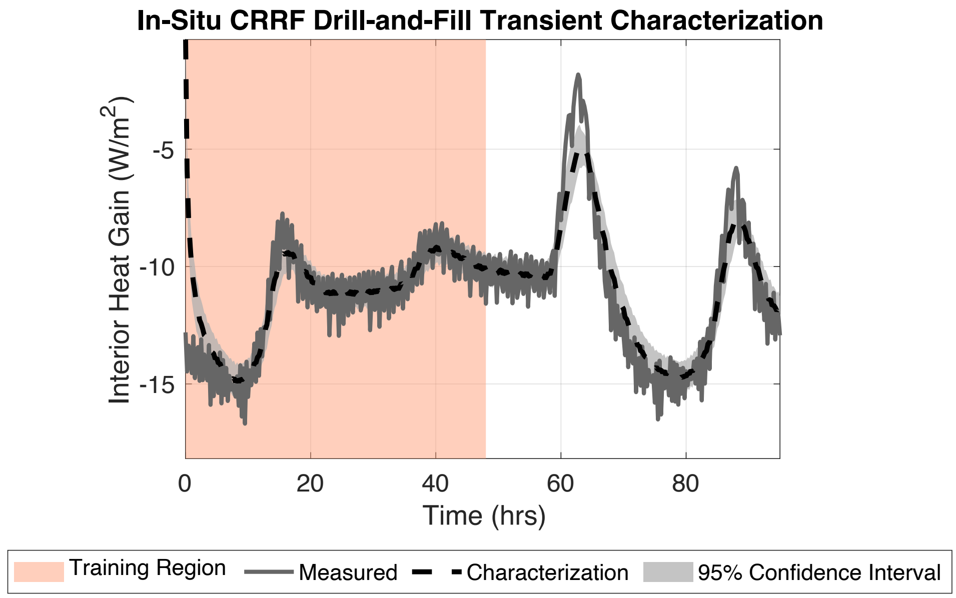

Figure 5.19 Plotted interior heat gain from a Bayesian characterization for the Cloquet drill-and-fill characterization experiment.

From the above figure, the transient characterization for the drill-and-fill wall is displayed. It can be noted that the measurement data does appear to have consistent noise across the entire measurement period. This noise is attributed to the on-off switching of the bay's resistance heater, which was set to maintain a setpoint of 22.2°C. Regardless of this noise, the characterization did fit the trend of the measured data, producing a measured-characterization RMSE value of 1.34 (1.23, 1.45) W/m^2.

Viewing the wall's characterization, a few things can be noted in Figure 5.19. First off, the warm-up period is present but ends near the 4-hour mark, indicating this is an assembly with a lower thermal mass than that evaluated in the Atlanta experiment. Additionally, this characterization does have issues matching the peaks and troughs of the measured heat flux. This phenomenon is due to the free-floating film coefficient present on the interior surface of the assembly, which was computed to be approx. 4.79 W/m^2-K via the

Summation Method. The Atlanta experiment utilized a piece of board insulation to act as a stable resistive boundary condition, compared to the temperature- and environmental-dependent film coefficient utilized here. Regardless, the computation and application of an average film coefficient allows for an assembly to be characterized, however, the characterization may underpredict the peaks and troughs of the time-dependent heat transfer due to film coefficient averaging.

Alongside the time-dependent heat flux, thermal masses and thermal resistances were inferred at each step of the 10,000 Markov chain iterations. Trace plots for the parameter estimations are displayed in Figure 5.20.

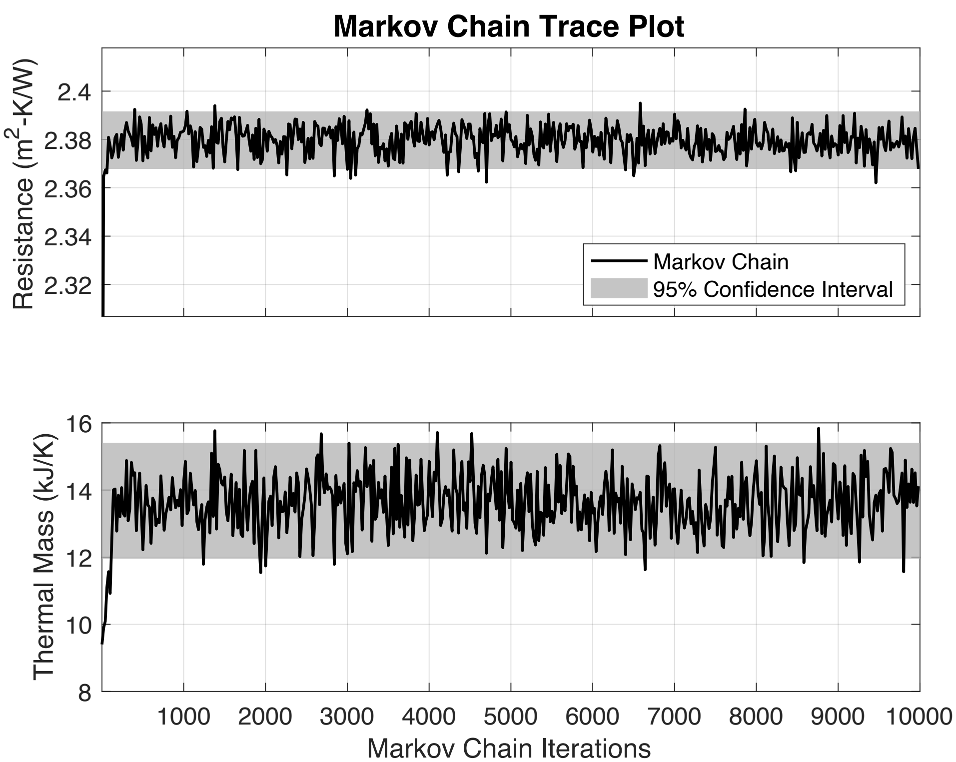

Figure 5.20 Trace plots of the Bayesian inference parameter Markov chains in the CRRF Drill-and-Fill characterization.

From Figure 5.20, the convergence of the Markov chains can be seen. Chains for thermal resistance appear to begin converging near iteration #50, and chains for thermal mass converge near iteration #150, which is much faster than that for the Atlanta experiment. This thermal resistance and thermal mass converged to values of 2.38 (2.37, 2.39) m^2-K/W and 13.7 (12.0, 15.4) kJ/m^2-K, respectively. The histogram of characterized thermal resistances and thermal masses can be visualized in Figure 5.21.

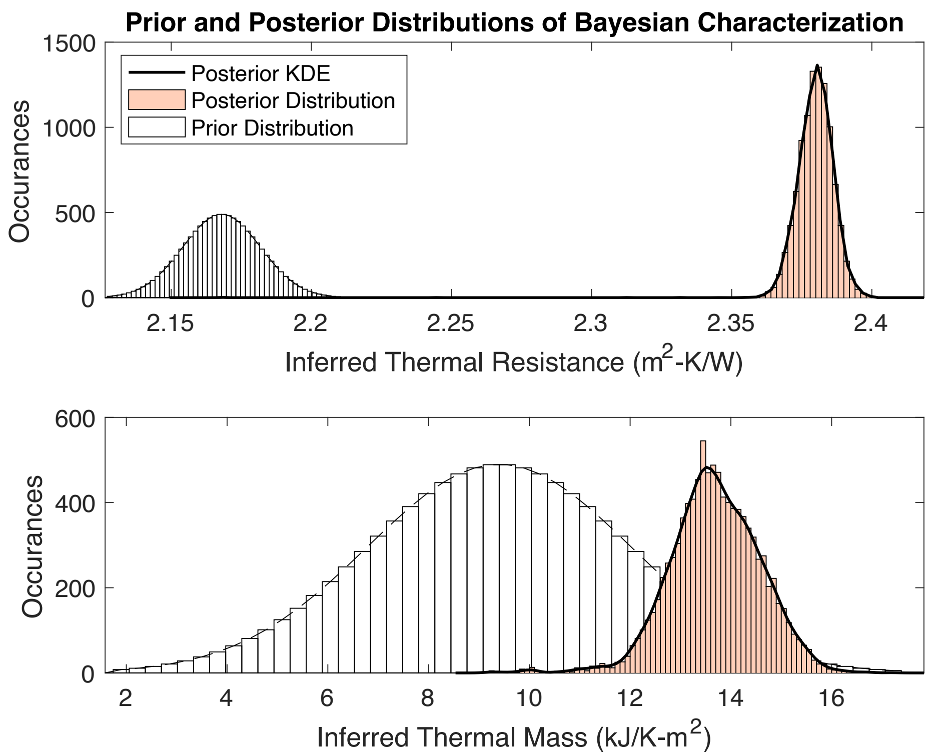

Figure 5.21 Histograms of prior and posterior distributions of the Bayesian inference parameters characterized in the CRRF Drill-and-Fill wall characterization.

From Figure 5.21, the histograms of the inferred thermal mass and thermal resistance values are displayed. Based upon the shape of the histograms, it can be inferred that the prior and posterior thermal mass values are similar in shape and mean value. Alternatively, thermal resistance values started at a mean value of 2.17 m^2-K/W, with the Markov chains converging near a value of 2.38 (2.37, 2.39) m^2-K/W. This is due to minor differences in composition between the idealized prior distribution, Wall #11 in this case, and the real composition of the in-service assembly.

Alongside the transient characterization, there is also value in comparing these results to the steady-state characterization. Utilizing the summation method, the steady-state R-value was computed to be 2.33 (2.32, 2.34) m^2-K/W. With this R-value, the steady-state characterization's interior-facing heat flux was computed. This plot is displayed in

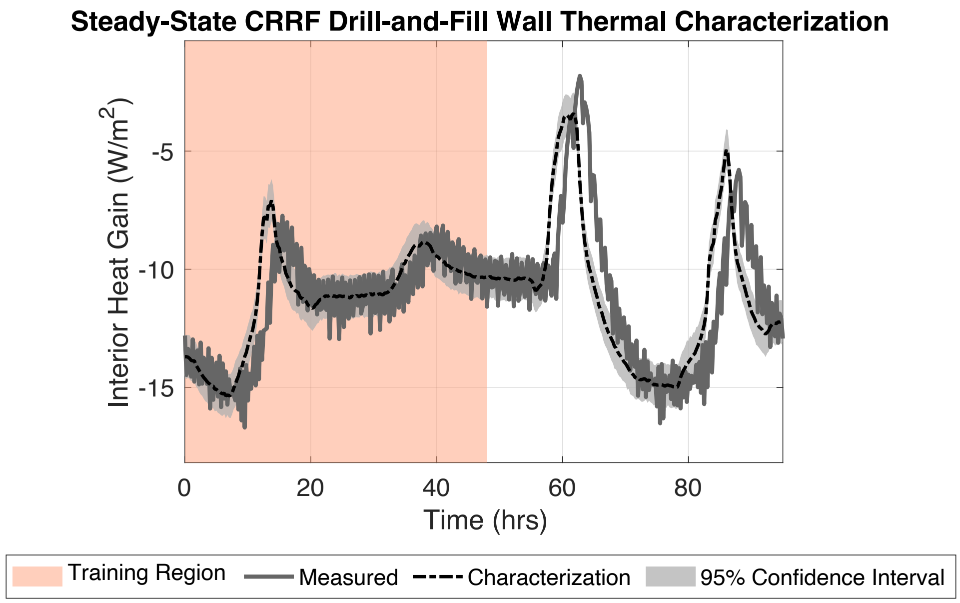

Figure 5.22 A graph of the time series measured interior-surface heat gain compared to the steady-state for the CRRF Drill-and-Fill assembly.

From the above figure, the steady-state characterization for this assembly can be evaluated. Due to the absence of thermal mass, this characterization does lag behind the measured data by approximately 2 hours. Based upon all of the other assemblies characterized, this period of thermal lag is to be expected for a stud-wall assembly. Outside of the steady-state characterization's phase shift, the steady-state characterization matches the trend of the measured data while overpredicting some peak heat flux values and underpredicting others. This is due to the absence of thermal mass; however, this characterization is quite strong otherwise.

Summarizing both of the characterizations, the following table can be generated:

Table 5.3 Tabulated thermal characterization results for tested CRRF Drill-and-Fill wall.

Test Case	Thermal Resistance (R), m^2-K/W	Lumped Thermal Capacitance (C_{th}), kJ/m^2-K	Ref/Model RMSE, W/m^2	Ref/Model NRMSE, %
"Similar" Assembly (Wall #11)	2.17	9.40	N/A	N/A
Transient Characterization	2.38 (2.37, 2.39)	13.7 (12, 15.4)	1.34 (1.23, 1.45)	9.12% (8.34%, 9.90%)
Steady-State Characterization	2.33 (2.32, 2.34)	N/A	2.38 (2.32, 2.45)	16.2% (15.7%, 16.6%)

5.8 Chapter Conclusion

In conclusion, the real-world performance of the transient characterization approach was validated in this chapter. This chapter displayed an experimental case study on a real in-service assembly; motivated the equipment selection, usage, calibration, and uncertainty quantification; addressed modeler inferences when testing an assembly of unknown composition; and validated the usage of a Bayesian inference approach to characterize transient thermal performance. The equipment displayed in this chapter was selected, procured, and deployed to validate this research. This equipment was funded via the Georgia Tech-Oak Ridge National Laboratory Collaboration seed grant, which made this experiment possible. This experiment was also made possible via the Georgia Tech College of Engineering, which granted access to calibration equipment to calibrate temperature sensors. Post-calibration, the uncertainty of all equipment was quantified, and equipment was deployed on a 1920s multifamily building in Atlanta. The composition of this building was inferred to possibly be a brick mass wall with minimal insulation, which was supported by experimental data. Data was collected for 100 hours, and the transient performance of this assembly was characterized via Bayesian inference. The thermal mass and thermal resistance of this assembly were measured to be 636 (554, 715) kJ/m^2-K and 0.546 (0.503, 0.595) m^2-K/W, respectively. These values are unlike any assembly present in the ASHRAE wall database, which suggests that there may be a deficiency in the database's entries related to existing, insulation-deficient assemblies.

To further validate this methodology, a low-mass, insulated assembly was characterized in Cloquet, Minnesota. This assembly was characterized in late January 2021in the depths of the Minnesota winter. This drill-and-fill assembly was built as an in-service test panel at the University of Minnesota Cloquet Residential Research Facility (CRRF) in collaboration with Pacific Northwest National Laboratory and Oak Ridge National Laboratory. Utilizing this sensor data, this assembly was characterized with an RMSE value of 2.38 (2.32, 2.45) W/m^2 during the 48-hour validation period. Thermal resistance and thermal mass were characterized to be 2.38 (2.37, 2.39) m^2-K/W and 13.7 (12.0, 15.4) kJ/m^2-K, respectively. These inferred thermal properties are near the expectation for the assembly, which was thought to be similar to ASHRAE Wall #11 in thermal performance.

While this chapter focused primarily on the technical aspects of these findings, there is a significant impact associated with this experimental work. These experiments confirm the validity of transient thermal characterization, allowing for confidence in utilizing this methodology in a variety of field applications under the influence of diverse weather conditions. Whether this is applied to a low mass or a high mass assembly in a hot or cold climate, this methodology displayed the potential to characterize transient thermal performance. This methodology performs under uncertainty with real sensor data, allowing for thermal mass to be captured alongside thermal resistance in R-value testing to gather a better understanding of as-built assembly performance.

5.9 Chapter Acknowledgement

The experimentation which occurred in Atlanta within this chapter was funded by the Georgia Tech-Oak Ridge National Laboratory Collaboration seed grant. This grant was awarded in Summer 2020 to be utilized for equipment procurement, equipment deployment, and experimentation at Oak Ridge National Laboratory. Experimentation at Oak Ridge National Laboratory did not occur due to COVID-19 travel restrictions; however, the monetary support provided by this seed grant made part of this chapter possible.

A special thanks also goes out to Pacific Northwest National Laboratory for sharing experimental data from the Cloquet Residential Research Facility test wall.

CHAPTER 6: PREDICTING ASSEMBLY CONSTRUCTION FROM IN-SITU CHARACTERIZATION RESULTS

With 50% of the aging US building stock constructed before 1980 (IEA, 2019), there are a significant number of buildings requiring energy retrofits in the coming future. Throughout this dissertation, transient thermal characterization has been posed as a solution to better understand in-situ envelope performance. This methodology, based upon that of ASTM C1155, has been proposed, verified, and validated in previous chapters; however, thermal characterization does fall short of providing information related to the assembly's materiality. While thermal characterization does have applicability to generate model inputs for thermal modeling, Building Energy Modeling (BEM), or retrofit decision making, this testing data can serve another purpose—classification. Machine Learning (ML) classification algorithms, such as K-nearest neighbors (KNN) (Altman, 1992), random forests (Breiman, 2001), and neural networks (Wan, 1990), can be utilized to correlate parameters to classes, which can be adapted for application in building envelopes. Research utilizing ML classification algorithms in the building sector is becoming more popular in the building industry; however, the bulk of these applications are mostly relegated to computer vision and geometry reconstruction applications (K. Chen, Reichard, Akanmu, et al., 2021; K. Chen, Reichard, Xu, et al., 2021; Deeb & LeWinter, 2018; Park & Guldmann, 2019; Rakha et al., 2018). While geometry reconstruction and feature recognition do provide context to a building's structure, these advances are limited when predicting the detailed composition inside of an envelope assembly.

Presently, there are a few methods to gather information on an envelope assembly—(1) destructive testing (Jasiński et al., 2019; Liñán et al., 2015), (2) thermography (Barreira & de Freitas, 2007; Garrido et al., 2022; Taylor et al., 2014), and (3) ultrasound or penetrating radar techniques (Dhekne et al., 2018; El Masri & Rakha, 2020; Liñán et al., 2015; Protiva et al., 2011; Sévigny & Fournier, 2017). The non-destructive methods of infrared thermography and radar-based techniques display promise of identifying wall structure (e.g. stud patterns and structural members can be identified); however, these techniques provide no context on the layering of individual materials or thermal performance of the assembly. Currently, the only method to identify materiality of assemblies is via destructive testing, such as sample drilling or borescope drilling. The major downside of this approach is its destructive nature, where testing requires damaging the assembly. Each of these modern testing techniques can provide some form of context on an assembly or structure, but at that time of writing this paper, no modern in-situ testing techniques can provide material layering detailing for an envelope assembly. ML can be utilized alongside in-situ thermal testing to infer assembly make-up. Measured thermal resistance values, along with effective assembly thermal capacitance values measured from transient thermal characterization, can be leveraged alongside ML techniques to infer assembly make-up. The details of this procedure will be described in subsequent sections.

6.1 Classification Framework

This chapter proposes a proof-of-concept methodology to infer the materiality of a building envelope assembly from in-situ testing data. This framework utilizes effective thermal metrics computed via in-situ envelope characterization to classify an assembly's materiality. Figure 6.1 showcases the proposed methodology's framework below.

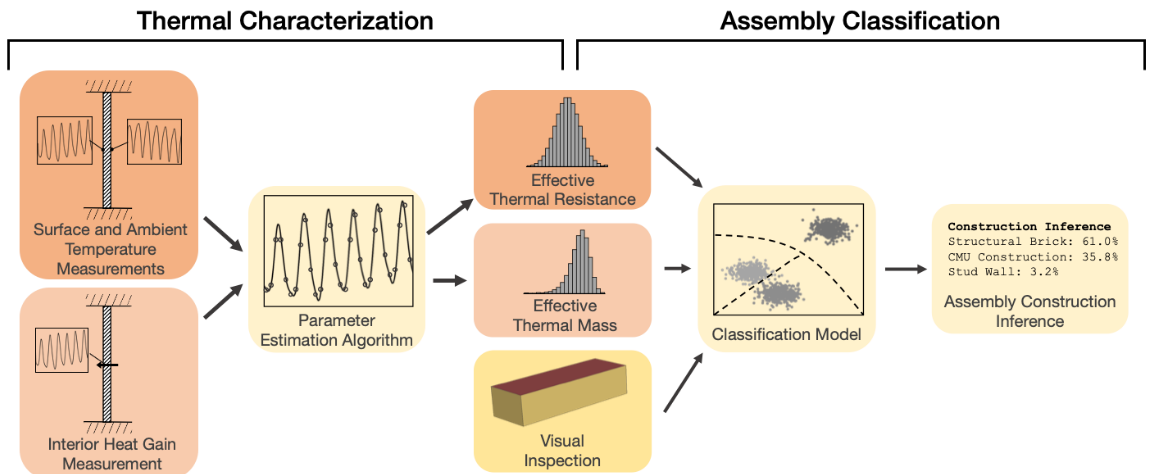

Figure 6.1 The proposed methodology framework for construction inference from in-situ thermal data.

From Figure 6.1, the proposed classification framework is displayed. This framework has three major stages: (1) thermal characterization, (2) classification, and (3) interpretation of results. This methodology specifically utilizes in-situ thermal data, namely effective thermal resistance and effective thermal mass, alongside a visual indication of assembly cladding, to infer the materiality of the candidate assembly. This model is built such that the input thermal resistance and thermal mass can be stochastic or deterministic, with stochastic inputs of N size producing N number of classifications and deterministic inputs producing singular, deterministic outputs. From there, the N outputs can be presented as percentages, which can be examined and grouped to infer the assembly's construction make-up.

6.1.1 Classification Model and Model Training Data

For the task of mapping input data to a classification, many multi-dimensional classification algorithms can be utilized. When accounting for the categorical data for cladding, alongside the thermal resistance and thermal mass features, this becomes a mixed-feature classification problem, which narrows the number of applicable classification algorithms. Support vector machines, neural networks, decision trees, and KNN algorithms are examples of classification algorithms that can be applied to this problem. For this proof-of-concept model, a KNN classifier will be utilized for its ease of computation and easy model interpretation for this proof-of-concept work.

To train the classification model, an input dataset is required. This dataset must be representative of the diverse set of in-service assemblies in the built environment, such that most assemblies which a user may interact with should be present in the training dataset. For this work, the ASHRAE wall database present in Table 16 and Table 18 in the ASHRAE Handbook of Fundamentals: Chapter 18 (ASHRAE, 2021) was utilized as a starting point. The ASHRAE Fundamentals database is a collection of typical new construction wall assemblies with their associated material layering and material thermal properties. In total, 66 wall assemblies are represented in this database. Two examples of wall assemblies from this database are displayed in Table 6.1.

Table 6.1 Two example assemblies with layer IDs from the ASHRAE Fundamentals Assembly Database.

Layer Number (Ext. to Int.)	Wall #13	Wall #63
1	25mm Stucco (F07)	200mm Heavyweight Concrete (M15)
2	13mm Fiberboard Sheathing (G03)	89mm Batt Insulation (I04)
3	89mm Batt Insulation (I04)	89mm Batt Insulation (I04)
4	16mm Gypsum Board (G01)	16mm Gypsum Board (G01)

From Table 6.1, two example wall assemblies, Wall #13 and Wall #63, from the ASHRAE Fundamentals assembly database are shown. The layer ID located in parentheses should also be noted, as these layer IDs correspond to a list of material thermal properties based on ASHRAE Fundamentals Chapter 26 material data. In total, this assembly database comprises 66 typical wall assemblies which range from stud walls to CMU and tilt-up concrete constructions.

While the ASHRAE fundamentals database provides a diverse set of wall assemblies to train the classification model with, there is a major limitation of this dataset—this assembly database is designed for new construction applications. Because of this dataset's application towards new construction, uninsulated or historic constructions are not represented in the dataset. This omission can potentially be a challenge, as 42% of residential wall assemblies in the United States are uninsulated (National Renewable

Energy Laboratory, 2019). Due to this, there is a high likelihood that one may encounter assemblies not represented in the ASHRAE Fundamentals assembly database.

To address this shortcoming, 19 additional wall constructions were generated and appended to the ASHRAE Fundamentals assembly list. These additional assemblies were designed to represent assemblies typically found in in-service buildings including:

- Uninsulated structural masonry walls.
- Uninsulated non-structural masonry walls.
- Uninsulated stud cavity walls.
- Stud walls with continuous insulation.

Each of these additional assemblies is composed of materials from the ASHRAE Fundamentals material list, so no additional materials were added to the database. In total, the edited construction dataset comprised 85 wall constructions, which are intended to represent a majority of constructions that would be encountered in a retrofit scenario.

With the 85 assembly classes identified, the effective thermal resistance and effective thermal capacitance of each assembly were required for model training and testing. To address this, each of the 85 assemblies was simulated in EnergyPlus for the TMY3 weather file of Atlanta, Georgia, and characterized utilizing Bayesian inference. To generate distinct training and testing datasets, walls were characterized during two different periods: (1) during the simulated first week of April, and (2) during the simulated second week of December.

For the two seasons, each assembly was stochastically characterized, providing 2,000 samples of effective thermal resistance and thermal capacitance for each of the 85 assemblies. These characterizations serve as a synthetic dataset since the model will be trained and evaluated based upon physics-based modeling simulating the real world. A scatter plot of each of the characterized effective thermal resistance and effective thermal mass values for each of the 85 assemblies are plotted in Figure 6.2. It should be noted that each shape and color corresponds to an individual assembly, with 2,000 data points plotted for each of the 85 assemblies. These were then separated into two datasets for model training and validation.

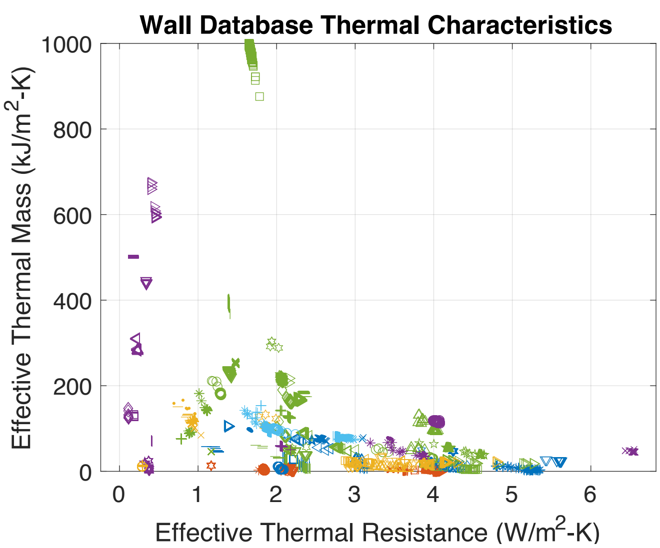

Figure 6.2 A scatter plot of thermal mass and thermal resistance values for the wall assembly dataset.

6.2 Model Training and Testing

6.2.1 Dataset Preparation

As previously mentioned, effective thermal resistance, effective thermal capacitance, and material information from visual inspections will be utilized within the classification model. Thermal resistance and thermal capacitance will be input into the model as numeric features, both of which differ greatly in magnitude. Due to the difference, both features were scaled via standard score normalization, also known as a z-score normalization. The equation for this scaling is shown below:

$$\bar{y} = \frac{y - \mu(y)}{\sigma(y)} \tag{55}$$

Where x is a numeric feature, $\mu(y)$ is the mean of feature's sample, $\sigma(y)$ is the standard deviation of feature's sample, and $\bar{y}$ is the standard score normalized feature. The normalization can be applied to both of the numeric features, allowing for scaling of these features to be of similar orders of magnitude. Feature scaling is especially important for distance-based algorithms such as KNN, where differing orders of magnitude between features can skew results and bias the model toward higher magnitude features.

Alongside numeric features, a categorical feature corresponding to cladding material was also utilized in the model. The goal of this feature is to encode information of an assembly's cladding material into the classification algorithm. This information can be easily determined via a photograph or visual inspection of the assembly. This feature is meant to distinguish relevant assemblies from irrelevant assemblies based upon cladding material. For example, if a wall with a brick cladding is instrumented, tested, and classified, the classification algorithm should logically not suggest that the assembly is constructed with wood siding. Encoding the exterior cladding information allows for the model to implicitly reduce the number of potential assemblies, which is especially important in the highly populated region of thermal mass values below 150 kJ/m^2-K as displayed in Figure 6.2.

To encode categorical features such as cladding material in a format usable for a machine learning algorithm, special care must be taken. The cladding feature is a categorical, non-ordinal feature, so the popular One-Hot Encoding (OHE) method was utilized to encode categorical variables into numeric data (W. Chen, 2016). OHE operates by transforming a list of N unique categories and M samples into a matrix of size *M*-by-*N* where every column corresponds to a specific category. When a category is selected for a given sample, that specific category will be denoted with a one, and all other categories will be zeros. An example of the OHE is shown in Table 6.2.

Table 6.2 An example visualization of One-Hot Encoding (OHE) for usage on categorical features.

Baseline Categorical Variable			**One-Hot Encoded Dummy Variable**			
	Cladding Category			"Brick"	"Wood Siding"	"Stucco"
Sample 1	"Brick"		Sample 1	1	0	0
Sample 2	"Wood Siding"		Sample 2	0	1	0
Sample 3	"Stucco"	→	Sample 3	0	0	1
Sample 4	"Brick"		Sample 4	1	0	0

6.2.2 Model Selection and Training

The KNN classification model that was utilized in this study is considered to be a lazy learner, as it does not learn from training data, but instead evaluates new model inputs against the training data for classification. In short, KNN calculates the distance between the candidate data and every datapoint within the training set. Once every distance is computed, the distances and their associated class labels are ordered from nearest to farthest, and the mode label of the first *K*-nearest data points is reported. One large advantage of KNN is that the model is explainable. Model parameters such as the distance function and the K-number of nearest neighbors can be tuned to increase KNN accuracy. To address modeler bias in model tuning, MATLAB's built-in hyperparameter optimizer was utilized to identify the optimum distance metric and best number of neighbors for the spring synthetic training dataset. The results of this model training and parameter tuning are shown in Table 6.3.

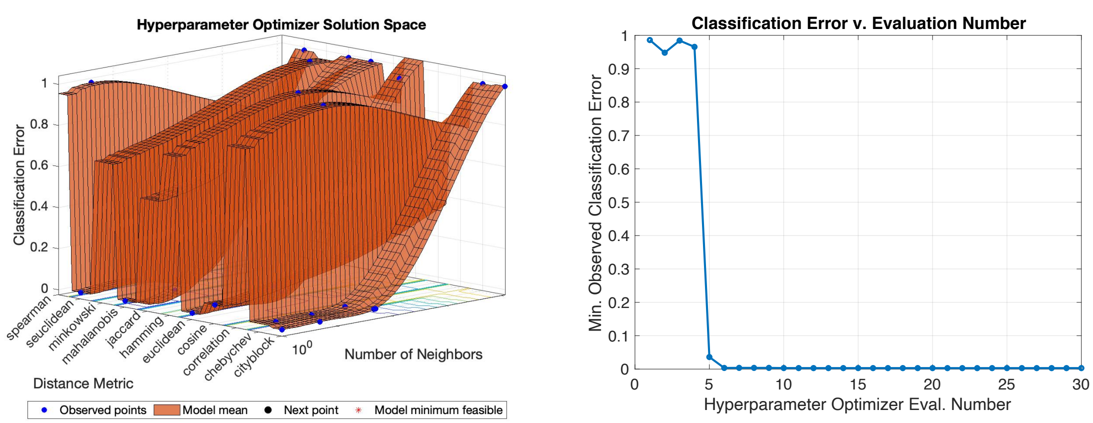

a) The hyperparameter solution space.

b) A graphical display of the hyperparameter optimizer's convergence.

Figure 6.3 Two graphs displaying the hyperparameter optimization for the KNN model.

From the figure, it can be noted that the classification error for standardized Euclidean, Euclidean, and city-block distance metrics produced similar results. It was also noted that any number of neighbors below 15 for these three distance metrics also produced similar results. This phenomenon is also shown in the asymptotic present after evaluation number 6 in the classification error versus evaluation number graph. While results were similar for these three metrics, the hyperparameter optimizer's best-observed parameter pair is that of a standardized Euclidean distance metric with 11 nearest neighbors. Because this parameter set was the optimum value, this set was selected for the proof-of-concept model evaluation and deployment.

6.2.3 Model Testing

With the model trained and optimized on the spring dataset, the model was evaluated on the winter dataset for testing. This testing dataset comprised 85,000 testing samples, with 1,000 occurrences of each of the 85 walls simulated in EnergyPlus and characterized for winter climatic conditions. To evaluate model performance, the results of this testing set were evaluated via the standard metrics of Precision, Recall, and the F1-Score, which is also known as the Sørensen–Dice coefficient (Dice, 1945). The equations for each of these testing metrics are shown in Eq. 56–58.

$$Precision = \frac{Number\ of\ Correct\ Class\ Predictions}{Number\ of\ Class\ Samples} \tag{56}$$

$$Recall = \frac{Number\ of\ Correct\ Class\ Predictions}{Number\ of\ Class\ Predictions} \tag{57}$$

$$F1 - Score = \frac{2 \times Recall \times Precision}{Recall + Precision} \tag{58}$$

From the above equations, the F1-score can be computed. It should be noted that the class macro-averaging scoring approach is utilized due to the large number of classes present in this classification model. The results of this testing are shown in Table 6.3.

Table 6.3 Testing performance metrics for the KNN classification model.

Metric	Macro-Averaged Score (%)	Standard Deviation of Score (%)
Precision	95.8%	18.7%
Recall	94.1%	20.6%
F1-Score	94.6%	19.5%

Table 6.3 showcases testing metric scores. It should be noted that all scores lie near an average value of approximately 95%, indicating robust model performance for the testing set. While the testing set scoring metrics display strong performance, the non-zero standard deviation of scores suggests the occurrence of misclassification. For example, the F1-score's standard deviation of 19.5% indicates that there are discrepancies in F1-scores between classes. When viewing these classification results in detail, it can be seen that 3 classes are never predicted by the model. While these misclassifications are technically a problem, these misclassifications are not drastically impactful from a practical perspective—e.g. two walls contain the same materials yet one wall has an air space and the other does not, or two similar walls with two inches of continuous insulation are misclassified a similar wall with a double stud construction rather than continuous insulation. Regardless of these discrepancies in three classes, the model fulfills the goal of classifying the general construction of an assembly.

6.3 Classification Model Spot Validation

With the model being trained and tested on synthetic datasets, it is important to validate the classification model with real-world data. To validate the classification model's performance, the characterization results from the Atlanta case were utilized. A photo of the Atlanta wall assembly is shown in Figure 6.4.

Figure 6.4 A photograph of the Atlanta case study wall.

This building was constructed around 1920 in Atlanta, Georgia, and was confirmed to be an uninsulated, brick mass wall via a previous renovation within the unit. This wall was instrumented with temperature sensors on the interior and exterior surfaces of the assembly, and an additional heat flux sensor was installed on the interior-facing surface of the wall. 100 hours of thermal data were recorded from the in-service assembly between 3/28/2021 and 4/1/2021, and this data was utilized to characterize the thermal properties of the assembly via Bayesian inference. The thermal performance of this assembly was characterized with a measured/simulation RMSE value of 0.624 W/m^2 over 100 hours. A histogram of the characterized effective thermal resistance and effective thermal capacitance values for the assembly are displayed in Figure 6.5.

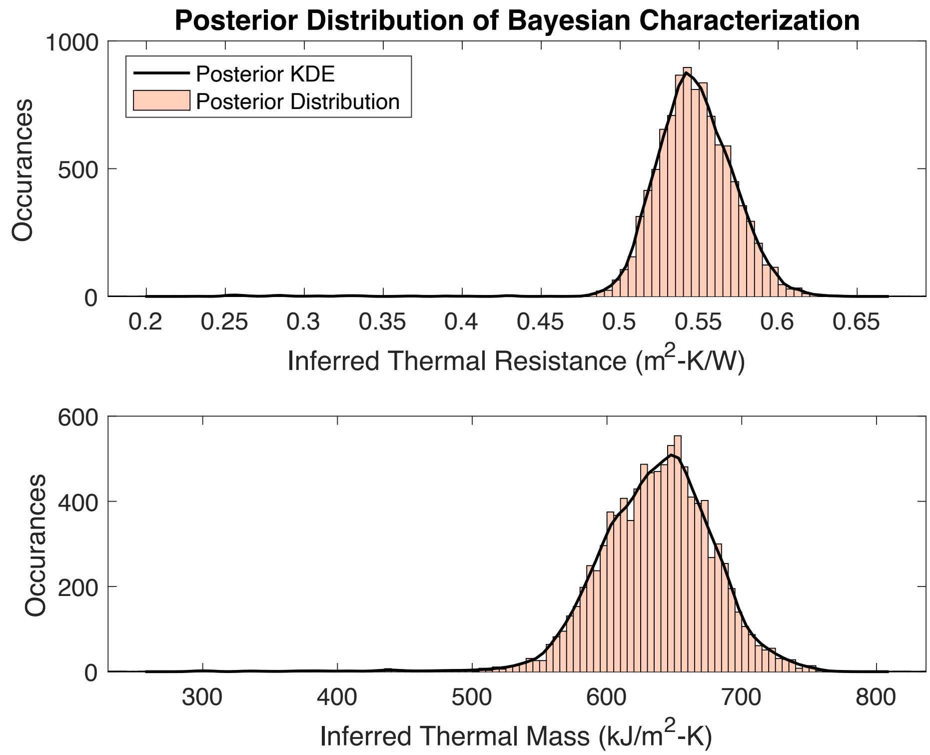

Figure 6.5 Histograms of the characterized thermal resistance and thermal mass for the Atlanta wall.

From Figure 6.5, it can be noted that the assembly was characterized to have a mean thermal resistance of 0.546 W/m^2-K with a standard deviation of 0.0294 W/m^2-K and a mean thermal capacitance of 636 kJ/m^2-K with a standard deviation of 43.7 kJ/m^2-K. This assembly was characterized via 10,000 Markov chain iterations, allowing for 10,000 discrete predictions of assembly composition. Utilizing this data alongside the cladding information, which was identified as brick via visual inspection, this assembly was classified via the proof-of-concept KNN classification model. Each of the Markov chain iterations was input into the classification model, which produced 10,000 predictions for the assembly's composition. The results of this classification are shown in Table 6.4.

Table 6.4 Assembly classification predictions for the Atlanta brick wall.

Wall ID	Percentage of Predictions (%)
Wall #72	98.0%
Wall #71	1.70%
Wall #70	0.300%

From these results, all of the Markov chain iterations were classified to be a brick mass wall, with Wall #70 being two bricks thick, Wall #71 being three bricks thick, and Wall #72 being four bricks thick. In short, these predictions all suggest that this assembly is an un-insulated brick mass wall. This prediction aligns with the ground truth information provided via the building manager, thus verifying the real-world validity of this KNN assembly classification algorithm.

6.4 Chapter Conclusion

In conclusion, the composition of building envelope assemblies can be predicted via in-situ thermal data and basic material identification. This paper developed an assembly dataset and proposed, trained, tested, and validated a proof-of-concept K-nearest neighbors classification model to predict wall assembly material composition via effective thermal resistance, effective thermal mass, and cladding material identification. This classification model was trained and tested to produce an average F1-score of 94.6% via synthetic datasets generated from physics-based simulation. This model was then verified via characterization of a 1920s mass wall that was tested in Atlanta, Georgia, where it correctly classified a 100-year-old, in-service wall assembly. This classification further suggests that this classification model has real-world validity with the potential to be deployed alongside current state-of-the-art in-situ thermal measurement techniques. This work enables retrofit stakeholders and decision-makers to non-destructively assess the make-up of in-service assemblies to inform envelop retrofit decisions, all without damaging or disturbing the assembly.

For future work, this classification model should be further evaluated to identify additional features or sources of data that may increase its performance and usability for non-technical audiences. Furthermore, work should be conducted to identify alternative classification algorithms, such as neural network or deep learning-based approaches which may provide additional value above the simplistic K-nearest neighbors approach utilized in this work. Finally, additional work should be conducted to guarantee the validity of this methodology in diverse climatic conditions with differing construction types.

CHAPTER 7: CONCLUSION

In conclusion, the US building stock is aging and few existing buildings are renovated or retrofitted annually. To enable retrofits, in-situ thermal testing, like R-value testing, can be employed to understand and model the thermal performance of an in-service assembly. One limitation of steady-state R-value testing is the omission of thermal mass, which causes modeling discrepancies of up to 27.3% for low mass assemblies and up to 52.4% for high mass assemblies when ignored. To support the characterization of thermal mass alongside thermal resistance testing, a methodology adapted from ASTM C1155's Sum of Least-Squares technique was proposed utilizing Bayesian inference and transient finite element heat transfer modeling. This methodology was verified via EnergyPlus simulations and validated via two real-world case studies on in-service wall assemblies. Transient thermal characterization allows for an existing assembly of unknown composition to be characterized and modeled in a non-destructive manner without disturbing the assembly. This characterization data can additionally be utilized with machine learning classification algorithms, such as K-nearest neighbors classifiers, to predict an assembly's composition and material makeup via characterized thermal mass, characterized thermal resistance, and the cladding material of the assembly. This characterization framework was verified via testing on a synthetic dataset with an average F1-Score of 94.6% and was validated via the previously mentioned real-world case study that occurred in Atlanta, Georgia. This work represents a comprehensive body of work related to in-situ transient thermal characterization and applications of this data to further inform non-destructive evaluation of building envelopes and enable envelope retrofits.

7.1 Research Questions Revisited

Alongside the developments made in transient characterization and assembly classification, this dissertation also set out to answer a series of questions. Each of these questions has been implicitly answered in respective chapters or case studies, but the answers to each are as follows:

1) Which methods apply to this compute the effective thermal properties of an existing building envelope assembly?

Through the literature survey present in Chapter 2, multiple thermal characterization and heat transfer calculation methods were evaluated. Two standards governing this practice are ASTM C1155 and ISO 9869-1. Both standards focus on an identical method for calculation of thermal resistance titled the "Summation Method" in ASTM C1155 and the "Average Method" in ISO 9869-1. Outside of this method prioritized in both standards, ASTM C1155 presents the "Sum of Least Squares Technique", which is an inverse problem approach to compute the effective thermal resistance and effective thermal capacitance of a single-material homogeneous layer with equivalent thermal performance to a complex, multi-layered envelope assembly. This method is strong as it computes thermal resistance and thermal capacitance rather than coefficients or correction factors representing an assembly. While this method is strong, the SLS method requires that sensors be built or probed inside of an assembly based upon the parameterization of the heat transfer problem as proposed by the method. Building upon the SLS method, it is possible to pose this heat transfer problem to allow for thermal characterization without the need for sensors to be located inside of the assembly.

Outside of the standards governing thermal characterization, an abridged review of approaches to simulate transient conduction was also conducted. For all of the methods reviewed, transient finite element heat transfer modeling stood apart, striking a balance between execution time, accuracy, and inverse modeling potential. This does not necessarily mean that this algorithm is the best heat transfer algorithm, but instead means that the finite element method is best suited for inverse modeling of envelope thermal mass and thermal resistance in a 1-dimensional space.

2) Can the sensors and methods from the state-of-the-art methods be utilized to non-destructively infer thermal mass and thermal resistance?

ASTM C1155's sum of least squares method utilizes heat flux sensors and two temperature sensors to characterize the effective thermal resistance of an assembly. One issue with this method is that "Compare [temperatures and heat fluxes] to measurements at the interior nodes where independent measurements are available." This means that the ASTM C1155 SLS method requires temperature and heat flux sensors to be located inside of the assembly, presumably installed during construction or via destructive instrumentation.

To address this issue with the ASTM C1155 SLS method, the problem was reformulated from a heat transfer problem with two temperature boundary conditions to a

1D heat transfer problem with one temperature boundary condition and one convective boundary condition. This approach is summarized in Figure 3.5. The advantage of this approach is that an assembly can be characterized by placing temperature and heat flux sensors on its surfaces, as opposed to located sensors inside of the assembly. One major disadvantage of this approach is that convection, or film coefficient, on the interior surface of the assembly now must be known; however, this coefficient can be approximated via ASTM C1155's summation method or ISO 9869-1's average method.

3) How can the proposed inverse modeling approach be verified against existing simulation workflows and validated for field deployment?

This inverse modeling approach was validated via EnergyPlus simulations of two multi-layered envelope assemblies. These two assemblies were characterized with mean RMSE values of 0.308 (0.136, 0.688) W/m^2 and 0.229 (0.149, 0.435) W/m^2, respectively. Additionally, characterized effective thermal resistances were within 1% of that which was modeled in the simulation.

To verify this inverse modeling approach, two case studies were conducted on in-service assemblies to verify real-world performance. The first case study was conducted on a wall assembly within a 1920s multifamily building located in Atlanta, Georgia. This experiment utilized calibrated equipment to measure temperatures and heat flux values for the 100-year old mass wall assembly, and the assembly was characterized with 48 hours of training data and produced a simulation/measured RMSE value of 0.805 (0.475, 1.30) W/m^2 over the 48-hour validation period. A second case study was undertaken through an independent dataset provided by Pacific Northwest National Laboratory. This dataset was collected from a stud wall test panel insulated with drill-and-fill blown cellulose insulation in Cloquet, Minnesota. This assembly was characterized with 48 hours of training data and produced a simulation/measured RMSE value of 1.34 (1.23, 1.45) W/m^2 over the 48-hour validation period. With these two experiments occurring in two differing climates (mixed-humid and very cold) and the two assemblies characterized differing drastically in composition (100-year old mass brick wall versus a newly-constructed insulated stud wall), these results suggest that this transient characterization methodology does have real-world validity. Additional testing should be conducted in other climates to further confirm the real-world validity of the method.

4) How long must an assembly be instrumented with sensors to infer thermal mass and thermal resistance?

To answer this question, 66 different wall assemblies were modeled and characterized with variable amounts of training data. These 66 assemblies were exacted from ASHRAE Fundamentals Chapter 18: Nonresidential Cooling and Heating Load Calculations. This chapter includes a list of typical building envelope materials, thermal properties of each material, and a list of 66 typical new construction wall assemblies designed to represent a majority of new construction wall assemblies in the western world. Each of these assemblies was simulated in EnergyPlus and characterized with time series training data spanning from 1 hour to 96 hours of data with a 48-hour validation dataset. Each of these assemblies was characterized, and it was found that the lower 95th percentile of data required was approximately 48 hours of training data for this simulation case study. These results suggest that sensors should log a minimum of 48 hours of in-situ thermal data to characterize an assembly. In practice, this is the functional minimum of data required—It is suggested that a validation dataset also be recorded to confirm the validity of the transient characterization.

5) What is the impact of thermal mass on envelope heat transfer, and is it required that thermal mass be measured alongside thermal resistance?

To address this question, the computed normalized root-mean-squared error values for each of the four characterization trials were analyzed. In each of these trials, transient and steady-state characterizations were conducted and characterization/reference NRMSE values were computed for each characterization. Across all four characterized assemblies, NRMSE was on average 3.06x larger for the steady-state characterizations compared to the transient characterizations. This steady-state/transient characterization error also appeared to become larger with more thermally-massive assemblies, with the lowest mass assembly having a steady-state error 1.28x larger than transient error, and the highest mass assembly having a steady-state error 4.83x larger than the transient characterization. These findings suggest that ignoring thermal resistance does have an impact on modeled thermal performance, even in assemblies traditionally thought of as being "low mass".

6) Can the measurement of thermal mass and thermal resistance be made beneficial to those without the specialized knowledge to simulate transient heat transfer?

In Chapter 6, a proof-of-concept machine learning methodology was proposed to classify assembly composition from effective thermal resistance, effective thermal mass, and the cladding material of an assembly. This classification model was trained and tested via a synthetic dataset generated via EnergyPlus simulations. This proof-of-concept methodology was designed to utilize the K-nearest neighbors classifier and produced a macro-averaged F1-score of 94.6%. This model was also applied to the Atlanta experiment, where the machine learning model predicted the assembly's composition as being 77.6% an un-insulated structural brick mass wall and 22.4% an insulated structural brick mass wall. These results align with the assembly's true composition, which is an uninsulated structural brick with a plaster interior surface finish.

While the machine learning approach displayed in Chapter 6 is a proof-of-concept, this machine learning application displays the potential to develop into an innovative approach to non-destructively characterize an assembly's composition via thermal testing. Significant further work should be conducted to improve the machine learning algorithm's performance, and additional in-situ testing data will be required to transition the model's training dataset from a synthetic dataset to one informed by physical testing of diverse assemblies across diverse climatic conditions.

7.2 Future Work

Due to the scope of this work, future work can take many forms. First, additional work should be conducted to apply the thermal characterization workflow to envelope defects, such as thermal bridging or moisture-laden assemblies. It is believed that this approach can be applied to these assemblies, but defects and their vast multi-dimensional complexity were deemed outside of the scope of this work. This work should be first conducted via test panels with known defects, then evaluated within the field on real deteriorating or failing envelope assemblies.

Secondly, additional work should be conducted to bolster the classification model proposed within Chapter 6. This KNN classification model was designed to be a proof-of-concept approach to classify assembly materiality; however, additional work should be conducted to generate datasets based upon real data as opposed to the synthetic dataset utilized to train and test the model. Additionally, the KNN model was selected due to its ability to be explained, not based on its performance. KNN is considered to be a "lazy learner" and does not actually learn any information from the training data; instead, KNN simply classifies based upon the nearest datum from the training set. Because KNN does not actually learn from data, it is suggested that this problem be revisited via a sophisticated classification approach that does learn and identify patterns through data.

Thirdly, the thermal characterization method proposed within the dissertation is a physics-based model which informs a Bayesian inference algorithm for parameter estimation. Future work should be conducted to approach this problem from a deep learning point of view. Utilizing early developments in model-free methods, it may be possible to identify effective thermal resistance, effective thermal capacitance, and assembly materiality via deep learning or a combination of mixed-fidelity modeling to remove the need for the computationally costly Bayesian inference approach. Additionally, future research should be conducted to replace the transient finite element heat transfer model with a data-driven model rather than a physics-based model, which would drastically speed up execution times while still maintaining usage of the Bayesian inference workflow. Examples of these types of data-driven modeling approaches can be found within the field of computation finance, where governing equations for underlying phenomena are often unknown.

Finally, future work should be conducted to apply this thermal characterization workflow in the field to identify how it can add value to building audits and retrofits. As discussions on how to address our aging, poorly-performing building stock are on-going, the need to understand the in-situ thermal performance of our building's envelopes will continue to become more important.

REFERENCES

Aïssani, A., Chateauneuf, A., Fontaine, J. P., & Audebert, P. (2016). Quantification of workmanship insulation defects and their impact on the thermal performance of building facades. *Applied Energy*. https://doi.org/10.1016/j.apenergy.2015.12.040

Al-Sanea, S. A. (2003). Finite-volume thermal analysis of building roofs under two-dimensional periodic conditions. *Building and Environment*. https://doi.org/10.1016/S0360-1323(03)00068-4

Alawadhi, E. M. (2008). Thermal analysis of a building brick containing phase change material. *Energy and Buildings*. https://doi.org/10.1016/j.enbuild.2007.03.001

Alawadhi, E. M. (2012). Using phase change materials in window shutter to reduce the solar heat gain. *Energy and Buildings*. https://doi.org/10.1016/j.enbuild.2011.12.009

Alshatshati, S. F. (2017). *Estimating Envelope Thermal Characteristics From Single Point in Time Thermal Images* [University of Dayton]. https://pdfs.semanticscholar.org/ee4b/4c1803850f5fa07edc183ad9ed7f27f88e02.pdf

Altman, N. S. (1992). An Introduction to Kernel and Nearest-Neighbor Nonparametric Regression. *The American Statistician*, *46*(3), 175–185. https://doi.org/10.1080/00031305.1992.10475879

Anderson, B. A., & Singh, R. P. (2006). Effective heat transfer coefficient measurement during air impingement thawing using an inverse method. *International Journal of Refrigeration*. https://doi.org/10.1016/j.ijrefrig.2005.05.016

Antonopoulos, K. A., & Koronaki, E. (1998). Apparent and effective thermal capacitance of buildings. *Energy*. https://doi.org/10.1016/S0360-5442(97)00088-1

Architecture 2030. (2018). *Architecture 2030 - Existing Buildings*. https://architecture2030.org/existing-buildings-operation/

ASHRAE. (1989). 1989 ASHRAE Handbook of Fundamentals. *American Society of Heating, Refrigerating, and Air Conditioning Engineers*, *4*.

ASHRAE. (2013). *2013 ASHRAE Handbook of Fundamentals*. ASHRAE. https://www.ashrae.org/technical-resources/ashrae-handbook

ASHRAE. (2021). *2021 ASHRAE Handbook — Fundamentals*. https://www.ashrae.org/technical-resources/ashrae-handbook

ASTM. (2013a). *ASTM C1046: Standard Practice for In-Situ Measurement of Heat Flux and Temperature on Building Envelope Components*. https://www.astm.org/Standards/C1046.htm

ASTM. (2013b). *ASTM C1155: Standard Practice for Determining Thermal Resistance of Building Envelope Components from the In-Situ Data*.

https://www.astm.org/Standards/C1155.htm

ASTM. (2019). *ASTM E644: Standard Test Methods for Testing Industrial Resistance Thermometers*. https://www.astm.org/Standards/E644.htm

Barreira, E., & de Freitas, V. P. (2007). Evaluation of building materials using infrared thermography. *Construction and Building Materials*, *21*(1), 218–224. https://doi.org/10.1016/j.conbuildmat.2005.06.049

Beck, J. V., & Arnold, K. J. (1977). *Parameter estimation in engineering and science*. James Beck.

Beck, J. V, Petrie, T. W., & Courville, G. E. (1991). Using parameter estimation to analyze building envelope thermal performance. *Special Report*, *9*(3), 161–191. https://erdc-library.erdc.dren.mil/jspui/bitstream/11681/11625/1/SR-91-3.pdf

Bénard, C., Guerrier, B., & Rosset-Louerat, M. M. (1992). Optimal Building Energy Management: Part I—Modeling. *Journal of Solar Energy Engineering*, *114*(2). https://asmedigitalcollection.asme.org/solarenergyengineering/article-abstract/114/1/2/419966?casa_token=nXSTCLSQ_UgAAAAA:D7WsM2F61lxRaKtW-T2Tt7V4BWOmmXhIhfVgw1z5fC9ZkvQniVL5Mvw0qqOXY1dS3BWUHK_n

Bierlaire, M. (2015). Simulation and optimization: A short review. *Transportation Research Part C: Emerging Technologies*, *55*, 4–13. https://doi.org/10.1016/j.trc.2015.01.004

Box, G. E. P., & Tiao, G. C. (1973). *Bayesian inference in statistical analysis*. John Wiley & Sons.

Braun, J., & Chaturvedi, N. (2002). An Inverse Gray-Box Model for Transient Building Load Prediction. *HVAC&R Research*, *8*(1), 73–99. https://doi.org/10.1080/10789669.2002.10391290

Breiman, L. (2001). Random forests. *Machine Learning*, *45*(1), 5–32.

Cai, J., & Braun, J. E. (2012). Efficient and robust training methodology for inverse building modeling. *Proceedings of SimBuild*, *5*(1), 456–461. http://www.ibpsa-usa.org/index.php/ibpusa/article/view/463

Chaudhary, G., New, J., Sanyal, J., Im, P., O'Neill, Z., & Garg, V. (2016). Evaluation of "Autotune" calibration against manual calibration of building energy models. *Applied Energy*. https://doi.org/10.1016/j.apenergy.2016.08.073

Chen, K., Reichard, G., Akanmu, A., & Xu, X. (2021). Geo-registering UAV-captured close-range images to GIS-based spatial model for building façade inspections. *Automation in Construction*, *122*, 103503. https://doi.org/10.1016/j.autcon.2020.103503

Chen, K., Reichard, G., Xu, X., & Akanmu, A. (2021). Automated crack segmentation in close-range building façade inspection images using deep learning techniques. *Journal of Building Engineering*, *43*, 102913.

https://doi.org/10.1016/j.jobe.2021.102913

Chen, W. (2016). *Learning with Scalability and Compactness*. Washington University in St. Louis. https://openscholarship.wustl.edu/cgi/viewcontent.cgi?article=1155&context=eng_etds

Childs, K. W., Courville, G. E., & Bales, E. L. (1983). *Thermal mass assessment: an explanation of the mechanisms by which building mass influences heating and cooling energy requirements*. https://doi.org/10.2172/5788833

Cui, B., Dong, J., Munk, J., Mao, N., & Kuruganti, T. (2018). *A simplified regression building thermal modelling method for detached two floor house in U.S.* https://www.osti.gov/servlets/purl/1461939

Curcija, C., & Pallin, S. (2018). *THERMM: Heat & Moisture Modeling Tool*. https://www.energy.gov/sites/prod/files/2018/06/f52/35390_Curcija_050318-930.pdf

Deeb, E., & LeWinter, A. (2018). *Building envelope assessment using thermal infrared and lidar scanning : Palmer Station, Antarctica*. https://doi.org/10.21079/11681/27353

Deru, M., Field, K., Studer, D., Benne, K., Griffith, B., Torcellini, P., Liu, B., Halverson, M., Winiarski, D., Rosenberg, M., & others. (2011). *US Department of Energy commercial reference building models of the national building stock*. National Renewable Energy Laboratory. https://digitalscholarship.unlv.edu/cgi/viewcontent.cgi?article=1045&context=renew_pubs

Dhekne, A., Gowda, M., Zhao, Y., Hassanieh, H., & Choudhury, R. R. (2018). LiquID. *Proceedings of the 16th Annual International Conference on Mobile Systems, Applications, and Services*, 442–454. https://doi.org/10.1145/3210240.3210345

Dice, L. R. (1945). Measures of the Amount of Ecologic Association Between Species. *Ecology*, *26*(3), 297–302. https://doi.org/10.2307/1932409

DOE. (2012). *Energy Department Announces Six Projects to Develop Energy-Saving Windows, Roofs, and Heating and Cooling Equipment*. https://www.energy.gov/articles/energy-department-announces-six-projects-develop-energy-saving-windows-roofs-and-heating

DOE. (2021a). *EnergyPlus Version 9.5.0 Engineering Reference*. https://energyplus.net/sites/all/modules/custom/nrel_custom/pdfs/pdfs_v9.5.0/EngineeringReference.pdf

DOE. (2021b). *EnergyPlus Weather Data*. https://energyplus.net/weather

EIA. (2012). *2012 Commercial Buildings Energy Consumption Survey (CBECS)*. https://www.eia.gov/consumption/commercial/data/2012/bc/pdf/b1-b46.pdf

Ekelof, S. (2001). The genesis of the Wheatstone bridge. *Engineering Science \& Education Journal*, *10*(1), 37–40.

El Masri, Y., & Rakha, T. (2020). A scoping review of non-destructive testing (NDT) techniques in building performance diagnostic inspections. *Construction and Building Materials*, *265*, 120542. https://doi.org/10.1016/j.conbuildmat.2020.120542

Fister, I., Yang, X.-S., Fister, I., Brest, J., & Fister, D. (2013). *A Brief Review of Nature-Inspired Algorithms for Optimization*. http://arxiv.org/abs/1307.4186

FluxTeq. (2016). *R-Value Measurement Instruction Manual*.

FluxTeq. (2020). *PHFS Heat Flux Sensor Instruction Manual*.

Fraisse, G., Viardot, C., Lafabrie, O., & Achard, G. (2002). Development of a simplified and accurate building model based on electrical analogy. *Energy and Buildings*, *34*(10), 1017–1031. https://doi.org/10.1016/S0378-7788(02)00019-1

Fux, S. F., Ashouri, A., Benz, M. J., & Guzzella, L. (2014). EKF based self-adaptive thermal model for a passive house. *Energy and Buildings*, *68*(PART C), 811–817. https://doi.org/10.1016/j.enbuild.2012.06.016

Garrido, I., Barreira, E., M.S.F. Almeida, R., & Lagüela, S. (2022). Introduction of active thermography and automatic defect segmentation in the thermographic inspection of specimens of ceramic tiling for building façades. *Infrared Physics & Technology*, *121*, 104012. https://doi.org/10.1016/j.infrared.2021.104012

Gelman, A., Carlin, J. B., Stern, H. S., Dunson, D. B., Vehtari, A., & Rubin, D. B. (2013). *Bayesian data analysis*. CRC press.

Haario, H., Laine, M., Mira, A., & Saksman, E. (2006). DRAM: efficient adaptive MCMC. *Statistics and Computing*, *16*(4), 339–354.

Haario, H., Saksman, E., Tamminen, J., & others. (2001). An adaptive Metropolis algorithm. *Bernoulli*, *7*(2), 223–242.

Haberl, J. S., & Bou-Saada, T. E. (1998). Procedures for Calibrating Hourly Simulation Models to Measured Building Energy and Environmental Data. *Journal of Solar Energy Engineering*, *120*(3), 193–204. https://doi.org/10.1115/1.2888069

Hasse, C., Grenet, M., Bontemps, A., Dendievel, R., & Sallée, H. (2011). Realization, test and modelling of honeycomb wallboards containing a Phase Change Material. *Energy and Buildings*. https://doi.org/10.1016/j.enbuild.2010.09.017

Hastings, W. K. (1970). Monte Carlo sampling methods using Markov chains and their applications. *Biometrika*, *57*(1), 97–109. https://doi.org/10.1093/biomet/57.1.97

Henninger, R. H., & Witte, M. J. (2011). EnergyPlus testing with ASHRAE 1052-RP Toolkit--Building fabric analytical tests. *Lawrence Berkeley National Laboratory, USA*. https://energyplus.net/sites/all/modules/custom/nrel_custom/eplus_files/current_testi ng_reports/ASHRAE1052RP-8.3.0-b45b06b780.pdf

Heo, Y., Choudhary, R., & Augenbroe, G. A. (2012). Calibration of building energy models for retrofit analysis under uncertainty. *Energy and Buildings*. https://doi.org/10.1016/j.enbuild.2011.12.029

Hittle, D C, & Pedersen, C. O. (1981). Calculating building heating loads using the frequency response of multi-layered slabs.[BLAST code, NBSLD code]. *ASHRAE Trans.;(United States)*, *87*(CONF-810657-). https://www.osti.gov/biblio/6340456

Hittle, Douglas Carl. (1979). *The Building Loads Analysis and System Thermodynamics (blast) Program, Version 2.0: User's Manual*. NTIS.

Hudson, G., & Underwood, C. P. (1999). A Simple Building Modelling Procedure for MATLAB / SIMULINK. *Building Simulaiton 1999*, 1–7. www.ibpsa.org/%5Cproceedings%5CBS1999%5CBS99_PA-05.pdf

Hukseflux. (2021). *USER MANUAL TRSYS01: High-accuracy building thermal resistance measuring system with two measurement locations*.

IEA. (2019). *IEA Energy Efficiency: Buildings*. https://www.iea.org/topics/energyefficiency/buildings/

ISO. (2014). *ISO 9869-1: In-Situ Measurement of Thermal Resistance and Thermal Transmittance*. https://www.iso.org/standard/59697.html

Iu, C. (2002). *CTF/PRFGenerator*. http://www.hvac.okstate.edu/resources.html

Janssen, H., Blocken, B., & Carmeliet, J. (2007). Conservative modelling of the moisture and heat transfer in building components under atmospheric excitation. *International Journal of Heat and Mass Transfer*. https://doi.org/10.1016/j.ijheatmasstransfer.2006.06.048

Jasiński, R., Drobiec, Ł., & Mazur, W. (2019). Validation of Selected Non-Destructive Methods for Determining the Compressive Strength of Masonry Units Made of Autoclaved Aerated Concrete. *Materials*, *12*(3), 389. https://doi.org/10.3390/ma12030389

Khoshbakht, M., Lin, M. W., & Feickert, C. A. (2009). A finite element model for hygrothermal analysis of masonry walls with FRP reinforcement. *Finite Elements in Analysis and Design*. https://doi.org/10.1016/j.finel.2009.02.007

Koo, C., Park, S., Hong, T., & Park, H. S. (2014). An estimation model for the heating and cooling demand of a residential building with a different envelope design using the finite element method. *Applied Energy*, *115*, 205–215. https://doi.org/10.1016/j.apenergy.2013.11.014

Koschenz, M. (1999). Calculation of surface temperature in DOE-2. *The Building Energy Simulation User News*, *20*(2).

Kramer, R. P., & van Schijndel, A. W. M. (2012). Inverse modeling of climate responses of monumental buildings. *ArXiv Preprint ArXiv:1206.4438*.

Kramer, R., van Schijndel, J., & Schellen, H. (2013). Inverse modeling of simplified hygrothermal building models to predict and characterize indoor climates. *Building and Environment*. https://doi.org/10.1016/j.buildenv.2013.06.001

Krutz, G. W., Schoenhals, R. J., & Horc, P. S. (1978). Application of the Finite-Element Method to the Inverse Heat Conduction Problem. *Numerical Heat Transfer*, *1*(4), 489–498. https://doi.org/10.1080/10407797809412181

Kumar, R., & Kaushik, S. C. (2005). Performance evaluation of green roof and shading for thermal protection of buildings. *Building and Environment*. https://doi.org/10.1016/j.buildenv.2004.11.015

Kummert, M., André, P., & Nicolas, J. (1996). Development of Simplified Models for Solar Buildings Optimal Control. *EuroSun'96*, 1055–1061. https://pdfs.semanticscholar.org/8b17/55e136e9020ef6add676d8f6ddde82290ab0.pdf

Laine, M. (2008). *Adaptive MCMC methods with applications in environmental and geophysical models*. Finnish Meteorological Institute.

Lee, K., & Braun, J. E. (2016). Development and application of an inverse building model for demand response in small commercial buildings. *Proceedings of SimBuild*, *1*(1). http://ibpsa-usa.org/index.php/ibpusa/article/view/121

Li, L. P., Wu, Z. G., Li, Z. Y., He, Y. L., & Tao, W. Q. (2008). Numerical thermal optimization of the configuration of multi-holed clay bricks used for constructing building walls by the finite volume method. *International Journal of Heat and Mass Transfer*, *51*(13–14), 3669–3682. https://doi.org/10.1016/j.ijheatmasstransfer.2007.06.008

Li, Q. (2017). *Addressing data informativeness in risk-conscious building performance simulation applications*. Georgia Institute of Technology.

Li, X. Q., Chen, Y., Spitler, J. D., & Fisher, D. (2009). Applicability of calculation methods for conduction transfer function of building constructions. *International Journal of Thermal Sciences*. https://doi.org/10.1016/j.ijthermalsci.2008.11.006

Liñán, C. R., Morales Conde, M. J., de Hita, P. R., & Gálvez, F. P. (2015). Application of Non-Destructive Techniques in the Inspection of Wooden Structures of Protected Buildings: The Case of Nuestra Señora de los Dolores Church (Isla Cristina, Huelva). *International Journal of Architectural Heritage*, *9*(3), 324–340. https://doi.org/10.1080/15583058.2013.771292

Lorenz, F., & Masy, G. (1982). Méthode d'évaluation de l'économie d'énergie apportée par l'intermittence de chauffage dans les bâtiments: Traitement par differences finies d'un model a deux constantes de temps. In *Faculte des Sciences Appliquees*.

Lü, X. (2002). Modelling of heat and moisture transfer in buildings: I. Model program.

Energy and Buildings. https://doi.org/10.1016/S0378-7788(02)00021-X

Luo, C., Moghtaderi, B., Sugo, H., & Page, A. (2008). A new stable finite volume method for predicting thermal performance of a whole building. *Building and Environment*. https://doi.org/10.1016/j.buildenv.2006.11.037

Mendon, V. V, Taylor, Z. T., Rao, S. U., & Xie, Y. L. (2015). *2015 IECC : Energy Savings Analysis*. *May*.

Metropolis, N., Rosenbluth, A. W., Rosenbluth, M. N., Teller, A. H., & Teller, E. (1953). Equation of state calculations by fast computing machines. *The Journal of Chemical Physics*, *21*(6), 1087–1092.

Mitalas, G. P., & Stephenson, D. G. (1967). Room Thermal Response Factors. *Transactions of the American Society of Heating, Refrigerating, and Air Conditioning Engineers*, *73*. http://web.mit.edu/parmstr/Public/NRCan/rp342.pdf

Modera, M. P., Sherman, M. H., & Sonderegger, R. C. (1985). Determining the U-value of a wall from field measurements of heat flux and surface temperatures. In *Building Applications of Heat Flux Transducers*. ASTM International. https://escholarship.org/content/qt7rv2z4vv/qt7rv2z4vv.pdf

Mohamed, I. O. (2008). An inverse lumped capacitance method for determination of heat transfer coefficients for industrial air blast chillers. *Food Research International*. https://doi.org/10.1016/j.foodres.2008.01.005

National Renewable Energy Laboratory. (2019). *ResStock*. Data Viewer: National Baseline (EFS V2).

NIST. (n.d.). Lauda Ecoline E100 Immersion Thermostat. In *2012*. https://www.nist.gov/laboratories/tools-instruments/lauda-ecoline-e100-immersion-thermostat

Omega Engineering. (n.d.). *Revised Thermocouple Reference Tables: Type T*. https://assets.omega.com/pdf/tables_and_graphs/thermocouple-type-t-fahrenheit.pdf

Omega Engineering. (2019). *Thermocouple Types*. https://www.omega.com/en-us/resources/thermocouple-types

Ozel, M. (2011). Effect of wall orientation on the optimum insulation thickness by using a dynamic method. *Applied Energy*. https://doi.org/10.1016/j.apenergy.2011.01.049

Pallin, S., Boudreaux, P., Shrestha, S., New, J., & Adams, M. (2017). State-of-the-Art for hygrothermal simulation tools (draft). *Ornl*.

Park, Y., & Guldmann, J.-M. (2019). Creating 3D city models with building footprints and LIDAR point cloud classification: A machine learning approach. *Computers, Environment and Urban Systems*, *75*, 76–89. https://doi.org/10.1016/j.compenvurbsys.2019.01.004

Peavy, B. (1977). NOTE ON RESPONSE FACTORS AND CONDUCTION

TRANSFER-FUNCTION. *ASHRAE JOURNAL-AMERICAN SOCIETY OF HEATING REFRIGERATING AND AIR-CONDITIONING ENGINEERS*, *19*(12), 35. https://www.google.com/url?sa=t&rct=j&q=&esrc=s&source=web&cd=3&ved=2ahUKEwi9upXBpe3kAhXkUN8KHQTlC5wQFjACegQIAxAC&url=http%3A%2F%2Fweb.mit.edu%2Fparmstr%2FPublic%2Fhittle.doc&usg=AOvVaw1TvcxIQHCldz0NdU0ACBeJ

Peralta, M. (2012). *Propagation of Errors: How to Mathematically Predict Measurement Errors*. Createspace Independent Pub. https://books.google.com/books?id=MZhQLwEACAAJ

Peskun, P. H. (1973). Optimum monte-carlo sampling using markov chains. *Biometrika*, *60*(3), 607–612.

Protiva, P., Mrkvica, J., & Machac, J. (2011). Estimation of Wall Parameters From Time-Delay-Only Through-Wall Radar Measurements. *IEEE Transactions on Antennas and Propagation*, *59*(11), 4268–4278. https://doi.org/10.1109/TAP.2011.2164206

Rakha, T., Liberty, A., Gorodetsky, A., Kakillioglu, B., & Velipasalar, S. (2018). Heat Mapping Drones: An Autonomous Computer-Vision-Based Procedure for Building Envelope Inspection Using Unmanned Aerial Systems (UAS). *Technology|Architecture + Design*, *2*(1), 30–44. https://doi.org/10.1080/24751448.2018.1420963

Ramos, N., Delgado, J., Barreira, E., & De Freitas, V. (2010). Hygrothermal numerical simulation: application in moisture damage prevention. In L. Angermann (Ed.), *Applications in Computational Fluid Dynamics*. InTech. https://books.google.com/books?id=N9CcDwAAQBAJ&lpg=PA97&ots=tjvGu0_jkG&dq=Hygrothermal Numerical Simulation%3A Application in Moisture Damage Prevention&lr&pg=PR2#v=onepage&q=Hygrothermal Numerical Simulation: Application in Moisture Damage Prevention&f=f

Reddy, J. N., & Gartling, D. K. (2010). *The Finite Element Method in Heat Transfer and Fluid Dynamics, Third Edition* (3rd ed.). CRC Press. https://doi.org/10.1201/9781439882573

Reddy, T. A. (2006). Literature review on calibration of building energy simulation programs: uses, problems, procedures, uncertainty, and tools. *ASHRAE Transactions*, *112*, 226. https://search.proquest.com/docview/192562738?pq-origsite=gscholar

Royapoor, M., & Roskilly, T. (2015). Building model calibration using energy and environmental data. *Energy and Buildings*. https://doi.org/10.1016/j.enbuild.2015.02.050

Seem, J. E. (1987). *Modeling of heat transfer in buildings.*

Segerlind, L. J. (1976). *Applied Finite Element Analysis*. Wiley.

Sévigny, P., & Fournier, J. (2017). *Automated Front Wall Feature Extraction and Material Assessment Using Fused LIDAR and Through-Wall Radar Imagery*.

https://www.sto.nato.int/publications/STO Meeting Proceedings/STO-MP-SET-241/MP-SET-241-10-4.pdf

Shankle, D. L., Merrick, J. A., & Gilbride, T. L. (1994). *A History of the Building Energy Standards Program*. https://doi.org/10.2172/10154655

Spitler, J. D., & Fisher, D. E. (1999). Development of periodic response factors for use with the radiant time series method. *Ashrae Transactions*, *105*(2), 491–509.

Spitler, J. D., Fisher, D. E., & Pedersen, C. O. (1997). *The radiant time series cooling load calculation procedure*. https://www.osti.gov/biblio/349986

Steinhart, J. S., & Hart, S. R. (1968). Calibration Curves for Thermistors. *Deep Sea Research and Oceanographic Abstracts*, *15*(4), 497–503. https://doi.org/10.1016/0011-7471(68)90057-0

Strand, R., Buhl, F. W. F., Huang, J., & Taylor, R. (1999). Enhancing and extending the capabilities of the building heat balance simulation technique for use in EnergyPlus. *In Proceedings of Building Simulation'99, Volume II*.

Strand, R. K. (2001). Modularization and simulation techniques for heat balance based energy and load calculation programs: The experience of the ASHRAE loads toolkit and EnergyPlus. *Proceedings of Building Simulation 2001*. http://www.ibpsa.org/proceedings/BS2001/BS01_0043_50.pdf

Straube, J. (2007). Thermal metrics for high performance enclosure walls: The limitations of R-Value. *Building Science Corporation, Research Report--0901*. https://www.buildingscience.com/sites/default/files/migrate/pdf/RR-0901_Thermal_Metrics.pdf

Sujatmiko, W., Suhedi, F., & Rumiawati, A. (2016). Thermal resistance measurements of building envelope components of the minang traditional house using the heat flow method. *2016 International Seminar on Sensors, Instrumentation, Measurement and Metrology (ISSIMM)*, 88–92. https://doi.org/10.1109/ISSIMM.2016.7803729

Tabares-Velasco, P. C., Christensen, C., Bianchi, M., & Booten, C. (2012). *Verification and Validation of EnergyPlus Conduction Finite Difference and Phase Change Material Models for Opaque Wall Assemblies*. https://www.nrel.gov/docs/fy12osti/55792.pdf

Tarantola, A. (2005). *Inverse problem theory and methods for model parameter estimation*. SIAM.

Taylor, T., Counsell, J., & Gill, S. (2014). Combining thermography and computer simulation to identify and assess insulation defects in the construction of building faç ades. *Energy and Buildings*, *76*, 130–142. https://doi.org/10.1016/j.enbuild.2014.02.080

Texas Instruments. (2019). *ADS111x ultra-small, low-power, I2C-compatible, 860-SPS, 16-bit ADCs with internal reference, oscillator, and programmable comparator*.

https://www.ti.com/lit/gpn/ADS1113

Tian, W., Wang, Q., Song, J., & Wei, S. (2014). Calibrating dynamic building energy models using regression model and bayesian analysis in building retrofit projects. *International Building Performance Simulation Association*.

Tierney, L., & Mira, A. (1999). Some adaptive Monte Carlo methods for Bayesian inference. *Statistics in Medicine*, *18*(17–18), 2507–2515.

Tseng, A. A., Chen, T. C., & Zhao, F. Z. (1995). DIRECT SENSITIVITY COEFFICIENT METHOD FOR SOLVING TWO-DIMENSIONAL INVERSE HEAT CONDUCTION PROBLEMS BY FINITE-ELEMENT SCHEME. *Numerical Heat Transfer, Part B: Fundamentals*, *27*(3), 291–307. https://doi.org/10.1080/10407799508914958

van Schijndel, A. W. M. (2009). The Exploration of an Inverse Problem Technique to Obtain Material Properties of a Building Construction. In *4th International Building Physics Conference*.

Venter, G. (2010). *Review of optimization techniques*.

Vidanovic, D. S., Curcija, D. C., Salonvaara, M., & Pallin, S. (2021). *THERM 8 Technical Documentation--New Hygrothermal Modeling Functionality*.

Walton, G. N. (1983). Thermal Analysis Research Program Reference Manual. *National Bureau of Standards, March*. https://www.govinfo.gov/content/pkg/GOVPUB-C13-6176908b08a357a0ac91a8ab3db55b97/pdf/GOVPUB-C13-6176908b08a357a0ac91a8ab3db55b97.pdf

Wan, E. A. (1990). Neural network classification: a Bayesian interpretation. *IEEE Transactions on Neural Networks*, *1*(4), 303–305. https://doi.org/10.1109/72.80269

Wang, S., & Xu, X. (2006). Parameter estimation of internal thermal mass of building dynamic models using genetic algorithm. *Energy Conversion and Management*. https://doi.org/10.1016/j.enconman.2005.09.011

Witte, M. J., Henninger, R. H., & Crawley, D. B. (2016). Experience testing EnergyPlus with the ASHRAE 1052-RP building fabric analytical tests. *Proceedings of SimBuild*, *1*(1). https://ibpsa-usa.org/index.php/ibpusa/article/download/142/127

Yang, S., Pilet, T. J., & Ordonez, J. C. (2018). Volume element model for 3D dynamic building thermal modeling and simulation. *Energy*, *148*, 642–661. https://doi.org/10.1016/j.energy.2018.01.156

Yao, W., Chen, X., Luo, W., van Tooren, M., & Guo, J. (2011). Review of uncertainty-based multidisciplinary design optimization methods for aerospace vehicles. *Progress in Aerospace Sciences*, *47*(6), 450–479. https://doi.org/10.1016/j.paerosci.2011.05.001

Yoon, J., Lee, E.-J., & Claridge, D. E. (2003). Calibration procedure for energy performance simulation of a commercial building. *Journal of Solar Energy*

Engineering, *125*(3), 251–257. https://doi.org/10.1115/1.1564076

York, D. A., & Cappiello, C. C. (1981). *DOE-2 engineers manual (Version 2. 1A)*. http://doe2.com/Download/Doe-21e/DOE-2engineersmanualversion2.1A.Pdf

Zhu, Q., Xu, X., & Yu, J. (2012). Study of dynamic thermal performance of active pipe-embedded building envelopes based on frequency-domain finite difference method. *ASim 2012 IBPSA Asia Conference, Shanghai*. https://pdfs.semanticscholar.org/f1c5/3d632a441b49a0730c49cfcd7b108df01b6a.pdf

APPENDIX A: EFFECTIVE THERMAL PROPERTIES OF ASHRAE FUNDAMENTALS WALL ASSEMBLIES

After characterizing every wall assembly in the ASHRAE Handbook of Fundamentals wall database, it was noted that the resulting characterization information can be utilized. Every wall was characterized stochastically via Bayesian inference, which produces a distribution thermal resistances and thermal masses (via Markov chains). This data can potentially serve as a prior distribution database, where the user makes an inference regarding a wall's composition and selects the wall from the database that most closely represents their expectation of the wall's composition. The list of characterized thermal masses and thermal resistances are tabulated below.

Table A.1 A table of stochastic effective thermal properties for all walls in the ASHRAE Fundamentals Wall Database.

Wall ID	Mean Effective Thermal Resistance, m^2-K/W	Standard Deviation of Effective Thermal Resistance, m^2-K/W	Mean Effective Thermal Capacitance, kJ/m^2-K	Standard Deviation of Effective Thermal Capacitance, kJ/m^2-K
Wall #1	2.14	2.42E-02	15.2	0.932
Wall #2	3.82	4.42E-02	16.7	0.189
Wall #3	2.12	4.87E-03	38.5	3.82
Wall #4	3.87	1.27E-02	57.0	2.92
Wall #5	3.74	1.30E-02	2.43	0.491
Wall #6	3.79	1.86E-02	16.8	0.29
Wall #7	2.08	1.23E-02	35.1	1.03
Wall #8	3.94	1.92E-02	53.9	6.37
Wall #9	2.10	1.08E-02	15.7	2.45

Wall ID	Mean Effective Thermal Resistance, m^2-K/W	Standard Deviation of Effective Thermal Resistance, m^2-K/W	Mean Effective Thermal Capacitance, kJ/m^2-K	Standard Deviation of Effective Thermal Capacitance, kJ/m^2-K
Wall #10	3.87	1.94E-02	15.4	0.46
Wall #11	2.19	3.21E-02	19.2	0.684
Wall #12	3.98	1.63E-02	17.4	0.246
Wall #13	2.13	8.54E-03	16.8	2.37
Wall #14	3.94	1.42E-02	16.1	0.244
Wall #15	1.32	1.22E-02	23.7	1.06
Wall #16	2.17	1.54E-02	23.6	0.396
Wall #17	2.95	6.10E-02	21.0	1.31
Wall #18	4.65	2.98E-02	19.6	0.536
Wall #19	1.73	7.33E-03	126	3.81
Wall #20	2.55	5.30E-03	113	0.81
Wall #21	1.56	4.95E-03	46.3	2.89
Wall #22	2.40	9.43E-03	39.7	1.17
Wall #23	2.35	4.20E-03	33.1	0.601
Wall #24	4.13	2.29E-02	26.6	1.65
Wall #25	3.18	1.42E-02	33.8	0.364
Wall #26	5.69	5.11E-02	29.4	1.24
Wall #27	1.53	3.08E-03	126	0.933
Wall #28	2.32	1.15E-02	102	2.13
Wall #29	2.61	7.77E-03	80.8	1.60
Wall #30	4.37	1.65E-02	55.1	1.14
Wall #31	1.40	4.90E-03	215	4.49
Wall #32	2.18	1.01E-02	174	3.40
Wall #33	1.21	3.83E-03	190	3.25
Wall #34	1.98	1.26E-02	146	3.42

Wall ID	Mean Effective Thermal Resistance, m^2-K/W	Standard Deviation of Effective Thermal Resistance, m^2-K/W	Mean Effective Thermal Capacitance, kJ/m^2-K	Standard Deviation of Effective Thermal Capacitance, kJ/m^2-K
Wall #35	1.77	3.86E-03	299	3.93
Wall #36	2.58	1.23E-02	258	5.51
Wall #37	1.51	5.19E-03	647	9.73
Wall #38	2.31	9.58E-03	647	9.73
Wall #39	2.37	9.12E-03	228	3.60
Wall #40	4.23	1.65E-02	141	2.17
Wall #41	2.31	4.49E-03	40.8	0.890
Wall #42	4.20	1.35E-02	32.0	0.428
Wall #43	2.69	2.81E-02	54.2	8.14
Wall #44	4.42	2.46E-02	39.3	2.14
Wall #45	2.12	8.12E-03	46.0	2.00
Wall #46	3.88	6.36E-02	35.0	10.8
Wall #47	0.794	9.61E-04	81.9	0.464
Wall #48	1.05	4.36E-03	92.1	0.600
Wall #49	1.33	5.64E-03	152	5.39
Wall #50	1.30	7.45E-03	43.3	2.49
Wall #51	2.15	2.32E-02	34.5	0.439
Wall #52	2.10	3.30E-03	33.8	0.645
Wall #53	3.98	1.67E-02	26.8	1.41
Wall #54	2.01	1.06E-02	122	2.60
Wall #55	3.43	3.38E-02	92.1	3.56
Wall #56	1.36	2.10E-03	283	3.38
Wall #57	2.15	6.23E-03	235	2.63
Wall #58	2.30	6.15E-03	74.8	1.37
Wall #59	4.03	1.06E-02	47.8	0.722

Wall ID	Mean Effective Thermal Resistance, m^2-K/W	Standard Deviation of Effective Thermal Resistance, m^2-K/W	Mean Effective Thermal Capacitance, kJ/m^2-K	Standard Deviation of Effective Thermal Capacitance, kJ/m^2-K
Wall #60	1.87	6.29E-03	396	4.54
Wall #61	4.62	3.35E-02	992	8.41
Wall #62	2.00	3.26E-03	47.6	0.998
Wall #63	3.78	2.20E-02	36.6	3.21
Wall #64	3.33	1.30E-02	55.8	2.40
Wall #65	6.71	3.65E-02	71.6	2.91
Wall #66	0.159	1.19E-04	622	1.06

APPENDIX B: SUPPLIMENTS TO THE ASHRAE FUNDAMENTALS WALL DATASET

When designing a dataset to classify assemblies from their effective thermal mass and thermal resistance, it was noted that the ASHRAE Fundamentals Chapter 18 wall dataset lacked some wall constructions which are representative of in-service assemblies. These types of assemblies are not present in the ASHRAE Fundamentals database since this list of walls is designed to be representative of new construction applications. To address this issue, 19 additional wall assemblies were generated via the material data already present within ASHRAE Fundamentals. A list of the supplemental assemblies and their effective thermal characterizations are present in Table B.1 and Table B.2.

Table B.1 Material data for supplemental existing building walls.

Wall ID	Layer 1	Layer 2	Layer 3	Layer 4	Layer 5	Layer 6	Layer 7	Layer 8
Wall #67	F01	M03	F02					
Wall #68	F01	M05	F02					
Wall #69	F01	M01	F02					
Wall #70	F01	M01	M01	F02				
Wall #71	F01	M01	M01	M01	F02			
Wall #72	F01	M01	M01	M01	M01	F02		
Wall #73	F01	M01	F04	M01	F02			
Wall #74	F01	M01	G03	F04	G01	F02		
Wall #75	F01	F11	G02	F04	G01	F02		
Wall #76	F01	F08	G03	F04	G01	F02		
Wall #77	F01	F10	G03	F04	G01	F02		

Wall ID	Layer 1	Layer 2	Layer 3	Layer 4	Layer 5	Layer 6	Layer 7	Layer 8
Wall #78	F01	M01	I01	G03	I04	G01	F02	
Wall #79	F01	F11	I01	G02	I04	G01	F02	
Wall #80	F01	F08	I01	G03	I04	G01	F02	
Wall #81	F01	F10	I01	G03	I04	G01	F02	
Wall #82	F01	M01	I01	I01	G03	I04	G01	F02
Wall #83	F01	F11	I01	I01	G02	I04	G01	F02
Wall #84	F01	F08	I01	I01	G03	I04	G01	F02
Wall #85	F01	F10	I01	I01	G03	I04	G01	F02

Table B.2 Thermal characterization data for supplemental existing building walls.

Wall ID	Mean Effective Thermal Resistance, m^2-K/W	Standard Deviation of Effective Thermal Resistance, m^2-K/W	Mean Effective Thermal Capacitance, kJ/m^2-K	Standard Deviation of Effective Thermal Capacitance, kJ/m^2-K
Wall #67	0.412	3.40E-04	77.6	0.220
Wall #68	0.186	1.70E-04	139	0.335
Wall #69	0.116	1.20E-04	135	0.382
Wall #70	0.232	3.99E-04	307	2.71
Wall #71	0.347	2.02E-04	467	0.787
Wall #72	0.462	2.68E-04	621	1.03
Wall #73	0.386	2.39E-04	289	0.320
Wall #74	0.474	2.30E-04	22.3	0.0766
Wall #75	0.532	4.58E-04	26.9	0.142
Wall #76	0.441	5.70E-04	34.9	2.78
Wall #77	0.447	2.88E-04	18.3	0.149
Wall #78	2.96	7.33E-03	22.0	0.176

Wall ID	Mean Effective Thermal Resistance, m^2-K/W	Standard Deviation of Effective Thermal Resistance, m^2-K/W	Mean Effective Thermal Capacitance, kJ/m^2-K	Standard Deviation of Effective Thermal Capacitance, kJ/m^2-K
Wall #79	3.02	1.22E-02	26.4	0.347
Wall #80	2.95	4.98E-03	46.3	1.17
Wall #81	2.93	2.27E-02	21.4	1.87
Wall #82	3.78	2.89E-02	23.8	1.13
Wall #83	3.85	1.41E-02	28.6	0.672
Wall #84	3.86	4.98E-02	66.9	2.10
Wall #85	3.76	6.32E-02	23.0	0.357